UNIVERSITY OF CINCINNATI

Date: 29-Apr-2010

I, Samir B Tambe **,**

hereby submit this original work as part of the requirements for the degree of:

Doctor of Philosophy

in Aerospace Engineering

It is entitled:

Liquid Jets Injected into Non-Uniform Crossflow

Student Signature: Samir B Tambe

This work and its defense approved by:

Committee Chair: San-Mou Jeng, PhD
San-Mou Jeng, PhD

Milind Jog, PhD
Milind Jog, PhD

Shaaban Abdallah, PhD
Shaaban Abdallah, PhD

George Hsiao, PhD
George Hsiao, PhD

Liquid Jets Injected into Non-Uniform Crossflow

A dissertation submitted to the

Graduate School

of the University of Cincinnati

in partial fulfillment of the

requirements of the degree for

Doctor of Philosophy

in the Department of Aerospace Engineering

of the College of Engineering

by

Samir Tambe

M.S. University of Cincinnati

December 2004

Committee Chair: San-Mou Jeng, Ph. D.

Abstract

An experimental study has been conducted with liquid jets injected transversely into a crossflow to study the effect of non-uniformities in the crossflow velocity distribution to the jet behavior. Two different non-uniform crossflows were created during this work, a shear-laden crossflow and a swirling crossflow.

The shear-laden crossflow was generated by merging two independent, co-directional, parallel airstreams creating a shear mixing layer at the interface between them. The crossflow exhibited a quasi-linear velocity gradient across the height of the test chamber. By varying the velocities of the two airstreams, the sense and the slope of the crossflow velocity gradient could be changed. Particle Image Velocimetry (PIV) studies were conducted to characterize the crossflow. The parameter, *UR*, is defined as the ratio of the velocities of the two streams and governs the velocity gradient. A positive velocity gradient was observed for $UR > 1$ and a negative velocity gradient for $UR < 1$. PIV and Phase Doppler Particle Anemometry (PDPA) studies were conducted to study the penetration and atomization of 0.5 mm diameter water jets injected into this crossflow. The crossflow velocity gradient was observed to have a significant effect on jet penetration as well as the post breakup spray. For high UR (> 1), jet penetration increased and the Sauter Mean Diameter (SMD) distribution became more uniform. For low UR (< 1), low penetration, higher droplet velocities and better atomization were observed.

The second crossflow tested was a swirling flow generated using in-house designed axial swirlers. Three swirlers were used, with vane exit angles of 30°, 45° and 60°. Laser Doppler Velocimetry (LDV) was used to study the crossflow velocities. The axial (U_x) and the tangential (U_θ)

components of the crossflow velocity were observed to decrease with increasing radial distance away from the centerbody. The flow angle of the crossflow was smaller than the vane exit angle, with the difference increasing with the vane exit angle. Water jets were injected from a 0.5 mm diameter orifice located on a cylindrical centerbody. Multi-plane PIV measurements were conducted to study the penetration and droplet velocity distribution of the jets. The jets were observed to follow a path close to the helical trajectory of the crossflow with a flow angle slightly less than the crossflow. This deficit in flow angle is attributed to the centrifugal acceleration experienced by the jet. Mie-Scattering images obtained from PIV were used to recreate the jet plume and to obtain the jet trajectory for penetration analysis. In cylindrical coordinate system, the jet penetration can be described in terms of radial and "circumferential" penetration, where circumferential penetration relates to the difference in the circumferential displacement of the jet and the crossflow over the same streamwise displacement. Radial penetration increased with q while circumferential penetration increased with swirl angle. PIV results from cross-sectional and streamwise planes were combined to generate three-dimensional droplet velocity distribution throughout the jet plume. The three-dimensional velocity distribution yielded further insight into the evolution of the jet plume

Acknowledgements

I express my sincere gratitude to my advisor, Dr. San-Mou Jeng, for his continuous guidance and support throughout my studies.

I thank Professors Shaaban Abdallah and Milind Jog and Dr. George Hsiao for being on my advising committee and for their help and support.

I would also like to thank my colleagues at the Combustion Diagnostic Research Laboratory for their help and support. I would like to specially thank Jun Cai and Omar Elshamy. Jun has been my mentor and has been a great help in learning and troubleshooting the diagnostic techniques in the lab. I would like to thank Omar for the hours spent conducting experiments together, and for his valuable insights.

I am grateful to Curtis Fox for his help, support and encouragement, and especially for making the lab a fun place to work in with his entertaining quips and retorts.

My wholehearted gratitude is to my family for their constant love and support. My parents have always been a source of motivation and inspired me to excel. My brothers, Vinit and Rahul, always spurred me to give my best and supported me through the years spent away from them.

I would also like to thank all my friends for their support and care throughout my stay here in Cincinnati.

Table of Contents

List of Figures

List of Tables

List of Symbols

A	cross-sectional area
AR	aspect ratio
C_d	coefficient of discharge
F	force
KE	Kinetic energy
L	reference length
OD	outer diameter
R	radial axis
Re	Reynolds number
U	crossflow (air) velocity
UR	crossflow velocity ratio (shear-laden crossflow)
V	jet velocity, droplet velocity
We	aerodynamic Weber number (crossflow)
X	streamwise axis
Y	vertical axis
Z	lateral axis
$(dU)_y$	slope of velocity gradient (shear-laden crossflow)
R^2	coefficient of determination

a	acceleration
c	vane chord
cb	centerbody
d	jet injection diameter
m	mass
$\dot{m}$	mass flow rate
n	number of vanes
q	momentum flux ratio
r	radius, radial coordinate
t	time
u'	instantaneous velocity
x	streamwise coordinate
y	vertical coordinate
z	lateral coordinate
Θ	circumferential axis
α	vane angle
ϕ	circumferential displacement
λ	grid spacing
μ	dynamic viscosity

θ	circumferential coordinate
ρ	density
σ	surface tension
ψ	flow angle

Subscripts

avg	averaged property
b	lower airstream (shear-laden crossflow)
cf	crossflow
j	jet
r	radial (R) component
turb	turbulent
u	upper airstream (shear-laden crossflow)
x	streamwise (X) component
y	vertical (Y) component
z	lateral (Z) component
θ	circumferential/tangential (Θ) component

Chapter 1 Introduction

1.1 Liquid Jets in Crossflow: Introduction and Motivation

A liquid jet injected transversely into a crossflowing gaseous stream has found applications in aerospace as well as other industrial fields including fuel injection, film cooling [7, 14], and lubrication of the bearing chamber [5]. Application for fuel injection includes fuel injection in the combustion chambers of gas turbines [1, 2, 3, 6], ramjets [16, 17, 25] and scramjets [17] as well as in the afterburner of a gas turbine [25].

1.1.1 Application for Fuel Injection in Gas Turbine Engines

Our application of interest is the fuel injection in the combustion chamber of a gas turbine engine. The major focus for gas turbines over the last decade has been to minimize the production of harmful effluents such as NOx gases, while maintaining thrust output and efficiency. This has led to the emergence and application of low-emission combustion mechanisms such as Lean Premixed Prevaporized (LPP), Lean Direct Injection (LDI) and Rich burn, Quick quench, Lean burn (RQL) [19].

The LPP and LDI concepts seek to limit NOx formation by inhibiting the thermal mechanism of NOx formation. According to Lefebvre [19], the rate of thermal NOx formation increases exponentially with flame temperature. In both the LPP and LDI mechanisms, lean fuel-air mixture is

maintained throughout the primary zone, thus limiting flame temperature, thereby maintaining a suitable low rate of formation of NOx by the thermal mechanism.

Successful application of LPP and LDI necessitates the presence of lean conditions uniformly throughout the primary zone. The presence of even small pockets of near stoichiometric fuel-air mixture could raise the flame temperature locally, thereby accelerating NOx formation. This need to maintain uniform fuel-air mixture imposes several restrictions on the fuel injection mechanism. The fuel atomization has to be good enough to ensure that a homogeneous fuel air mixture exits the nozzle, to preclude the formation of such pockets.

A liquid fuel jet injected transversely into air crossflow is an interesting candidate for the LPP combustion mechanism [1, 2, 3].

1.2 Literature Review: Jets in Crossflow

A jet of fluid injected normal to a crossflowing stream of fluid is one of the basic phenomena in fluid mechanics and has been studied for over half a century [23]. It presents one of the easiest ways of mixing two fluids. Depending upon the nature of the fluids involved, the phenomenon can be classified as single-phase [11, 13], where both fluids are either liquid or gases, or two-phase [1, 6, 7, 28], where one of the fluids is a liquid and the other is a gas. The flowfield is said to be two phase if a liquid jet is injected into a gaseous crossflow or vice versa. There have been similarities as well as differences in the results for single-phase and two-phase jets in crossflow. Here we attempt to outline some of the significant observations for both. We are mainly interested in liquid jets in a gaseous (air) crossflow, which will be referred to simply as Liquid Jets in Crossflow from here on.

1.2.1 Single-Phase Jets in Crossflow

Single phase jet in crossflow occurs when a gaseous jet is injected into a gaseous stream or a liquid jet is injected into a liquid stream. It is common practice to use the same fluid for both jet and crossflow [11, 13], so that the physical properties are matched, making studies easier. The important parameters for the study of the single-phase jet in crossflow are the Reynolds number of the crossflow [11] and the ratio of the velocity of the jet to that of the crossflow [11, 13].

As soon as the jet enters the crossflow, the jet entrains momentum as well as mass from the crossflow [13, 30]. As a result, the jet acquires momentum in the direction of the crossflow, causing the jet to tilt towards the direction of the flow of the crossflow.

The location of the jet and the rate of mixing with the crossflow can be measured using a parameter called the mixture fraction [22], which measures the ratio of the volume of crossflow fluid present per unit volume of total fluid passing any location in the flow field. Thus the mixture fraction has a value of 1 at a location containing only jet fluid, and 0 at a location containing only crossflow fluid. The mixture fraction thus enables studying the spread of the jet fluid within the flow field.

The location and spread of the jet fluid can be quantified in terms of the jet penetration [13, 26, 30]. The jet penetration represents the transverse height achieved by the jet at any streamwise location, and is usually specified in terms of a correlation. However, there exist some discrepancies in the definition of penetration itself. It is common practice to define the jet penetration as the location of the highest location in the jet centerplane where jet fluid is present [13, 26, 30]. Typically a cutoff mixture fraction is defined, and the location where this is achieved is denoted as the location of jet penetration. Other researchers have used the location of maximum mixture

fraction to describe the jet penetration. In all cases, the jet penetration has been shown to be a function of the velocity ratio [13].

The jet flow field has been observed to be highly turbulent, with the presence of several vortex structures [11, 14, 18, 26]. Near injection, the jet is seen to consist of ring vortices which are periodically shed from the nozzle. Further downstream, the jet is mainly composed of a counter-rotating vortex pair which gives the jet its well-known kidney shape. Additionally, a horse-shoe vortex is observed to wrap around the base of the jet. A wake region forms behind the jet and is observed to be composed of a series of wake vortices.

1.2.2 Liquid Jets in Crossflow

Liquid Jets in Crossflow is also a well researched area. Quite a few reviews exist [9, 23, 27], discussing the various features, so we will only look at a few key results here.

The liquid jets bends soon after injection, due to the dynamic pressure of the crossflow, which can also be seen as a drag force exerted by the crossflow on the jet [15, 30]. In addition to imparting momentum to the jet stream, the drag force also causes a shear action on the liquid surface causing the surface to break up into small droplets [6, 28].

The jet eventually breaks up into ligaments which further break up to form droplets [28]. Different breakup modes have been observed, including the column breakup and shear breakup [1, 28]. The significant parameters of the jet with regards to breakup are the aerodynamic Weber number, We, and the momentum flux ratio, q [1, 9, 27, 28]. We is defined as a ratio of the dynamic pressure of the crossflow to the surface tension forces of the jet. The dynamic pressure reflects the aerodynamic force exerted by the crossflow on the jet, inducing the jet to break up. On the

other hand, the surface tension forces seek to maintain the jet surface, and thus oppose breakup. Thus, *We* is a measure of the capacity of the crossflow to induce breakup. The momentum flux ratio, *q*, is a ratio of the dynamic pressure of the jet to that of the crossflow, and represents the ability of the jet to withstand the crossflow. This is mostly affects of the penetration of the crossflow, with jets of higher *q* penetrating further into the crossflow. Another parameter of interest is the Ohnesorge number, *Oh*, which relates the viscous forces to the inertial and surface tension forces. Birouk et al [5] observed that jet penetration was affected by viscosity for jet fluids with high *Oh* (high viscosity).

Many studies have focused on the jet trajectory and penetration, similar to single phase jets in crossflow. For liquid jets in crossflow, penetration is usually defined as the maximum transverse location of the liquid jet. Wu et al [28] modeled the jet trajectory by balancing liquid acceleration with aerodynamic drag forces in the streamwise direction. Studies focused on penetration include experimental as well as computational studies. Lin et al [21] conducted a review of the penetration of liquid jets in crossflow. In most of the studies, the penetration height at any streamwise location has been related to the momentum flux ratio, *q*, the nozzle diameter, *d* and the streamwise coordinate.

The extent of atomization and mixing of the jet can be characterized by droplet sizes, which represent the extent of atomization, and the volume flux, which represents the spatial progress of the jet, and is indicative of mixing with the crossflow.

Since atomization is one of the chief concerns for liquid jet in crossflow, several studies have focused on the droplet characteristics of the post breakup jet spray [16, 27, 29]. Studies have characterized the droplet sizes both in the far field [16] and more recently in the near field region

[29] of the jet. The droplet size distribution within the spray plume has been studied and has been observed to depend on q and the streamwise distance from the location of injection [16, 27, 29].

The volume flux distribution typically exhibits a small region of high flux, called the jet core. The core typically consists of larger droplets [27, 29].

Another parameter of interest in studying jet atomization is droplet velocities as it indicates the tendency of the droplets to spread [9, 16, 27, 29]. Low streamwise velocities are observed in the spray core, probably due to the presence of larger droplets. The droplet velocities are observed to peak near the top of the spray plume.

1.3 Jets in Non-Uniform Crossflow

The research presented in sections 1.1 – 1.2 assumes the crossflow to be uniform, i.e. they assume a uniform streamwise velocity profile in the transverse direction. Some studies do account for the presence of boundary layer near the wall, but it is mostly neglected. The advantage of using such a crossflow is that it simplifies the flow field, allowing the researcher to focus on the interaction and behavior of the jet itself.

However, there exist quite a few applications where the crossflow experienced by a jet is not uniform, and may contain severe velocity gradients. Examples are spinning jets and secondary fuel injection in gas turbine combustors.

Spinning jets can be observed in garden sprinklers and in prilling [8]. The nozzle itself rotates about an axis, so that even if the surrounding flow is stationary, it appears to be moving with respect to the jet nozzle, with the velocity decreasing inversely with respect to (radial) distance from the nozzle.

Another relevant example is the secondary fuel injection in a gas turbine combustor. Several gas turbines still use simplex type nozzles for fuel injection. However simplex nozzles prove to be inefficient to provide suitable atomization for the very high dynamic range of flow rates needed over the course of a flight cycle. This is usually avoided by providing two separate fuel nozzles, with the primary nozzle, usually of simplex type, used for low fuel flow requirements. For higher fuel flow requirements, the secondary nozzle is also turned on.

A viable option is to use jet injectors to inject secondary fuel, with injection occurring slightly offset to the primary fuel injection. In this way, the primary zone can still be operated at fuel lean conditions, and the combustion could be spread over a larger area. The air flow experienced by the secondary jets is the air downstream of the air swirler, and thus is highly non-uniform.

In a non-uniform crossflow, especially in a swirling crossflow, the three-dimensional nature of the crossflow can have significant effect on the jet behavior which cannot be predicted by studying jets in uniform crossflows, and hence needs to be investigated.

1.4 Literature Review: Jets in Non-Uniform Crossflow

1.4.1 Single-Phase Jets in Non-Uniform Crossflow

Lilley [20] investigated the injection of dilution air jets into a swirling combustor flow field. The swirling flow was created by a variable-angle vane axial swirler into a cylindrical test chamber. Two jet orifices, located diametrically opposite from each other on the wall of the chamber were used for jet injection. Jets were injected radially inwards into the flow. Jet penetration studies were conducted at different velocity ratios and swirl vane angles, both for single and two jets. They observed that jet penetration reduced as swirl vane angle increased.

1.4.2 Liquid Jets in Non-Uniform Crossflow

Becker and Hassa [2] studied liquid fuel injection into a prototype LPP injection module, featuring a double-annular, counter-swirling crossflow. Fuel jets were injected radially outward from a cylindrical centerbody. Experiments were conducted at elevated temperature and pressure to simulate gas turbine operating conditions. Measurements were conducted 1 mm downstream of the outlet of the premix module. The distance of the swirler and nozzle from the outlet could be varied to simulate measurement at various distances downstream of injection. They studied the effect of density and fuel flow rate on jet behavior. As pressure increases, the swirl Stokes number increases, so that the droplets are more likely to follow the swirling path of the crossflow. Using superposition to extrapolate the fuel flux data for a single jet, they observed that the fuel flux reached asymptotic circumferential homogeneity for 8 nozzles, for their particular setup.

In a follow-up study, Becker Heitz and Hassa [3] studied the effect of a filmer ring on the jet behavior. The filmer ring was introduced between the two annular swirling flows, and thus served to eliminate radial movement of the droplets in the shear layer between the two swirling flows. They observed that at high pressure, the fuel droplets remained trapped in the inner annulus due to the local dominance of drag forces. On the other hand, turbulent mixing was enhanced, resulting in a uniform droplet size distribution, while the volume flux remained non-uniform.

Gong et al [12] conducted a preliminary study on water jets injected radially inwards into a cylindrical chamber with a swirling crossflow, with a configuration similar to that used by Lilley. They varied the crossflow swirl number and the jet diameter, the injection angle of the jet and the injection velocity.

1.5 Motivation and Objectives of Current Study

From section 1.4, it can be seen that very few researchers have tackled the issue of the effect of non-uniform crossflows on transversely injected liquid jets. Hence there is a need to conduct such a study to understand the differences in the flow field and to quantify their effect on jet behavior. The current work proposes to conduct such a study. Our aim is to create specific crossflow with typical non-uniform velocity profiles. The crossflow will be characterized, and this information will be used to study the effect of the crossflow on the behavior of transversely injected liquid jets.

Two such non-uniform crossflows have been studied. The first crossflow creates a shear layer along the interface of two rectangular airstreams of different velocities. Liquid jets will be injected in a manner normal to the resultant shear layer. The crossflow has been termed as a shear-laden crossflow on account of the shear mixing layer between the two airstreams. By varying the velocities of the two streams, it is possible to generate crossflows with positive or negative velocity gradients, i.e. where the crossflow velocity increases (positive gradient) or decreases (negative gradient) with increasing distance from the jet injection surface. The purpose of generating such a crossflow is to serve as a 2-D equivalent of a swirling flow, with the velocity gradient representing the variation of tangential velocity in a simplified swirling flow (solid body rotation). The effect of the velocity gradient, in addition to relevant jet parameters, on the penetration and atomization of the liquid jets will be studied.

The second crossflow implemented is a swirling crossflow. Axial swirlers with different vane exit angles were used to generate swirling flows of differing swirl strengths. A liquid jet was injected radially outwards from an orifice on a cylindrical centerbody. The effect of the swirl flow on the penetration and the droplet velocity distribution of the droplets in the jet will be studied.

The highly three-dimensional nature of the flow imposes several restrictions on such measurements, and the attempts made to overcome these restrictions will also be described in detail.

Chapter 2 Experimental Setup and Measurement Techniques

In this chapter, the experimental setup, and the measurement techniques used for the two crossflows studied will be discussed. Due to the nature of the flows, separate experimental fixtures were required for both.

2.1 Experimental Setup for Shear-Laden Crossflow

2.1.1 Concept of the Setup

The concept of the Shear-Laden crossflow originated as a 2-D representation of a simplified swirl flow. The simplified swirl flow is likened to a solid body rotation with constant axial velocity, zero radial velocity and tangential velocity proportional to the radius. Then the tangential velocity varies linearly with radial distance, or height. Our aim was to create a situation that would result in a quasi-linear velocity gradient across the height of the test chamber.

Such a velocity gradient was created by creating a horizontal partition in the center of the test chamber inlet. Two independent airstreams were introduced into the chamber from above and below the partition, such that they were parallel to each other, but with different velocities. As the two streams merge, a shear layer is created at the interface due to the difference in velocities, leading to momentum exchange between the two streams. As the flow moves downstream, the thickness of the shear layer increases, creating a quasi-linear velocity gradient across the height of the test chamber. Additionally, since the velocities of the individual airstreams can be con-

trolled independently, it is possible to have a case where the crossflow velocity increases with height (positive gradient) or vice versa (negative gradient).

In order to develop the necessary crossflow profile, it is necessary to introduce two separate airstreams, parallel to each other, into the test chamber. Thus there is a need to create a setup that will keep the two streams separated up to introduction into the test chamber. The following sections describe the test setup created to satisfy these requirements.

2.1.2 Test Rig

A new rig was created to satisfy the requirement of merging two separate airstreams at the inlet of the chamber. The rig is mounted on a frame consisting of Bosch Aluminum Structural Members. A common air supply is split up into two flow paths via pipes, each equipped with an orifice flow meter to measure flow rates and a valve downstream of the orifice plate to control the flow rate. Flexible hoses connect the two flow paths to the two air inlets on the test rig.

A schematic of the test rig has been shown in Figure 2.1. On each flow path, the air inlet leads into a settling chamber where it undergoes a 90° turn. The settling chambers are rectangular, with inner dimensions of 3.81 cm × 8.89 cm × 30.48 cm (1.5 inch × 3.5 inch × 12 inch), with a wall thickness of 6.35 mm (1/4 inch). The air inlet is located 5.08 cm (2 inch) from the upstream end of the settling chamber.

As shown in Figure 2.1, the two settling chambers are welded together along the side opposite to the air inlet. As a result, the combined outflow has a total cross sectional area of 8.89 cm × 8.89 cm (3.5 × 3.5 inch) including a 1.27 cm (1/2 inch) vertical separation between the two airstreams.

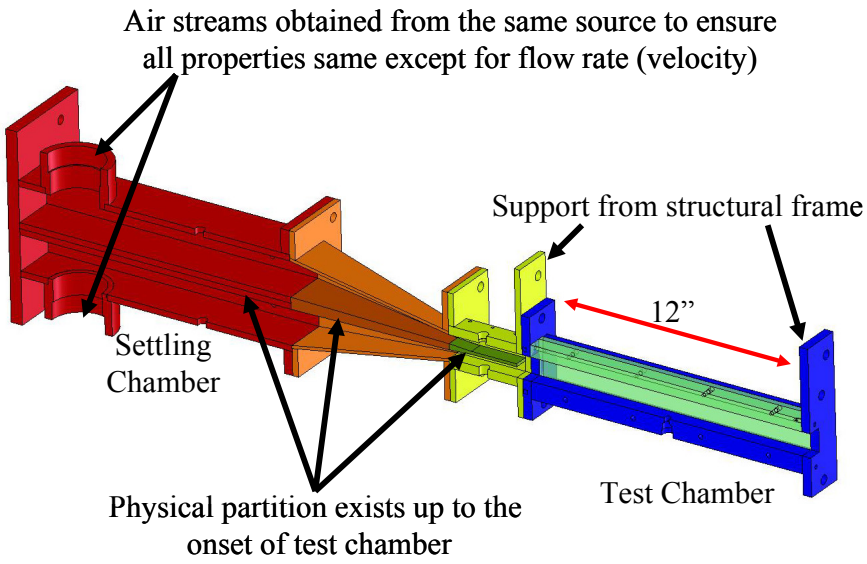

Figure 2.1 Schematic of the Test Rig for Shear Laden Crossflow

A square reducer brings down the total inner cross sectional area to 2.54 cm × 2.54 cm (1 × 1 inch). The reducer is fitted with a center plate that keeps the two airstreams separated. The thickness of the center plate tapers uniformly from 12.7 mm (1/2 inch) at the inlet to 6.35 mm (1/4 inch) at the exit.

A 7.62 cm (3 inch) long straightener section follows the reducer. The straightener section has a square cross section with and inner dimension of 2.54 cm (1 inch). A partition plate is built into the straightener to continue separating the airstreams. The thickness of the partition plate tapers uniformly from 6.35 mm (1/4 inch) at the inlet to 3.17 mm (1/8 inch) at a location 2.54 cm (1 inch) from the inlet, and then remains constant up to the exit. The straightener leads into the test chamber. The two airstreams, which have been physically separated, are merged at the outlet of the straightener section, leading into the test chamber.

Honeycomb strips were installed in the settling chambers and in both passages of the straightener section to smooth out the airflow.

2.1.3 Test Chamber

The test chamber, shown in Figure 2.2, has a square cross section of internal dimension 2.54 cm (1 inch) and is 30.48 cm (12 inch) long. The side and top walls of the test chamber are constructed of Lexan material for clear optical access, while the bottom wall is aluminum. Locations for installing the jet nozzle are provided 6.35 cm (2.5 inch) and 15.24 cm (6 inch) from the inlet, centered in the lateral direction. The 6.35 cm location was used for all tests. The nozzle is a 6.35 mm (1/4 inch) OD stainless steel tube with a flat endwall. A 0.5 mm diameter orifice is bored into the center of the endwall. Figure 2.3 shows a cross sectional view of the nozzle. The nozzle was installed so that the endwall surface is flush with the upper surface lf the bottom wall of the test chamber. The C_d of the nozzle was assumed to be 1.

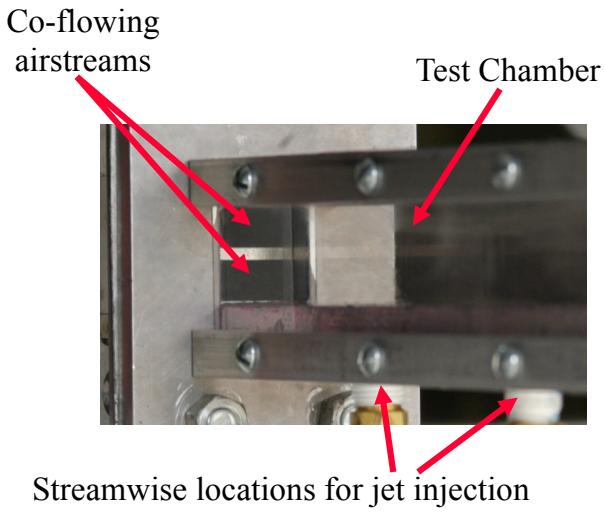

Figure 2.2 Test Chamber used for Shear Laden Crossflow

2.1.4 Air Delivery System

The air delivery subsystem that provides compressed air to the test consists of a compressor, air dryer, pressurized collection tanks and pressure regulator. The compressor used is a Kaeser Vari

able Speed, 335 HP, rotary screw compressor, rated at 1483 SCFM at 100 psig, and is capable of air flow rates of up to 0.907 kg/s (2 lb/s) at pressures of up to 13 bars (175 psig). A Domnick-Hunter Series DBP 1680, 200 psi heat reactivated blower purge desiccant air dryer removes moisture from the compressed air. The compressed air is stored in two 620 gallon vertical receiver tanks, and the flow is regulated by means of a pressure regulator located downstream of the tanks. A series of 10.16 cm (4 inch) and 5.08 cm (2 inch) diameter pipes connect the air delivery subsystem to the experiment. Figure 2.4 shows a schematic of the air delivery subsystem.

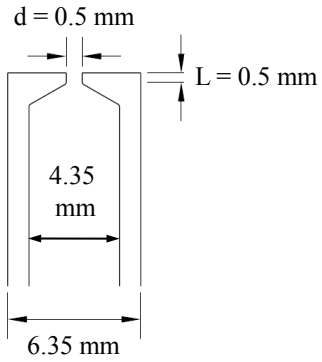

Figure 2.3 Section View of the Jet Nozzle

2.1.5 Water Delivery System

The liquid used for jet injection was water. Water is contained in a tank, which is pressurized using by a compressed nitrogen cylinder. The nitrogen pressure in the tank is regulated to ensure constant flow rate. Water issuing out of the tank passes through a filter and a coriolis flowmeter (Micro Motion CMF010) which monitors the fuel flow rate. A high precision Parker metering valve is used to control the water flow rate. Flexible 6.35 mm (1/4 inch) OD tubes are used to connect the tank to the nozzle via the flow control and metering assembly.

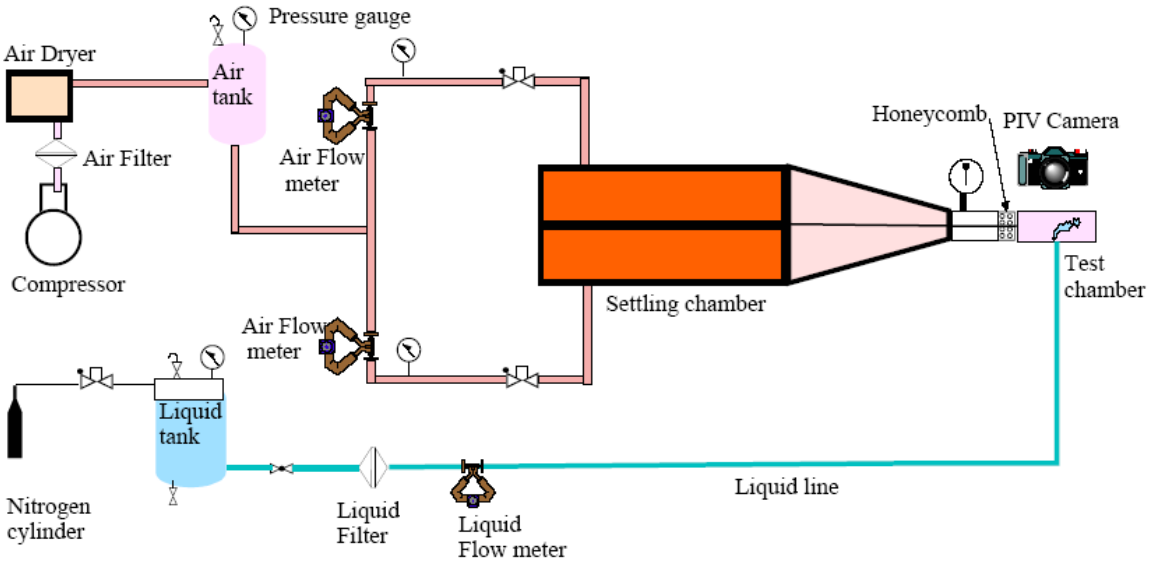

Figure 2.4 Schematic of the Air Delivery System

2.1.6 Particle Seeder

In-house designed olive oil seeders are used to seed the crossflow for the tests designed to investigate the characteristics of the crossflow.

2.2 Experimental Setup for Swirling Crossflow

2.2.1 Concept of the Setup

The main objective of this portion of the study is to determine the effect of the swirling crossflow on the water jets. To minimize complexity, a pre-vortex breakdown helical flow is desired. In order to preserve the nature of such a flow, which is axisymmetric, it is necessary to create a cylindrical enclosure. However it is extremely difficult to conduct measurements like PIV or PDPA inside a cylindrical chamber due to refraction at the chamber walls. Becker and

Hassa [2] overcame this issue by conducting measurements downstream of the exit of the enclosure. However, since one of our aims is to study the progress of the set, it becomes necessary for us to conduct measurements within the test chamber. Due to this, a test chamber with a square cross-section was used. Though this is expected to create unwanted disturbances in the crossflow, the process of taking measurements becomes a lot easier. The disturbances in the crossflow are expected to be in the form of recirculation zones due to the sharp corners. The corners of the test chamber were chamfered to dampen the corner recirculation zones. Additionally, the test chamber was made to be large enough so that the area of interest lies within the inner region of the crossflow, thereby remaining relatively unaffected by the recirculation zones.

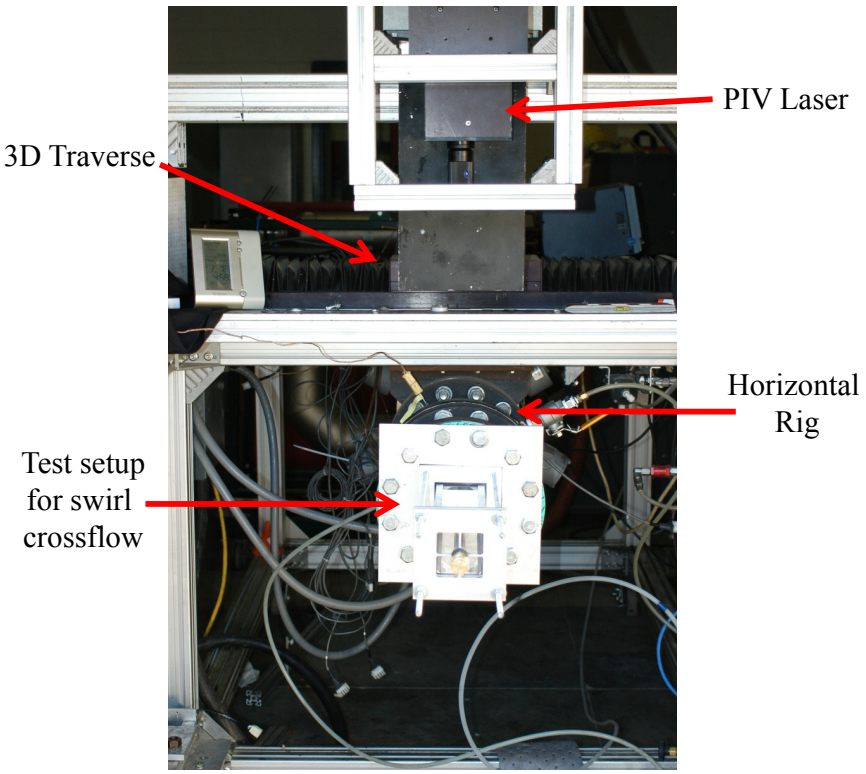

Figure 2.5 Horizontal Rig with Test Chamber for swirling crossflow and PIV installed

2.2.2 Horizontal Rig

The swirl crossflow experiments were set up on the Horizontal Rig (Figure 2.5), which is one of the experimental rigs available in the Combustion Diagnostics Research Laboratory in University of Cincinnati's Center Hill Facility. The Horizontal Rig is essentially a long 15.24 cm (6 inch) diameter pipe, mounted on a frame of Bosch Rail structural members. The frame is mounted on casters so as to allow movement of the rig. The Rig is equipped with a 72 kW inline air heater for preheating the air. The inlet of the rig is connected to the air delivery system by means of a 5.08 cm (2 inch) diameter flexible hose. Test hardware is mounted onto a standard 6 inch 300 lb flange at the outlet of the rig. A Lintek three-axis traverse is mounted on the Bosch Rail frame. It is controlled by a Velmex VP9000 controller, which can be operated by a computer via an RS-232 interface.

2.2.3 Mechanism for Swirl Generation

The test setup consists of the swirler assembly and the test chamber. The swirler assembly consists of the swirler, and the mounting plate for the swirler. The base plate mounts onto the horizontal test rig. The swirler is held in place by the swirler holder, which bolts on to the base plate (Figure 2.8).

The swirlers were designed in-house to be used for this experiment. The swirlers have an axial width of 2.54 cm (1 inch). The flow annulus has an outer diameter of 7.62 cm (3 inch) and an inner diameter of 2.22 cm (0.875 inch). A 1.91 cm (3/4 inch) diameter hole is provided at the center for installing a cylindrical center body, which also serves as the jet nozzle.

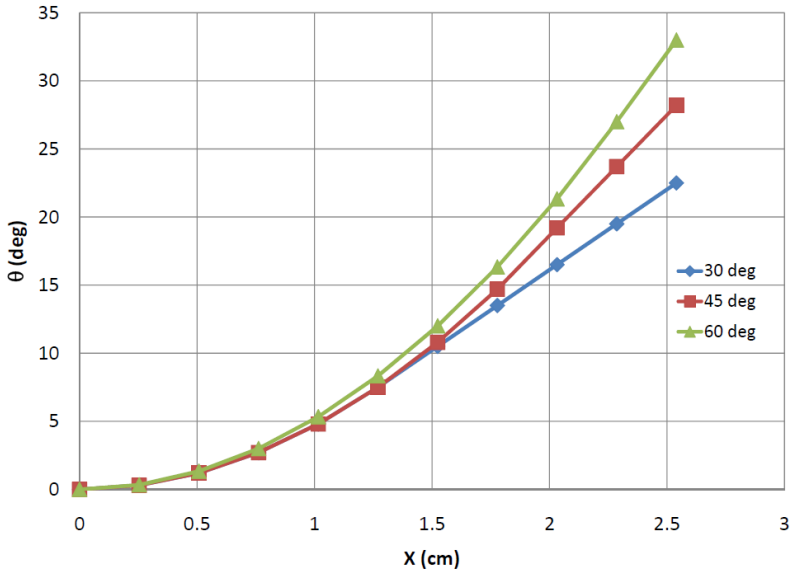

Figure 2.6 Vane Design

Three swirlers were designed, with vane exit angles of 30°, 45° and 60°. The vanes are radial, and were designed so as to create a smooth transition from 0° (axial direction) to the vane exit angle. Figure 2.6 shows the change in orientation of the vanes for the three swirlers over the length of the swirler (1 inch). Figure 2.7 shows the design concept as well as the finished 45° swirler. Table 2.1 lists the specifications for the three swirlers. Swirl numbers [4] were calculated from equation 2.1, where vane angle (α) is assumed to be constant. Aspect ratio is defined as the ratio of the vane height to the vane chord (c) where chord is the streamwise dimension of the vane. The Aspect Ratio (AR) can be calculated from equation 2.2. Vane solidity is defined as the radio of the vane chord to the circumferential spacing of the blades for a given diameter and is given by equation 2.3, where n refers to the number of vanes. Mean AR and *solidity* were calculated using vane properties at the mean radius ($0.5(r_{hub} + r_{tip})$).

$$S = \frac{2}{3}\left[\frac{1-\left(r_{hub}/r_{tip}\right)^3}{1-\left(r_{hub}/r_{tip}\right)^2}\right]\tan\alpha \qquad (2.1)$$

$$AR = \frac{r_{tip} - r_{hub}}{c} \tag{2.2}$$

$$Solidity = \frac{n \cdot c}{\pi\left(r_{tip} + r_{hub}\right)} \tag{2.3}$$

Both the 45° and 60° swirlers have 12 vanes. Since the 30° swirler had the smallest vane curvature, the number of vanes was increased to 16 to maintain reasonable solidity.

a) 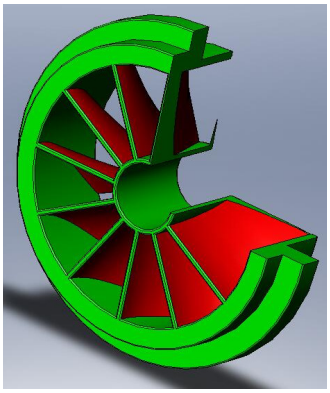 b) 

Figure 2.7 45° Swirler a) Design Concept, b) Swirler

a) 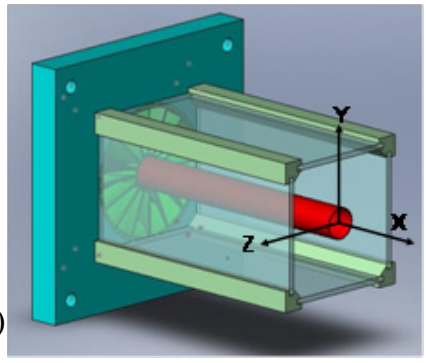

b) 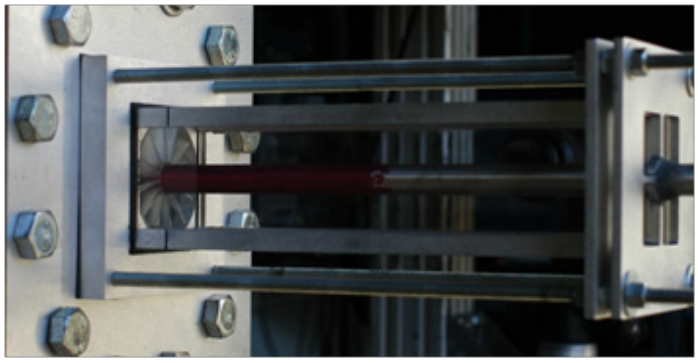

Figure 2.8 Test Chamber. a) Solidworks Model, b) Test Chamber

Table 2.1 Swirler Specifications

Vane Exit Angle	No. of Vanes	Mean Solidity	Mean Aspect Ratio	Swirl Number
30	16	3.53	0.95	0.41
45	12	2.83	0.85	0.71
60	12	3.2	0.75	1.23

2.2.4 Test Chamber

The test chamber has a square cross-section with an internal dimension of 7.62 cm (3 inch) and is 30.48 cm (12 inch) long. It is constructed out of 4 struts which support the walls made of 3.18 mm (1/8 inch) thick acrylic material for optical access. The corner of the strut that is interior to the test chamber is chamfered to suppress corner recirculation. The struts are connected to the swirler mounting plate. A downstream flange, supported by threaded rods from the swirler plate, is connected to the downstream ends of the struts and supports the walls of the test chamber. Figure 2.8 shows a model as well as a picture of the test chamber, along with the swirler assembly and the centerbody. Figure 2.8 also shows the coordinate system used.

2.2.5 Centerbody

A 38.1 cm (15 inch) long, 1.92 cm (3/4 inch) outer diameter, stainless steel tube, with 1.65 mm (0.065 inch) thick walls is used as a centerbody. The centerbody is inserted through the hub of the swirler and extends through the length of the test chamber. A second flange, connected to the downstream flange of the test chamber is used to support the downstream end of the centerbody.

The centerbody provides the jet injection nozzle in the form of a circular orifice of diameter 0.5 mm located 2.54 cm (1 inch) downstream of the swirler exit. The jet orifice was machined in the

tube wall by Electro-Discharge Machining (EDM) process. The downstream end of the centerbody tube is sealed. The water supply system is connected to the upstream end of the centerbody through a 6.35 mm (1/4 inch) flexible tube that is inserted into the horizontal rig by means of a feed-through fitting. The centerbody is oriented so that the jet will issue vertically upwards from the nozzle.

2.3 Measurement Techniques

This section describes the diagnostic equipment used in the measurement of the crossflow and jet properties.

2.3.1 Particle Image Velocimetry (PIV)

Particle Image Velocimetry is a measurement technique used to obtain velocity distribution in an area of interest in the measurement plane. Two images are captured in quick succession at a known time interval and cross-correlation is applied between the two images to map out the displacement of all particles within the area of interest. This is used to calculate the velocity vectors throughout the area of interest.

The PIV system used is a commercial LaVision PIV system. The system consists of a double-pulsed Nd:YAG laser and a double frame - double exposure CCD Camera. The laser is a New-Wave, SOLO PIV, Nd:YAG laser with a pulse energy of up to 120 mJ per pulse at 15 Hz. The Laser light has a wavelength of 532 nm. The CCD camera is a LaVision Imager Intense, and is capable of taking either two buffers or two frames in rapid succession. It records 12 bit digital images with a resolution of 1376 × 1040 pixels per frame. It features a built-in electronic shutter

with exposure times as short as 500 ns and can record double frames at the rate of 5 Hz. The camera is equipped with a 105 mm focal length Nikon Lens with a maximum aperture of f/2.4. A 532 ± 3 nm bandpass filter is used to prevent exposure to light sources other than the laser. Additional details of the PIV system can be found in Elshamy [9].

For the shear-laden crossflow, measurements were conducted in the vertical centerplane of the test chamber, which is also the centerplane of the jets. For the swirling crossflow, PIV measurements were carried out in multiple, equidistant, cross-sectional and streamwise planes.

2.3.2 Phase Doppler Particle Anemometry (PDPA)

Phase Doppler Particle Anemometry (PDPA) and Laser Doppler Velocimetry (LDV) are pointwise, laser-based measurement techniques to measure the droplet size and velocity, respectively of all particles crossing the measurement volume. In both techniques, two laser beams are made to intersect at a known angle, resulting in a fringe pattern at the location where the beams meet. This location is referred to as the measurement volume. Then any particle crossing the measurement volume will produce a frequency shift proportional to its velocity. Additionally, refraction of the laser light due to the surface curvature of the particle would produce a phase shift in the laser beam which can be used to calculate the particle size. Thus LDV and PDPA provide accurate means of measuring the velocity and size of all particles at a particular location in the flow field. PDPA systems can typically be operated in either in the LDV mode, where only velocities are measured, or in the PDPA mode, where particle sizes are also measured.

A Coherent Innova 90 Argon Ion Laser forms the core of the PDPA system. It produces a light beam within the green-blue-violet energy spectrum at a maximum power of 5 Watts. An Aero-

metrics FBD 240-R FiberDrive beam separator separates the beam into its constituent green (514.5 nm), blue (488.0 nm) and violet (476.5 nm) components. Only the green and the blue beams were used. The FiberDrive further splits each of these components into two and shifts the frequency of one component of each wavelength by 40 MHz using a Bragg Cell. All beams, shifted and unshifted, are focused onto fiber-optic cables connected to an Aerometrics XRV204-4.2 two-component transmitter outfitted with a 500 mm focal length lens. An Aerometrics RCV208 receiver is mounted on the other side of the measurement region at a 30° azimuthal angle with respect to the transmitter. The receiver sends signals to an Aerometrics RCM200LP6 Photodetector, which directs the blue and green signals to different Real Time Signal Analyzers (RSA 2000-P2 for green and RSA 2000-L for blue). The Analyzers send the processed data to a DOS-based computer with the DataView software, which records and processes the data. Additional details on the PDPA system can be found in Flohre [10].

In order to map out the desired measurement volume, both the transmitter and the receiver were mounted on a three-axis, Lintek traverse which is controlled by a Velmex VP9000 controller. The DataView software interfaces with the Velmex controller via a RS-232 connection, and is used to operate the traverse. Thus the information of the measurement location is also collected along with the PDPA data.

The Aerometrics PDPA system was used to study the behavior of the jets injected into the shear-laden crossflow. Measurements were conducted in the jet centerplane and 2 cross-sectional planes for a limited number of test conditions.

2.3.3 Phase Doppler Interferometry (PDI)

Phase Doppler Interferometry (PDI) is equivalent to the PDPA/LDV measurement technique. The PDI-200 system, developed by Artium Inc., is essentially a compact PDPA system. The PDI-200 system consists of a transmitter, a receiver, power supply for the transmitter and two signal processors for the two laser channels. The lasers used in the PDI-200 system are Diode Pumped Solid State (DPSS) lasers, which are very compact, and need no active cooling. This enables the lasers to be installed directly into the transmitter, thereby avoiding the need for fiber optic systems, and the accompanying alignment issues. Data is processed through the AIMS software which can also control the traverse to enable measurement over an area of interest.

The PDI-200 system was used in the LDV mode to characterize the swirling crossflow. Measurements were conducted in a cross-sectional plane located 2.54 cm (1 inch) downstream of the location of jet injection.

2.4 Relevant Parameters and Properties

2.4.1 Jet Properties

The liquid used for jet injection was water at room temperature. The density of water, ρ_j, was 996 kg/m^3 and the surface tension, σ, was taken as 0.072 N/m. Water flow rate was measured by a coriolis flow meter, MicroMotion CMF010. The jet injection velocity was calculated from the measured flow rate and the known nozzle area with C_d assumed to be 1.

2.4.2 Important Parameters for Liquid Jets in Crossflow

The chief parameters for liquid jet in crossflow are the Reynolds number, *Re*, of the crossflow, the aerodynamic weber number, *We*, of the crossflow corresponding to the jet and the momentum flux ratio, *q*, of the jet. The Reynolds number of the crossflow is defined with respect to the cross-sectional dimension of the test chamber and is given by

$$\mathrm{Re} = \frac{\rho_{cf} U L}{\mu} \tag{2.4}$$

where ρ_{cf} is the density of the crossflow fluid (air), U is the crossflow velocity, L is the reference length, and μ is the dynamic viscosity of the crossflow fluid (air).

The Weber number, *We*, is a ratio of the aerodynamic force exerted by the crossflow on the liquid jet to the surface tension forces exerted by the surface of the jet, and is given by,

$$We = \frac{\rho_{cf} U^2 d}{\sigma} \tag{2.5}$$

where d is the jet injection diameter and σ is the surface tension of the jet fluid.

The momentum flux ratio, *q*, is defined as the ratio of the momentum of the jet to that of the crossflow and is given by,

$$q = \frac{\rho_j V^2}{\rho_{cf} U^2} \tag{2.6}$$

where V is the jet velocity.

Chapter 3 Liquid Jets Injected into Shear-Laden Crossflow

3.1 Approach to Measurements and Test Conditions

In an attempt to create a 2-D analogy to a swirling flow, a flow with unknown characteristics was created. Hence it is essential to develop a complete understanding of the crossflow in order to analyze its effect on liquid jets.

From the description of the test setup for the shear-laden crossflow, it can be seen that there are two components that make up the crossflow, the two independent streams that are introduced into the test chamber. Based on physical position, they will be referred to as the upper and the lower airstreams, and will be represented by the subscripts *u* and *b* respectively.

Since there are two components to the crossflow, two independent quantities can be defined to quantify the flow. The first quantity is chosen to reflect the total amount of airflow passing through the test chamber, and the second quantity is chosen to represent the proportion in which the flow is divided among the two streams.

The first quantity is the total mass flow rate, which is proportional to the average velocity in the test chamber. Now if the air temperature does not change significantly, then from equation 2.4 it is known that crossflow velocity is proportional to the Reynolds number, *Re*. Then *Re*, defined based on the average crossflow velocity, represents the total mass flow rate of the crossflow. *Re* is defined as:

$$\mathrm{Re} = \frac{\rho_{cf} U_{avg} L}{\mu} \tag{3.1}$$

where L represents the dimension of the test chamber (= 2.54 cm), and U_{avg} represents the average velocity of the crossflow, given by,

$$U_{avg} = \frac{U_u + U_b}{2} \tag{3.2}$$

It is to be noted here that the velocities of the two component airstreams, U_u and U_b were calculated from the mass flow rates measured for the two air channels.

The second quantity denotes the division of the total flow rate among the two streams. A simple way to represent it is the ratio of the mass flow rates of the two streams. Now, velocity is related to mass flow by the relation $\dot{m} = \rho_{cf} A U$. Then since the flow area at the inlet of the test chamber for each stream is the same, it follows that the ratio of the velocities of the two streams is equal to the ratio of the flow rates of the two streams. Then the second quantity can be represented by the velocity ratio, *UR*, defined as,

$$UR = \frac{U_u}{U_b} = \frac{\dot{m}_u}{\dot{m}_b} \tag{3.3}$$

The crossflow can then be completely described by *Re* and *UR*.

Equation 2.4, shows that the aerodynamic weber number, *We*, depends upon the crossflow velocity, and the jet properties. Now since jets used had a constant diameter, and the same fluid was used, it is possible to calculate the expected *We* for jet injection, even though no jets were actually injected for the crossflow studies. *We* is defined using the average crossflow velocity, U_{avg}, as shown in equation 3.4. Now, since *We* is uniquely related to U_{avg}, it is possible to use *We* to de-

fine the crossflow instead of *Re*. *We* and *q* are the two most significant parameters for liquid jets in crossflow, so it follows that *We* is a more suitable choice of parameter to describe the crossflow as compared to *Re*. Hence the pair (*We*, *UR*) will be used to identify the crossflow. Now, for the shear-laden crossflow, the definition of *We* is based on the average crossflow velocity, as shown in equation 3.4.

$$We = \frac{\rho_{cf}\left(U_{avg}\right)^2 d}{\sigma} \tag{3.4}$$

3.1.1 Test Conditions

PIV studies were used to characterize the crossflow. The PIV studies were conducted in a streamwise vertical plane passing through the center of the test chamber. Thus the measurement plane was the centerplane of the test chamber. Then, since the jet nozzle is located at the center of the test chamber, the PIV measurement plane also aligns with the centerplane of the jet. The coordinate frame of reference used for these experiments is defined with the origin located at the center of the jet nozzle, with the *X*-axis pointing in the streamwise direction (the direction of flow), the *Y*-axis pointing vertically up and the *Z*-axis pointing laterally completing the right hand set.

A total of 10 crossflow cases were studied with 2 values of *Re* and 5 values of *UR* for each *Re*. Table 3.1 lists these test conditions. The values of *UR* used were 0.2, 0.5, 1, 2 and 5. Equation 3.3, shows that $UR < 1$ implies that $U_u < U_b$ and vice versa. The two values of *Re* were 1.3×10^5 for cases 1-5 and 1.9×10^5 for cases 6-10. The corresponding values of *We* were 50 and 100 for cases 1-5 and 6-10 respectively. Case 8 with $We = 100.57$ and $UR = 1.03$ was considered to be

the baseline crossflow for the study as this case is close to a uniform crossflow. PIV results were used to obtain the variation of the crossflow velocity and of turbulence with height.

Table 3.1 Test Conditions for Shear-Laden Crossflow

Case No	*We*	*UR*	m_{cf}	U_u	U_b	U_{avg}	*Re*	$(dU)_y$
			(kg/min)	(m/s)	(m/s)	(m/s)		
1	51.46	0.19	3.6	25.67	133.88	79.78	1.36E+05	-6.56
2	49.84	0.49	3.54	51.34	105.68	78.51	1.34E+05	-3.8
3	49.5	1.02	3.53	79.07	77.42	78.24	1.34E+05	0.14
4	50.89	2.06	3.57	106.96	51.85	79.41	1.35E+05	3.62
5	51.67	5.11	3.6	133.71	26.17	79.94	1.37E+05	6.98
6	101.81	0.19	5.06	36.32	188.11	112.21	1.92E+05	-8.8
7	100.68	0.48	5.03	72.39	150.79	111.59	1.91E+05	-4.67
8	100.57	1.03	5.02	113.3	109.96	111.63	1.90E+05	0.12
9	100.9	2.05	5.03	150.31	73.31	111.81	1.91E+05	4.34
10	102.84	5.07	5.08	188.59	37.18	112.88	1.93E+05	8.99

Once the crossflow has been characterized, the behavior of liquid jets injected in the crossflow needs to be investigated. PIV measurements were conducted in the same plane as the crossflow, which also happens to be the jet centerplane. 4 values of q were tested for each of the 10 crossflow cases, leading to a total of 40 cases studied. These cases are listed in Table 3.2. The case numbers used for jet studies reflect the crossflow test case numbers followed by letters "a" to "d" to represent the value of q used. Case 8b with a crossflow equivalent to case 8 (We = 99.46, UR = 1.04) and q = 10.07 was selected as the baseline jet case. Mie-Scattering images obtained from PIV were used to study jet penetration, while PIV results yielded droplet velocity distribution in the centerplane.

The PIV studies for jets were followed by PDPA studies for a few select cases to investigate the atomization of the jets. A total of 12 cases were selected and are listed in Table 3.3. The quantities of interest were the volume flux distribution, which indicates the spread of the jet, and the SMD, which indicates the extent of atomization of the jet. For each test condition, PDPA mea-

Table 3.2 Test Cases for PIV studies of Jet in Shear-Laden Crossflow

Case No	*We*	*UR*	*q*	*Re*	m_{cf}	m_j	U_u	U_b	U_{avg}	*V*
					(kg/min)	(kg/min)	(m/s)	(m/s)	(m/s)	(m/s)
1a	50.07	0.19	5	1.34E+05	3.54	0.071	25.49	132.18	78.84	6.02
1b	50.07	0.19	10.01	1.34E+05	3.54	0.1	25.49	132.18	78.84	8.51
1c	50.07	0.19	19.95	1.34E+05	3.54	0.141	25.49	132.18	78.84	12.02
1d	50.07	0.19	39.89	1.34E+05	3.54	0.199	25.49	132.18	78.84	16.99
2a	51.07	0.48	4.97	1.36E+05	3.59	0.071	51.79	107.02	79.4	6.06
2b	51.07	0.48	9.94	1.36E+05	3.59	0.101	51.79	107.02	79.4	8.56
2c	51.07	0.48	19.61	1.36E+05	3.59	0.141	51.79	107.02	79.4	12.03
2d	51.07	0.48	39.15	1.36E+05	3.59	0.2	51.79	107.02	79.4	17
3a	49.63	1.04	5.09	1.34E+05	3.54	0.071	79.58	76.83	78.2	6.04
3b	49.63	1.04	10.14	1.34E+05	3.54	0.1	79.58	76.83	78.2	8.53
3c	49.63	1.04	20.21	1.34E+05	3.54	0.141	79.58	76.83	78.2	12.04
3d	49.63	1.04	40.45	1.34E+05	3.54	0.2	79.58	76.83	78.2	17.04
4a	51.09	2.09	4.9	1.36E+05	3.59	0.071	107.39	51.31	79.35	6.02
4b	51.09	2.09	9.73	1.36E+05	3.59	0.1	107.39	51.31	79.35	8.48
4c	51.09	2.09	19.63	1.36E+05	3.59	0.141	107.39	51.31	79.35	12.04
4d	51.09	2.09	39.05	1.36E+05	3.59	0.199	107.39	51.31	79.35	16.99
5a	51	5.11	4.94	1.36E+05	3.59	0.071	132.61	25.94	79.28	6.03
5b	51	5.11	9.91	1.36E+05	3.59	0.1	132.61	25.94	79.28	8.55
5c	51	5.11	19.44	1.36E+05	3.59	0.141	132.61	25.94	79.28	11.97
5d	51	5.11	39.36	1.36E+05	3.59	0.2	132.61	25.94	79.28	17.04
6a	101.98	0.2	4.87	1.92E+05	5.07	0.099	36.7	187.71	112.2	8.47
6b	101.98	0.2	9.72	1.92E+05	5.07	0.141	36.7	187.71	112.2	11.97
6c	101.98	0.2	19.63	1.92E+05	5.07	0.2	36.7	187.71	112.2	17.01
6d	101.98	0.2	39.06	1.92E+05	5.07	0.282	36.7	187.71	112.2	24
7a	100.18	0.48	4.95	1.91E+05	5.03	0.099	72.35	149.87	111.11	8.47
7b	100.18	0.48	10.07	1.91E+05	5.03	0.142	72.35	149.87	111.11	12.08
7c	100.18	0.48	19.94	1.91E+05	5.03	0.199	72.35	149.87	111.11	16.99
7d	100.18	0.48	39.57	1.91E+05	5.03	0.281	72.35	149.87	111.11	23.94
8a	99.46	1.04	4.98	1.90E+05	5.01	0.099	113.06	108.35	110.7	8.46
8b	99.46	1.04	10.07	1.90E+05	5.01	0.141	113.06	108.35	110.7	12.03
8c	99.46	1.04	20.24	1.90E+05	5.01	0.2	113.06	108.35	110.7	17.06
8d	99.46	1.04	40.23	1.90E+05	5.01	0.282	113.06	108.35	110.7	24.05
9a	101.23	2.07	4.95	1.91E+05	5.05	0.1	150.83	72.75	111.79	8.51
9b	101.23	2.07	9.92	1.91E+05	5.05	0.141	150.83	72.75	111.79	12.05
9c	101.23	2.07	19.79	1.91E+05	5.05	0.2	150.83	72.75	111.79	17.02
9d	101.23	2.07	39.41	1.91E+05	5.05	0.282	150.83	72.75	111.79	24.02
10a	103.78	5.1	4.81	1.94E+05	5.11	0.1	189.27	37.11	113.19	8.5
10b	103.78	5.1	9.65	1.94E+05	5.11	0.141	189.27	37.11	113.19	12.03
10c	103.78	5.1	19.34	1.94E+05	5.11	0.2	189.27	37.11	113.19	17.04
10d	103.78	5.1	38.52	1.94E+05	5.11	0.282	189.27	37.11	113.19	24.04

surements were carried out in 3 planes, the center plane and 2 cross-sectional planes at 10 mm and 25 mm downstream of the jet nozzle (origin). The case numbers for PDPA measurements are indicated by adding the letter "d" to the jet PIV case number, so that PDPA studies for the base-line jet are represented by case number 8bd.

Table 3.3 Test Cases for PDPA studies of Jet in Shear-Laden Crossflow

Case No	*We*	*UR*	*q*	*Re*	m_{cf}	m_j	U_u	U_b	U_{avg}	V
					(kg/min)	(kg/min)	(m/s)	(m/s)	(m/s)	(m/s)
6bd	100.88	0.2	9.9	1.93E+05	5.09	0.141	36.66	184.13	110.39	12.02
6cd	101.78	0.2	19.75	1.93E+05	5.1	0.2	37.07	185.61	111.33	17.04
7bd	101.72	0.5	9.82	1.94E+05	5.11	0.141	74.26	147.66	110.96	12.02
7cd	102.6	0.5	19.59	1.95E+05	5.14	0.2	74.3	148.08	111.19	17.04
8bd	102.86	0.99	9.71	1.96E+05	5.16	0.141	110.57	111.81	111.19	12.02
8cd	99.96	0.98	20.04	1.92E+05	5.08	0.2	108.76	110.81	109.78	17.01
9bd	101.28	1.97	9.9	1.94E+05	5.12	0.141	146.24	74.09	110.16	12.04
9cd	102.01	1.98	19.67	1.95E+05	5.15	0.2	146.77	74.19	110.49	17.03
10bd	101.93	5.09	9.8	1.94E+05	5.1	0.141	186.13	36.57	111.35	12.02
10cd	102.79	5.05	19.55	1.95E+05	5.13	0.2	186.41	36.94	111.68	17.04

3.2 Shear-Laden Crossflow: Results and Discussion

As described in section 3.1.1, PIV measurements were conducted in an *XY* plane passing through the origin. 200 image pairs were captured for each test condition. The resulting instantaneous velocity maps were averaged to obtain the distribution of streamwise (U_x) and transverse (U_y) velocity components. The PIV software, Davis, can also calculate turbulence in the measurement plane from instantaneous velocities. Turbulent kinetic energy, KE_{turb}, was chosen to represent crossflow turbulence. The effect of crossflow parameters, (*We*, *UR*) on U_x, U_y and KE_{turb} was investigated.

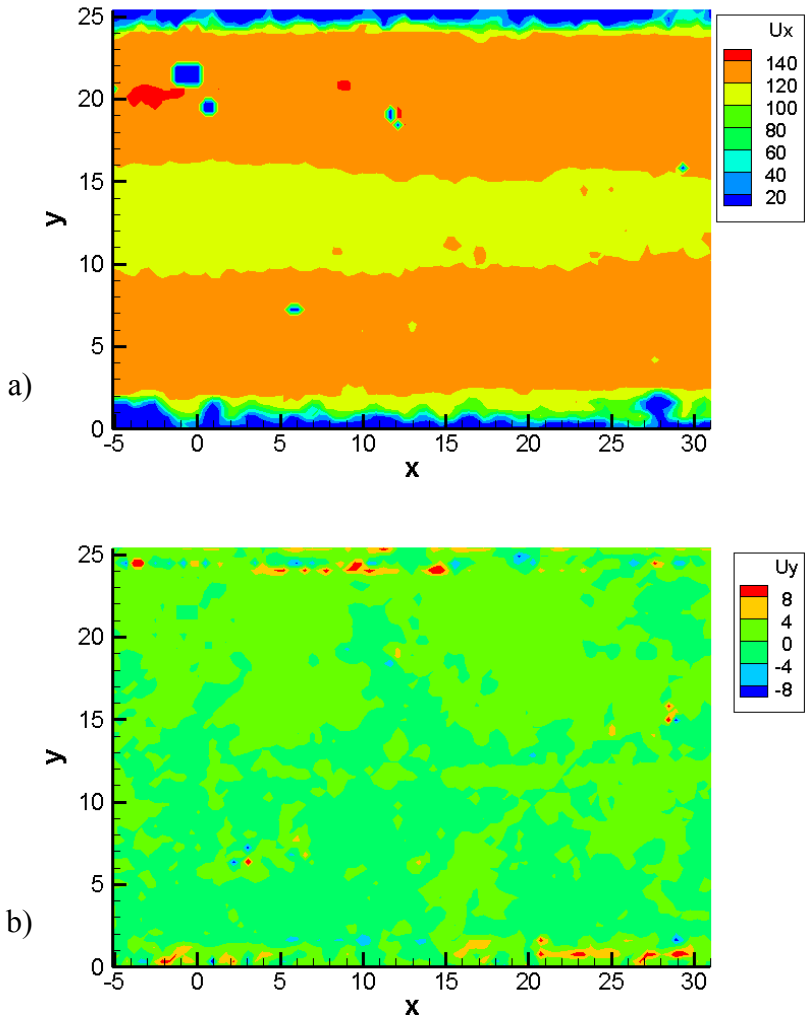

Figure 3.1 Crossflow Velocity distribution in the centerplane for the baseline crossflow, Case 8, We = 100.57, UR = 1.03, a) U_x, b) U_y

3.2.1 Crossflow Velocity Distribution

From PIV result, the distribution of velocity in the measurement plane is obtained. The visualization software, Tecplot can be used to plot either the 2-D velocity vectors, or contours of the total velocity or one of its components. Figure 3.1 shows the distribution of averaged U_x and U_y for the baseline crossflow test condition, Case 8. Since case 8 has UR = 1.03, the inlet velocities of

both streams are nearly equal, which is also observed in the U_x distribution. Now since the height of the chamber is 25.4 mm, a location of y = 12.7 mm marks the center of the chamber height. Around this height, a narrow band with lower velocity is observed. At the inlet of the test chamber the two airstreams were separated by 3.17 mm (1/8 inch), which is the thickness of the partition at the exit of the straightener section. Then a wake will form downstream of the partition. At the wake, there occurs mixing between the air from the upper and the lower streams, leading to the formation of the shear layer. This mixing creates a region where the streamwise component of velocity, U_x is lower than the surrounding region. From Figure 3.1b, it can be seen that U_y is nearly zero throughout the plane. Similar observations were observed for the remaining crossflow cases. Thus U_y is negligible as compared to U_x, which is to be expected, considering that the bulk of the crossflow motion is in the streamwise (X) direction. From here on, U_y is neglected from any further discussion, and the crossflow velocity, U will be considered to be equivalent to its streamwise component, U_x.

Figure 3.2 plots the contours of U_x for cases 6-7 and 9-10, which have the same *We* as the baseline crossflow. The velocity ratio, *UR* for cases 6, 7, 9 and 10 is 0.19, 0.48, 2.05 and 5.07 respectively. The values of *UR* indicate that for case 6, U_b is 5 times U_u while for case 10 U_u is 5 times U_b. Then the U_x distribution of case 6 can ideally be expected to be a mirror image of that for case 10, with higher velocities occurring in the lower portion of the chamber for case 6 and in the upper portion for case 10. Figures 3.2a and d, show that this is indeed the case. A similar relation is observed between the U_x distributions for cases 7 and 9 (Figures 3.2b, c).

Now cases 6-10 have the same *We*, hence the same average velocity. The only difference is the magnitudes of U_u and U_b. From Figures 3.1 and 3.2, it can be seen that the difference between U_u and U_b increases as the magnitude of *UR* moves away from 1, in either direction. As the differ-

ence between U_u and U_b increases, a higher rate of momentum exchange and higher turbulence in the shear layer is expected. Thus it can be inferred that the "*strength*" of the shear layer increases with the difference between U_u and U_b. In other words, the strength of the shear layer increases if *UR* increases (if > 1) or decreases (if < 1).

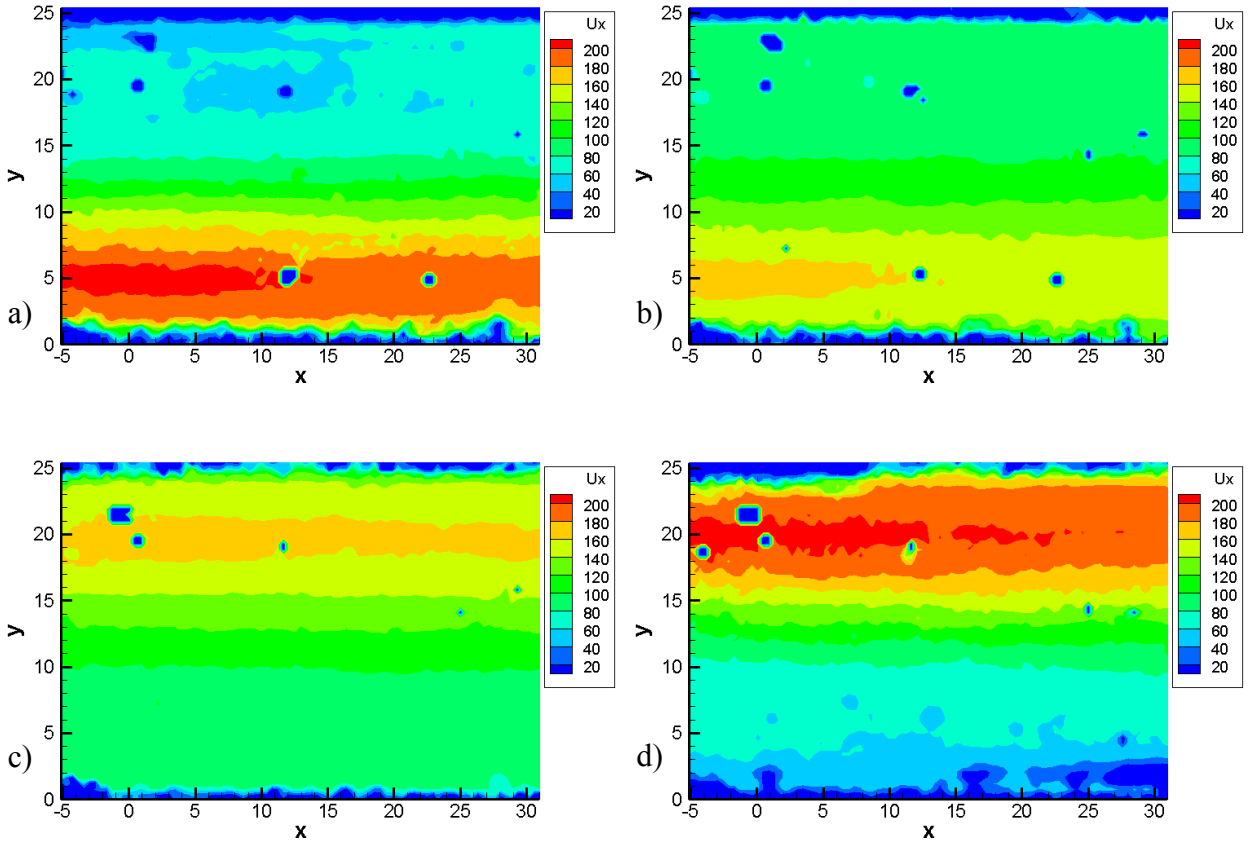

Figure 3.2 Contours of U_x in the centerplane, a) Case 6, *We* = 101.81, *UR* = 0.19, b) Case 7, *We* = 100.68, *UR* = 0.48, c) Case 9, *We* = 100.9, *UR* = 2.05, d) Case 6, *We* = 102.84, *UR* = 5.07,

As the crossflow progresses downstream, additional momentum exchange occurs within the shear layer. This causes a redistribution of the momentum, reducing velocity in the high velocity region and increasing the velocity in the low velocity region. Thus the "*strength*" of the shear layer can be said to decrease with streamwise distance. This is evident in Figure 3.2, especially for cases 6 and 10.

3.2.2 Crossflow Velocity Profiles at the Location of Jet Injection

Figure 3.2, shows that though U_x changes with x, the change occurs gradually and can be neglected if the region of interest has a short streamwise span, like the near-field of the jet. Thus the significant variation in U_x is in the y-direction. To study this more closely, the variation of U_x with y at the streamwise location of $x = 0$ (origin) was extracted from the PIV results. Figure 3.3 plots U_x against y for cases 6-10, thus showing the effect of UR on U_x. From the velocity profiles the boundary layer is seen to be approximately 3 mm thick on both the top and bottom walls at $x = 0$. The U_x profile for the baseline crossflow, case 8 clearly shows the velocity deficit around the center of the height. Figure 3.3 reinforces the notion that U_x increases with y for $UR > 1$ and decreases with y for $UR < 1$. Also, it is evident from Figure 3.3 that the absolute magnitudes of the gradient of U_x for cases 6 and 10 are higher than those for cases 7 and 9, respectively, indicating that the strength of the shear layer depends on UR.

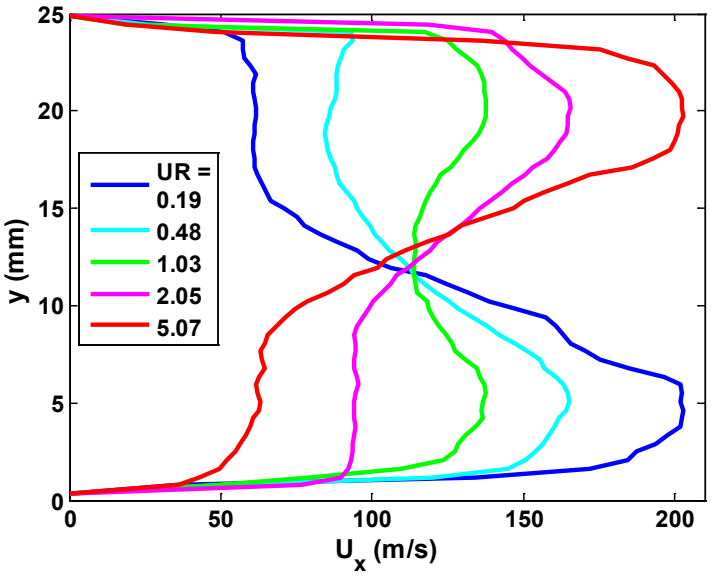

Figure 3.3 U_x profiles at $x = 0$ for crossflow cases 6-10 ($We \cong 100$)

Table 3.4 Linear fits for U_x

Case No	*We*	*UR*	*Re*	$U_{x,\,avg}$ (m/s)	$(dU)_y$	R^2
1	51.46	0.19	1.36E+05	91.32	-6.56	0.9294
2	49.84	0.49	1.34E+05	85.89	-3.8	0.93
3	49.5	1.02	1.34E+05	93.09	0.14	0.0229
4	50.89	2.06	1.35E+05	91.59	3.62	0.9078
5	51.67	5.11	1.37E+05	91.94	6.98	0.9203
6	101.81	0.19	1.92E+05	117.81	-8.8	0.904
7	100.68	0.48	1.91E+05	117.78	-4.67	0.8929
8	100.57	1.03	1.90E+05	126.79	0.12	0.0064
9	100.9	2.05	1.91E+05	123.5	4.34	0.8868
10	102.84	5.07	1.93E+05	121.81	8.99	0.9185

Figure 3.3 shows that the profiles of U_x are quasi-linear in nature. The profiles are nearly linear near the center of the chamber, with non-linear regions near the upper and lower walls. The only exception is case 6 with the velocity deficit near the center of the height. Then, linear fits can be used to describe the change in U_x without significant loss of information. In addition to simplifying the velocity distribution, this also creates a quantifiable representation of U_x which will be used for the analysis of jet penetration in section 3.4.

The linear fits for U_x were obtained using linear regression in Matlab. The boundary layer regions ($y \leq 2$ mm, $y \geq 23$ mm) were excluded from the linear regression as they would bias the velocity profiles, producing a non-representative slope. The results of the linear regression are listed in Table 3.4. The slope of the velocity gradient is denoted by $(dU)_y$, which is defined as shown in equation 3.5. Table 3.4 also lists a representative average velocity, $U_{x,\,avg}$, which is the magnitude of the linearized U_x at a height of $y = 12.5$ mm. Thus the U_x profile can be represented by $(dU)_y$ and $U_{x,\,avg}$. Good fits were obtained for all cases except the cases with $UR \cong 1$ (cases 3, 8), where the presence of the velocity deficit reduces the magnitude of the R^2 parameter. Now, $U_{x,\,avg}$ from Table 3.4 will be higher than U_{avg} from Table 3.1 as the boundary layers were neg-

lected while calculating $U_{x,\,avg}$. Figure 3.4 plots the U_x profile for case 7 along with the corresponding linear fit.

$$(dU)_y = \frac{dU_x}{dy} \tag{3.5}$$

Table 3.4, shows that the absolute magnitude of the velocity gradient, $(dU)_y$ increases with *We*. Thus $(dU)_y$ changes from 6.98 for *We* = 51.67 (case 5, *UR* = 5.11) to 8.99 for *We* = 102.84 (case 10, *UR* = 5.07). Then the "strength" of the shear layer can be said to increase with *We*.

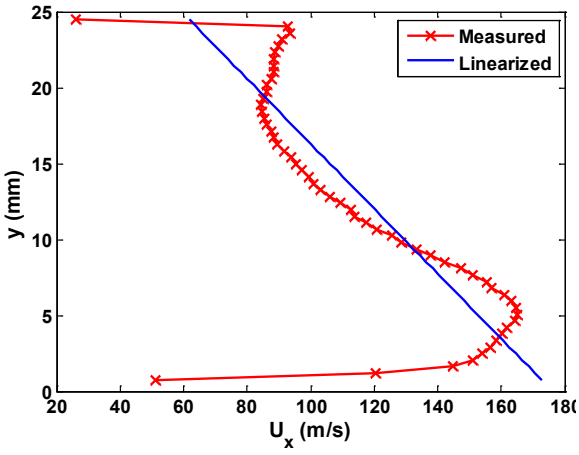

Figure 3.4 Linearization of U_x: Case 7, *We* = 100.68, *UR* = 0.48

3.2.3 Crossflow Turbulence at the Location of Jet Injection

The shear layer, which is an essential part of the crossflow, is made up of turbulent mixing between air from the two component airstreams. Hence, there is a need to study turbulence levels to complete the understanding of the crossflow.

The PIV software, Davis, can calculate turbulence parameters from the instantaneous velocity. Normalized turbulent kinetic energy, KE_{turb}, defined in equation 3.6, was chosen to represent

turbulence levels in the crossflow. Profiles of KE_{turb} at the origin were extracted from the KE_{turb} distributions.

$$KE_{turb} = \frac{u_x'^2 + u_y'^2}{\left(U_{x,avg}\right)^2} \tag{3.6}$$

Figure 3.5a shows the KE_{turb} profile for the baseline crossflow, case 8. Low KE_{turb} is observed in the bulk of the flow, with magnitudes of the order of 0.01, or 1%. Higher turbulence is observed in the boundary layer with a KE_{turb} magnitude of 10%.

Figure 3.5b compares KE_{turb} profiles of cases 6-7 ($We \cong 100$, $UR < 1$) with that for case 8. For cases 6-7, highest KE_{turb} values are observed in the region between the height center and the location of the peak U_x value ($y \cong 7$ mm). Within the shear layer, KE_{turb} increases continuously as one moves down from the low energy upper stream to the high energy lower stream. Also, case 6, which is considered to have a "stronger" shear layer, is observed to have higher KE_{turb} magnitudes as compared to case 7.

Figure 3.5c which plots KE_{turb} profiles for cases 8-10 ($We \cong 100$, $UR \geq 1$) shows similar results, with higher KE_{turb} for case 10 and regions of high KE_{turb} in the upper half of the crossflow for cases 9-10.

Figure 3.6 compares the KE_{turb} profiles for cases 4 and 9 (Figure 3.6a, $UR \cong 2$) and cases 5 and 10 (Figure 3.6b, $UR \cong 5$) to demonstrate the effect of We on KE_{turb}. Figure 3.6a, shows that magnitude of KE_{turb} for cases 4 and 9 are very close, though the peak KE_{turb} magnitude for case 4 ($We = 50.89$) is slightly higher than that for case 9 ($We = 100.9$). From Figure 3.6b, it can be seen that the magnitudes of KE_{turb} for cases 5 and 10 are also close. Recognizing that the size of the shear layer is reflected by the height of the region of high KE_{turb}, the height of shear layer for case 10

(We = 102.84) is observed to be higher as compared to case 5 (We = 51.67). Thus, it can be inferred that for lower We, high KE_{turb} is observed near the height center. For higher We, more mixing occurs so that the shear layer is wider, and also KE_{turb} exhibits a flatter distribution as compared to the lower We case.

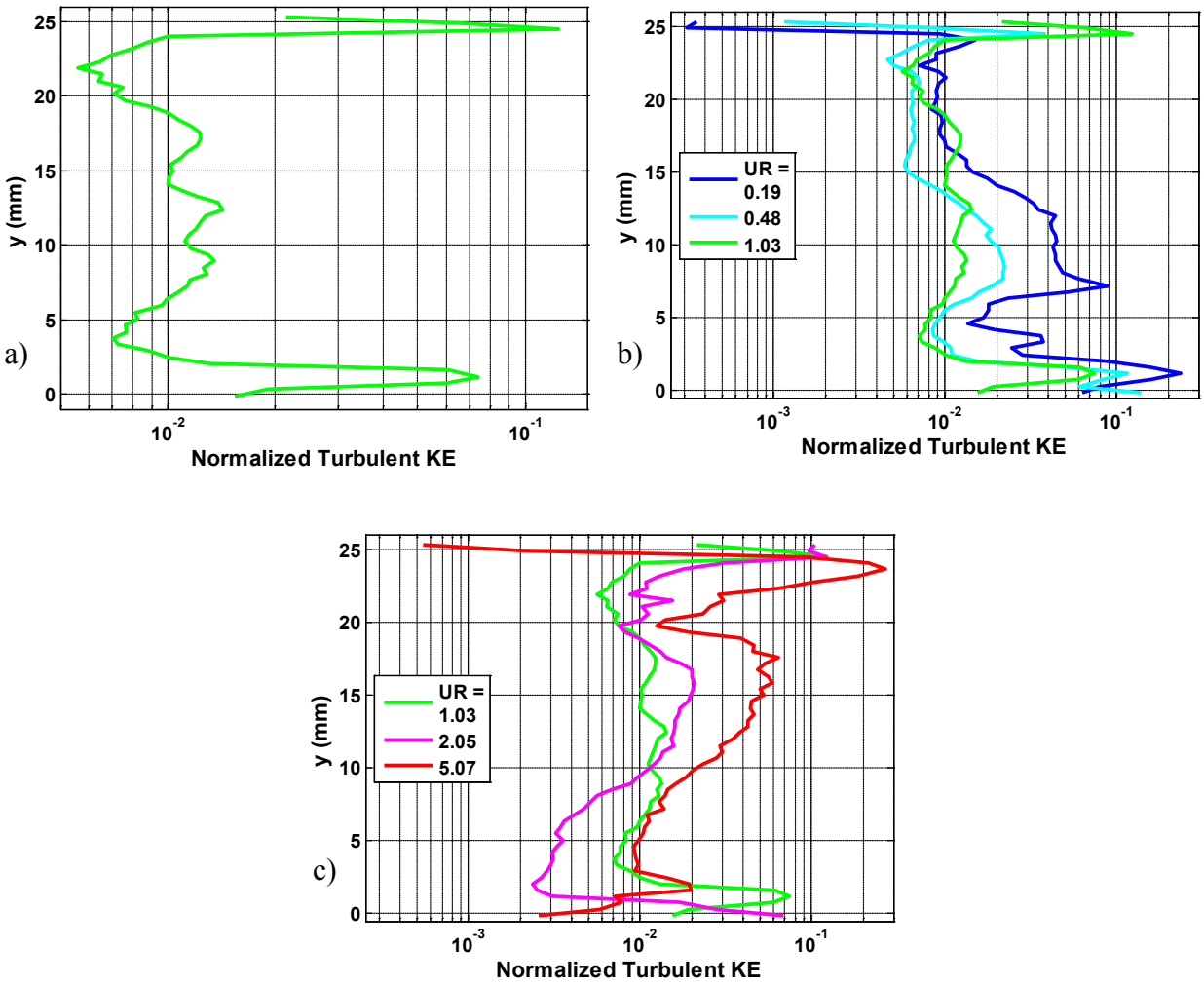

Figure 3.5 Profiles of KE_{turb} at the origin. a) Baseline crossflow, case 8 (We = 100.57, UR = 1.03), b) Cases 6-8 ($We \cong 100$, $UR \leq 1$), c) Cases 8-10 ($We \cong 100$, $UR \geq 1$)

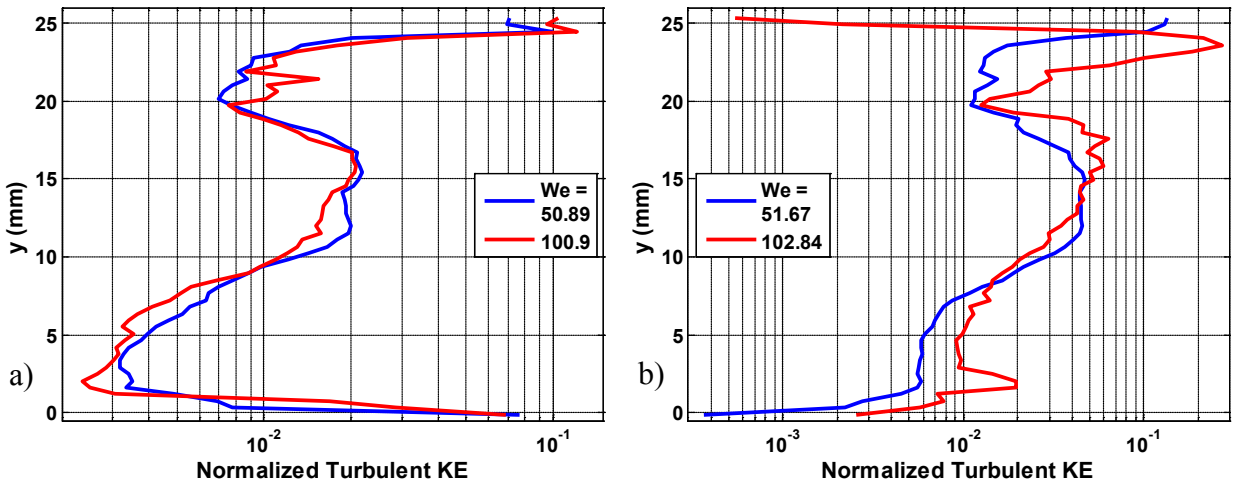

Figure 3.6 Effect of *We* on KE_{turb} at the origin a) Cases 4, 9 ($UR \cong 2$), b) Cases 5, 10 ($UR \cong 5$)

3.3 Overview of Liquid Jets in Shear-Laden Crossflow

The crossflow study was followed by the study of water jets injected into the crossflow. It was shown previously that the crossflow can be represented by (*We*, *UR*). Once the crossflow is known, the jet can be completely described by the momentum flux ratio, *q*. In a manner similar to *We*, the momentum flux ratio, *q*, is defined using the average crossflow velocity, as shown in equation 3.7.

$$q = \frac{\rho_w V^2}{\rho_a \left(U_{avg}\right)^2} \tag{3.7}$$

The results and discussion for the jets are divided into three parts. Section 3.4 discusses jet penetration and proposes an empirical correlation for the penetration. In Section 3.5 droplet velocities in the jet centerplane as measured by PIV are described. Section 3.6 discusses the jet atomization by investigating the volume flux and the SMD of the jets.

3.4 Jet Penetration

For PIV study of the jets, the crossflow was kept unseeded. The water droplets from the jet scatter the PIV Laser and hence can be captured by the PIV camera. Moreover, since the size of the droplets is significantly larger than the laser wavelength, the images recorded by the PIV system are essentially Mie-Scattering images. For each jet case, 200 image pairs were captured. The raw Mie-Scattering images for each case were averaged, and the resultant image was used for jet penetration analysis. Additionally, the upper jet periphery was obtained from the average Mie Scattering Image using an in-house developed Matlab program. These jet trajectories were used to obtain an empirical correlation for the jet penetration.

3.4.1 Penetration of the Baseline Jet (case 8b)

Figure 3.7 shows the jet plume for the baseline jet, case 8b (We = 99.46, UR = 1.04, q = 10.07). Since $UR \cong 1$, jet behavior is expecte to be close to that of a jet in a uniform crossflow. Figure 3.7a shows a false-color representation of the averaged Mie-Scattering image obtained from the PIV software, Davis. We observe that the jet issues vertically out of the nozzle, and starts bending within a short distance due to the momentum of the crossflow, similar to a jet in uniform crossflow. The high Mie-Scattering intensity near the nozzle indicates the presence of the jet core. The Mie-Scattering intensity reduces with streamwise distance as the jet undergoes more atomization. By x = 15 mm, the spray plume has nearly aligned itself with the direction of the crossflow. The usual convention for discussing jet penetration, is to normalize all distances by the nozzle diameter, d (= 0.5 mm). Thus, the baseline jet is nearly aligned with the crossflow by

a streamwise distance of 30*d* (= 15 mm). The maximum penetration of the jet was observed to be approximately 15*d*.

The PIV software, Davis, can also export the Mie-Scattering image as an intensity map, which can be visualized by Tecplot. Figure 3.7b shows the intensity contours for the baseline jet using Tecplot. The intensity map was normalized by the maximum intensity in the plane, and a threshold of 10% has been applied to demarcate the jet boundary. The contours of the normalized intensity for case 8b are shown in Figure 3.7c

3.4.2 Extracting the Jet Boundary

Jet penetration has been defined in the literature using the upper periphery of the jet, the jet centerline, and the location of maximum velocity by different researchers [30]. In this study, the upper periphery of the jet, also denoted from here on as the jet trajectory, is used to define jet penetration. The jet trajectory (periphery) was obtained by a gradient search tool using specifically developed Matlab programs. The use of the intensity gradients is preferred over directly tracking the jet boundary as it enables effective elimination of isolated droplets. The procedure of obtaining the jet trajectory is described here using the baseline jet as an example.

The program initially defines an area of interest (AOI) for conducting the boundary calculations. In the streamwise direction, the AOI extends from x = -0.5: 20 mm (-1d: 40 d). The upper limit for the AOI in the transverse direction is determined from the intensity values at each y location. The lower transverse limit is set to y = 0 mm. The intensity map for the AOI generated for the baseline case is shown in Figure 3.8a. The next step is to compute the intensity gradients in the AOI. Gradients are calculated along x and y and the larger of the two absolute gradient magni-

tudes is selected. In order to ensure that only the spray plume is tracked, the gradient values at isolated droplet locations are eliminated by conducting a neighborhood search. Figure 3.8b shows a contour plot of the intensity gradients for the baseline case. The upper periphery of the jet is then determined as the uppermost location of non-zero gradients. Figure 3.8c shows the jet periphery for the baseline jet. For calculating the penetration correlations, the position coordinates were scaled by the jet diameter (d = 0.5 mm). Additionally, the origin for penetration correlations was shifted upstream by 1d to mark the origin of the upper jet periphery. Figure 3.8d shows the jet trajectory for the baseline jet in the scaled coordinate system.

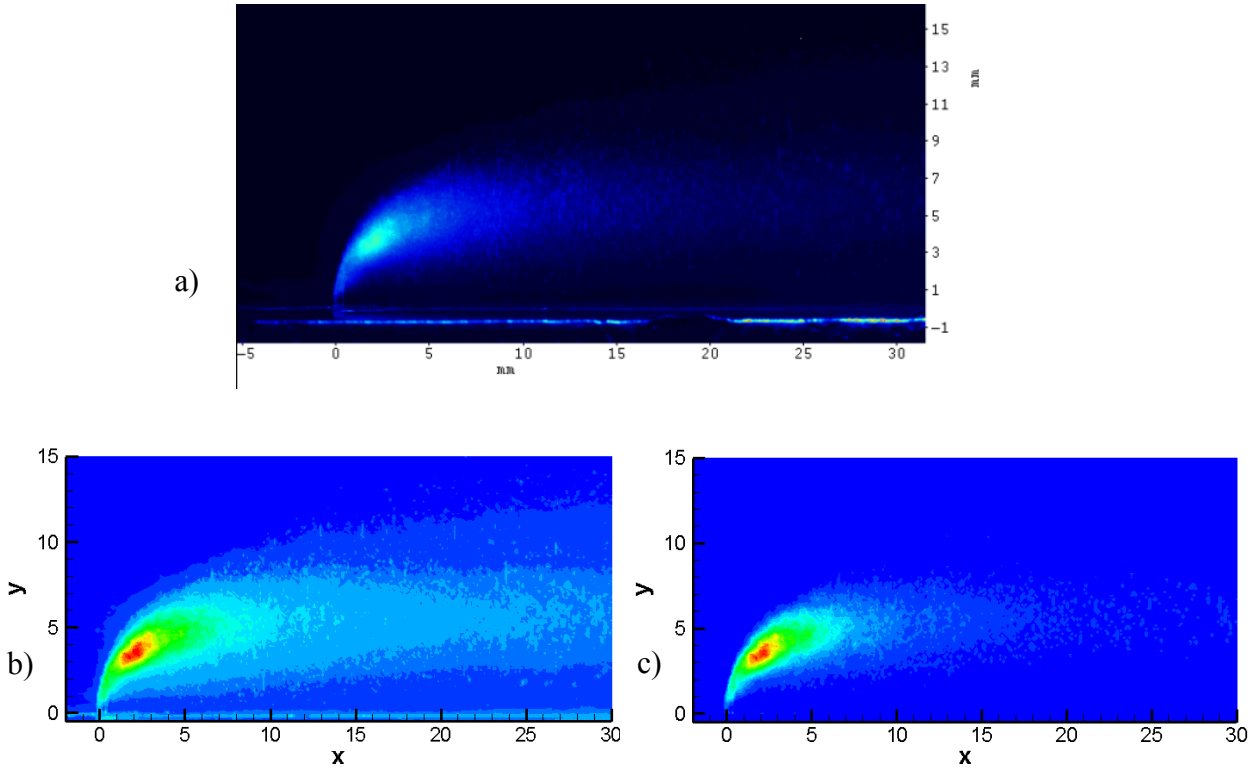

Figure 3.7 Baseline Jet, Case 8b, (We = 99.46, UR = 1.04, q = 10.07), a) Original Mie Scattering Image, b) Tecplot intensity contour plot, c) Normalized tecplot intensity contour plot

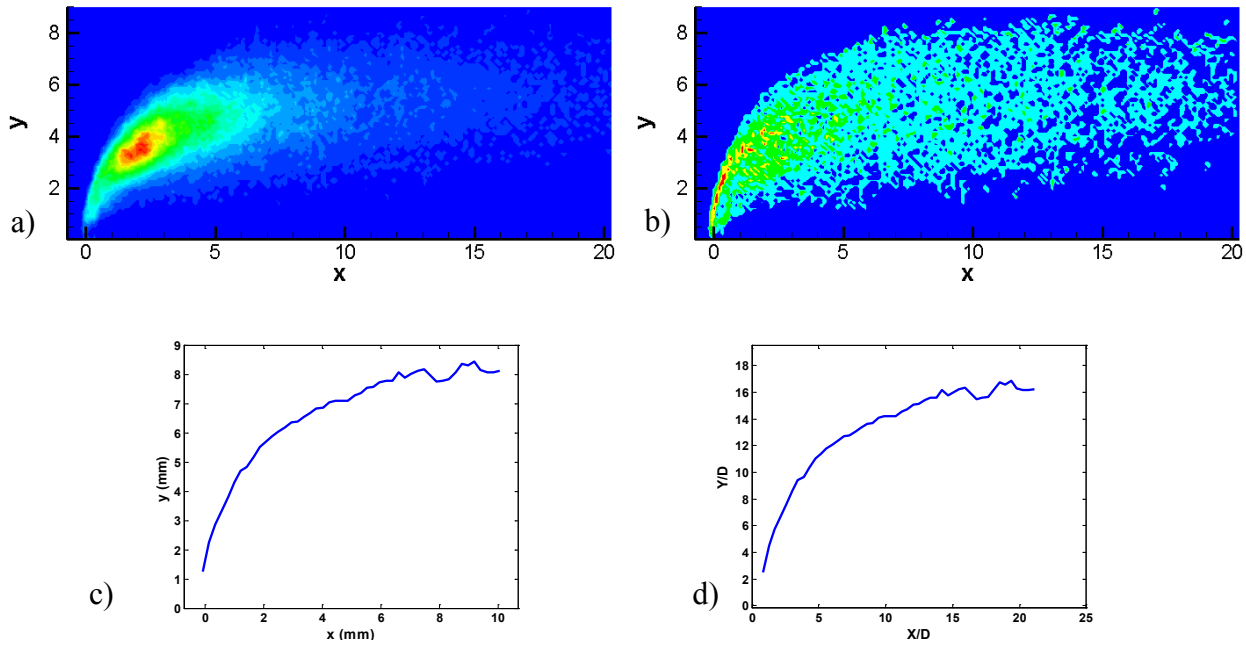

Figure 3.8 Extracting Jet Periphery for case 8b, (We = 99.46, UR = 1.04, q = 10.07), a) Area of interest, b) Gradient contour plot, c) Jet trajectory, d) Jet trajectory (scaled coordinates)

3.4.3 Effect of Crossflow Parameters (*We*, *UR*) on Jet Penetration

Figure 3.9 shows the effect of the UR on jet penetration by plotting the normalized Mie Scattering images for jets with $q \cong 10$ and $We \cong 100$ (cases 6b, 7b, 8b, 9b, 10b), which includes the baseline jet, case 8b (Figure 3.9c). The jet penetration increases as UR increases. This occurs since the local crossflow drag experienced by the jet changes with the height from the bottom wall. For $UR < 1$, the jet encounters a very high speed crossflow immediately after exiting the nozzle, consequently, the local q of the jet is low, and it undergoes rapid change in trajectory, and the overall penetration of the jet is low. However, if the local q were high enough to allow the jet to penetrate beyond the nearest high velocity crossflow region, it will experience reduced crossflow drag, so that incremental penetration for such a case can be expected to be higher than

that compared to a jet in uniform crossflow. The maximum penetration for case 6b (UR = 0.2) is 9.5d while that for case 7b (UR = 0.48) is 12d, as compared to 15d for the baseline jet. Thus reducing UR from 1.04 to 0.2 reduces the jet penetration by 37%.

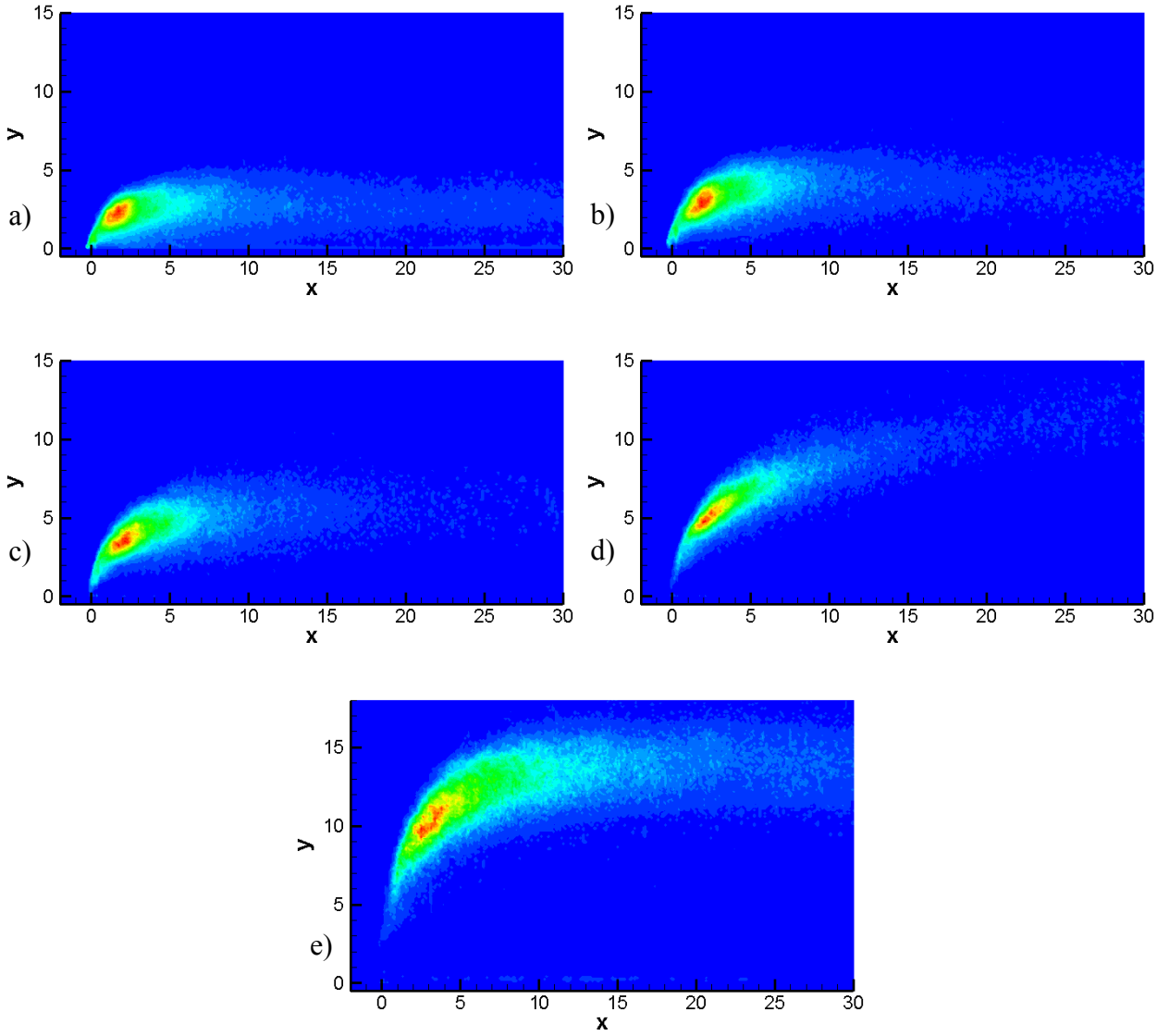

Figure 3.9 Effect of UR on Jet Penetration, a) case 6b, We = 101.98, UR = 0.2, q = 9.72, b) case 7b, We = 100.18, UR = 0.48, q = 10.07, c) case 8b (baseline jet), We = 99.46, UR = 1.04, q = 10.07, d) Case 9b, We = 101.23, UR = 2.07, q = 9.92, e) Case 10b, We = 103.78, UR = 5.1, q = 9.65

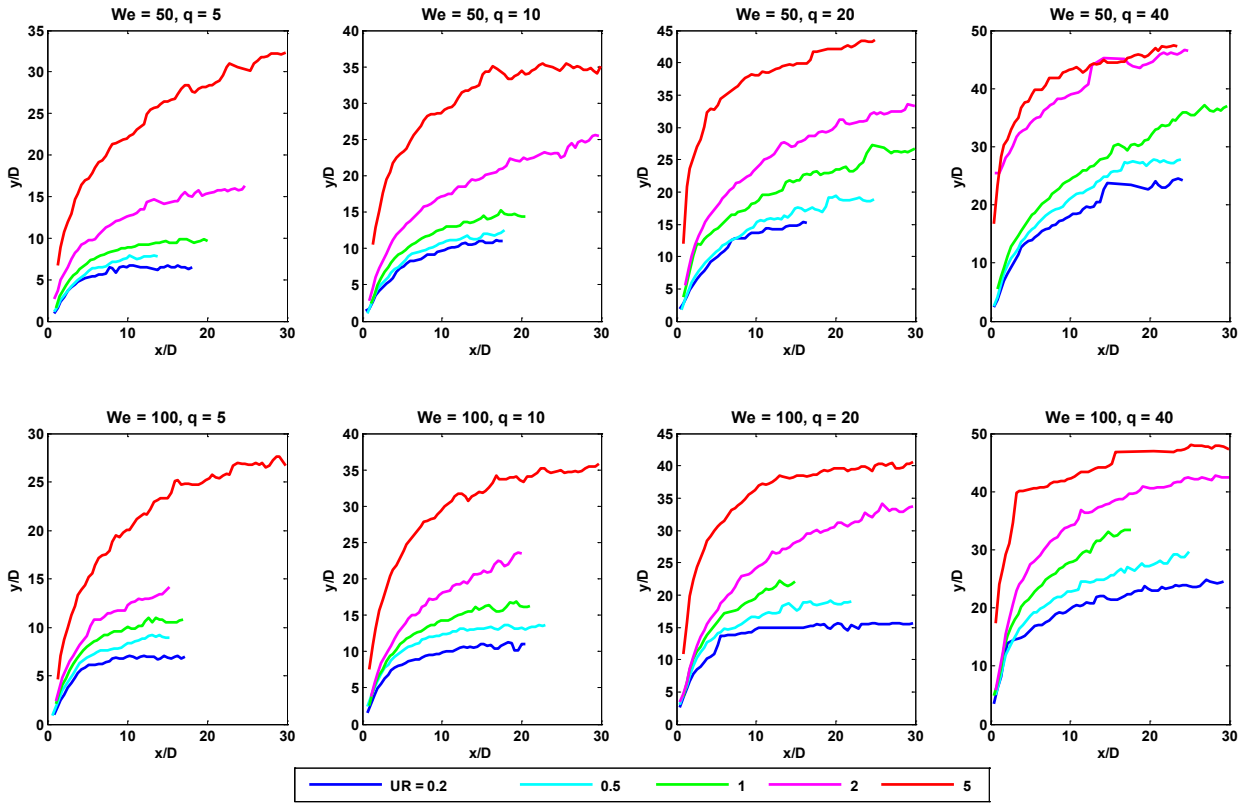

Figure 3.10 Effect of *UR* on Jet Penetration: Jet Trajectories

For $UR > 1$, the crossflow velocity near the jet nozzle is low, so that the local q is high, enabling higher penetration. Thus even for a low average q of 10, the jet reaches the upper portion of the crossflow where the velocity is high. As the jet reaches this region, the increase in the crossflow dynamic pressure accelerates the bending of the jet so that there is a rapid change in direction of the jet. Thus though the jets have high initial penetration, incremental penetration is low as compared to jets in uniform crossflow. This is especially noticeable for case 10b ($UR = 5.1$), shown in Figure 3.9e, where there is a significant increase in the change of trajectory slope as the jet penetrates above a height of 20d. For Case 9b, ($UR = 2.07$), shown in Figure 3.9d, the jet is nearly aligned with the crossflow by the time it reaches the height of 20d, so that the acceleration in the change in slope is not noticeable. The maximum penetration for Case 9b is 20d while that for Case 10b is 31d. Changing *UR* from 1 to 5 then increases the jet penetration by over 100%. Thus

UR has a big impact on jet penetration. Figure 3.10 plots the acquired jet trajectories for all 40 cases by sorting them into 8 groups each having the same (*We*, *q*) to illustrate the effect of *UR* on jet penetration.

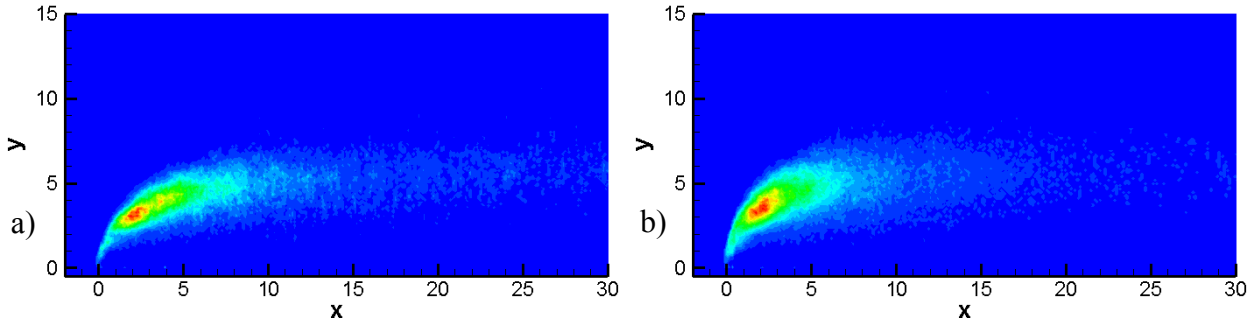

Figure 3.11 Effect of *We* on jet penetration a) Case 3b, *We* = 49.63, *UR* = 1.04, *q* = 10.14, b) Case 8b (Baseline Jet), *We* = 99.46, *UR* = 1.04, *q* = 10.07

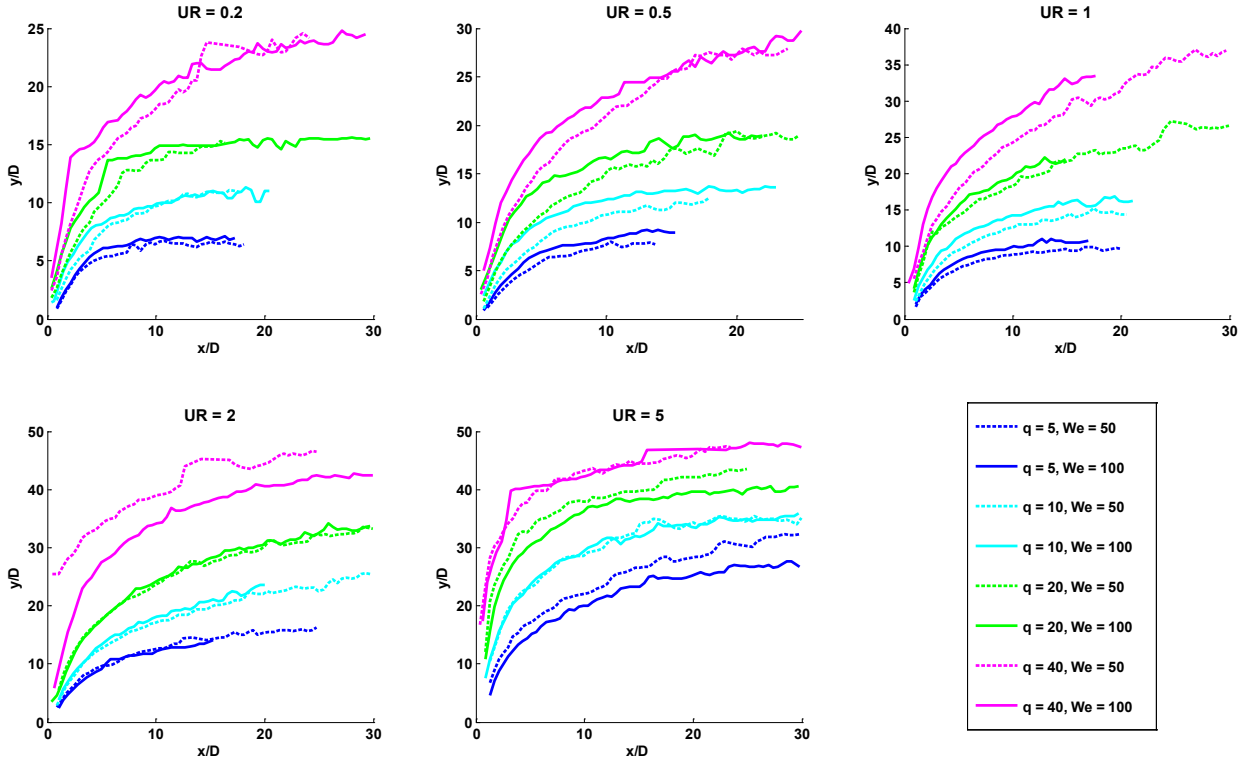

Figure 3.12 Effect of *We* on Jet penetration: Jet trajectories

Next we consider the effect of a change in *We* on jet penetration. Figure 3.11 shows the jets for case 3b (*We* = 49.63) and the baseline jet, case 8b, (*We* = 99.46), both of which feature *UR* ≅ 1, *q* ≅ 10. It can be seen that the penetrations for the two cases are nearly equal. Figure 3.12 plots the jet trajectories for all cases measured by grouping them according to *UR*. No clear trend of the effect of *We* on jet penetration is observed, with jet penetration decreasing with *We* for a few cases and increasing with *We* for the rest. In either case, the change in penetration is marginal, and it is difficult to demonstrate a clear dependence of penetration on *We*.

3.4.4 Effect of *q* on Jet Penetration

For traditional jets in crossflow, the momentum flux ratio, *q* is the chief parameter affecting jet penetration, with penetration increasing with *q*. Figure 3.13, plots the jets for cases 8a-d which have properties of *We* = 99.46, *UR* = 1.04 with *q* of 4.98, 10.07, 20.24 and 40.23 respectively. Figure 3.13 shows that jet penetration increases with an increase in *q* as expected. The effect of *q* on jet trajectories can also be observed from figure 3.12, which shows that jet penetration increased with *q* for all test conditions.

3.4.5 Penetration Correlations

The jet trajectories of all measured cases were used to fit an empirical correlation to predict jet penetration. The penetration data were limited to the near field of the jet by enforcing a limit of 30*d* in the streamwise direction.

Most of the penetration correlations present in the literature pose the transverse penetration (*y*/*d*) as a function of the streamwise distance (*x*/*d*) and the momentum flux ratio, *q*. Becker and Hassa

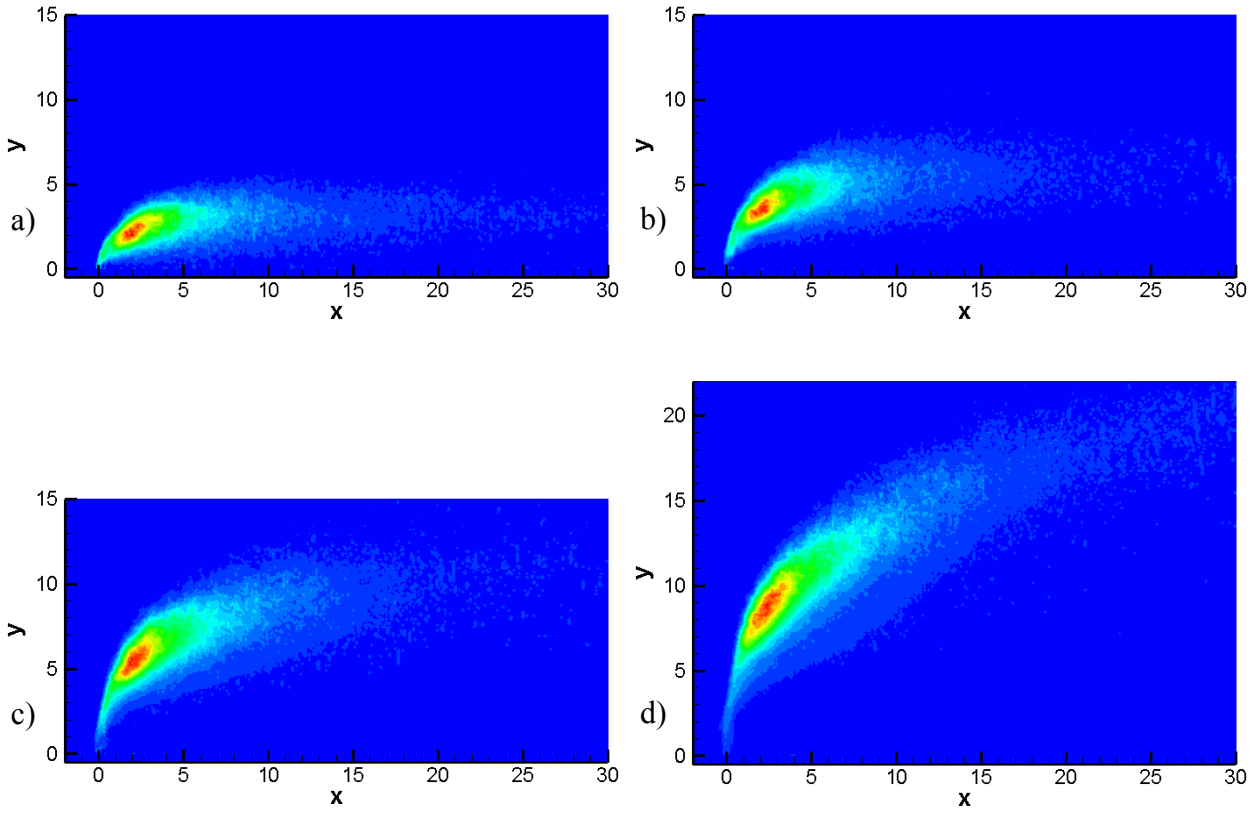

Figure 3.13 Effect of q on Jet Penetration a) Case 8a, We = 99.46, UR = 1.04, q = 4.98, b) Case 8b, We = 99.46, UR = 1.04, q = 10.07, c) Case 8c, We = 99.46, UR = 1.04, q = 20.24, d) Case 8d, We = 99.46, UR = 1.04, q = 40.23

[1] have proposed a logarithmic function for x while others, including Wu et al [28], proposed an exponential function for x. In a previous study [27], the logarithmic correlation was found to be the best fit for the penetration of a liquid jet in a uniform crossflow. Some researchers have also predicted the dependence of the penetration on the aerodynamic Weber number, We [9].

Based on these correlations, 3 different function templates were used for penetration correlations as given in equations 3.8 - 3.10. The parameters c, m, n and p in these equations are unknown constants to be fitted to the data.

$$\frac{y}{d} = c\left(\frac{x}{d}\right)^m q^n \tag{3.8}$$

$$\frac{y}{d} = c\left(\frac{x}{d}\right)^m q^n We^p \tag{3.9}$$

$$\frac{y}{d} = cq^n \ln\left(1 + m\frac{x}{d}\right) \tag{3.10}$$

The non-linear regression software package, NLREG [24], was used to fit the correlations. NLREG is a statistical analysis program that performs linear and non-linear regression analysis, surface and curve fitting. NLREG determines the values of parameters for an equation, whose form is specified, such that the resulting equation is the best fit for a set of data values.

The first set of correlations used average values of q and We. The best fit was obtained using the form of equation 3.10, with $R^2 = 0.5638$. The correlated function is given in equation 3.11. Figure 3.14a plots the predicted y/d values using equation 3.11 against the actual y/d values. Figure 3.14a shows a large spread in the data, indicating that the correlation could not predict the penetration in a satisfactory manner.

$$\frac{y}{d} = 2.17q^{0.43} \ln\left(1 + 2\frac{x}{d}\right) \tag{3.11}$$

A second set of correlations were obtained using the functional forms in equations 3.8-3.11 with local values of q and We. For this set, the best fit was obtained using the form of equation 3.10, with $R^2 = 0.5405$. The correlated function is given in equation 3.12. Figure 3.14b plots the predicted y/d values using equation 3.12 against the actual y/d values. The spread in the data from

Figure 3.14b is larger as compared to Figure 3.14a, indicating that even this correlation could not predict the penetration in a satisfactory manner.

$$\frac{y}{d} = 0.52\left(\frac{x}{d}\right)^{0.34} q^{0.34} We^{0.42} \tag{3.12}$$

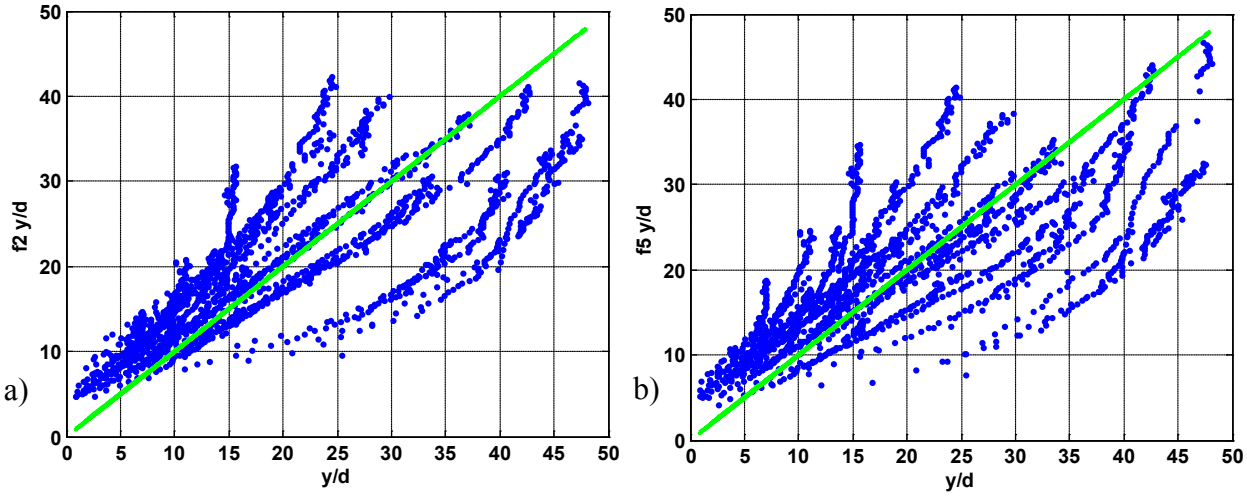

Figure 3.14 Direct Correlation, a) Constant *We*, *q* , b) Variable *We*, *q*,

Since these correlations failed to provide good predictions for the jet trajectory, a different approach to obtaining the form of the penetration correlation was sought. The basis for this approach was the analysis used by Wu et al [28]. They balanced liquid acceleration with the aerodynamic drag forces in the streamwise direction. Assuming that the streamwise component of the droplet velocity is negligible compared to crossflow velocity,

$$F_{cf} = m_j a_j$$

$$\frac{1}{2}\rho_{cf} U^2 \propto \frac{d^2 x}{dt^2}$$

Now,

$$\frac{dx}{dt} = V\frac{dx}{dy}$$

Then,

$$U^2 \propto V^2 \frac{d^2x}{dy^2}$$

Using this relation, function templates were created to relate the slope of the trajectory to the jet and crossflow parameters as shown in equations 3.13-14. The corresponding coordinate was then obtained by numerical integration.

$$\frac{dy}{dx} = c\left(\frac{x}{d}\right)^m q^n We^p \tag{3.13}$$

$$\frac{dx}{dy} = c\left(\frac{x}{d}\right)^m q^n We^p \tag{3.14}$$

The best result for this set of correlations was obtained based on the form in equation 3.13, with $R^2 = 0.5851$ and is given in equation 3.15. Figure 3.15 plots the predicted y/d values using equation 3.15 against the actual y/d values.

$$\frac{dy}{dx} = 1.8424\left(\frac{x}{d}\right)^{-0.671} q^{0.4391} We^{-0.0933} \tag{3.15}$$

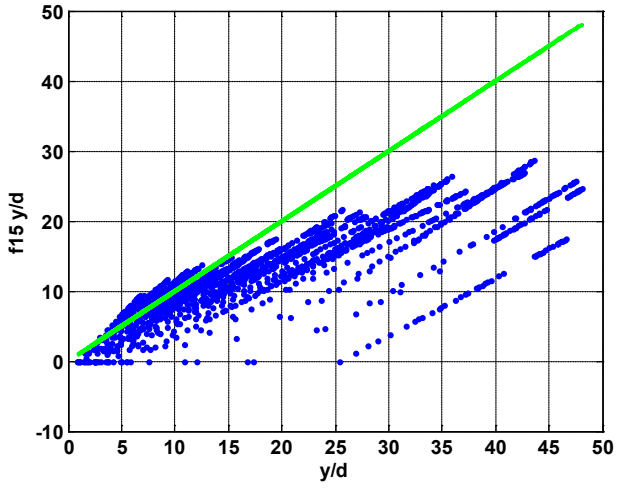

Figure 3.15 Correlation based on Equation 3.15

The correlation predicted from equation 3.15 also fails to provide a good match to the data as seen from Figure 3.15. It is believe that additional data may be necessary to generate a better correlation.

3.5 Droplet Velocities in the Jet Centerplane (PIV)

The droplet velocity distribution obtained from PIV results is considered next. The velocity distributions were obtained as velocity maps, which are visualized as vectors or as contours of individual components using Tecplot. The droplet velocity distribution in the jet centerplane and the effect of crossflow and jet parameters on the velocity distribution is studied in this section.

3.5.1 Droplet Velocity Distribution for the Baseline Jet (case 8b)

The centerplane droplet velocity distribution of a typical jet in a uniform crossflow contains high velocities near the top of the spray periphery, and a low velocity region denoting the spray core. The spray core usually consists of slow-moving, large droplets and constitutes a bulk of the volume flux of the jet. Higher velocities are observed above and below the core [9, 16, 27, 29].

The velocity distribution in the center plane for the baseline jet is shown in Figure 3.16a. The droplet velocities are observed to increase as the jet moves downstream due to the continued interaction with the crossflow. In the transverse direction, starting from the bottom wall, a small region of high velocity is observed, followed by the low velocity core. A large region of high velocities occurs above the core.

The transverse extent of the jet in the velocity plot is observed to be significantly higher than that observed in the Mie-Scattering image. The reason for this discrepancy is due to the nature of the

Mie-Scattering images. The Mie-Scattering image is an intensity map, where the intensity depends upon the total surface area of droplets crossing a given location. As a result, locations with low droplet concentrations will have low intensities. Additionally, since the images are averaged, the intensities at such locations can be very low and may get cut off due to the applied threshold. On the other hand, the process of obtaining average velocity vectors includes the velocities at all locations where at least 10 vectors were measured over the entire set of 200 images. Thus the averaging process for the velocity vectors is much more inclusive and will retail locations with low droplet concentrations. This causes the extent of the jet to appear larger in the PIV results.

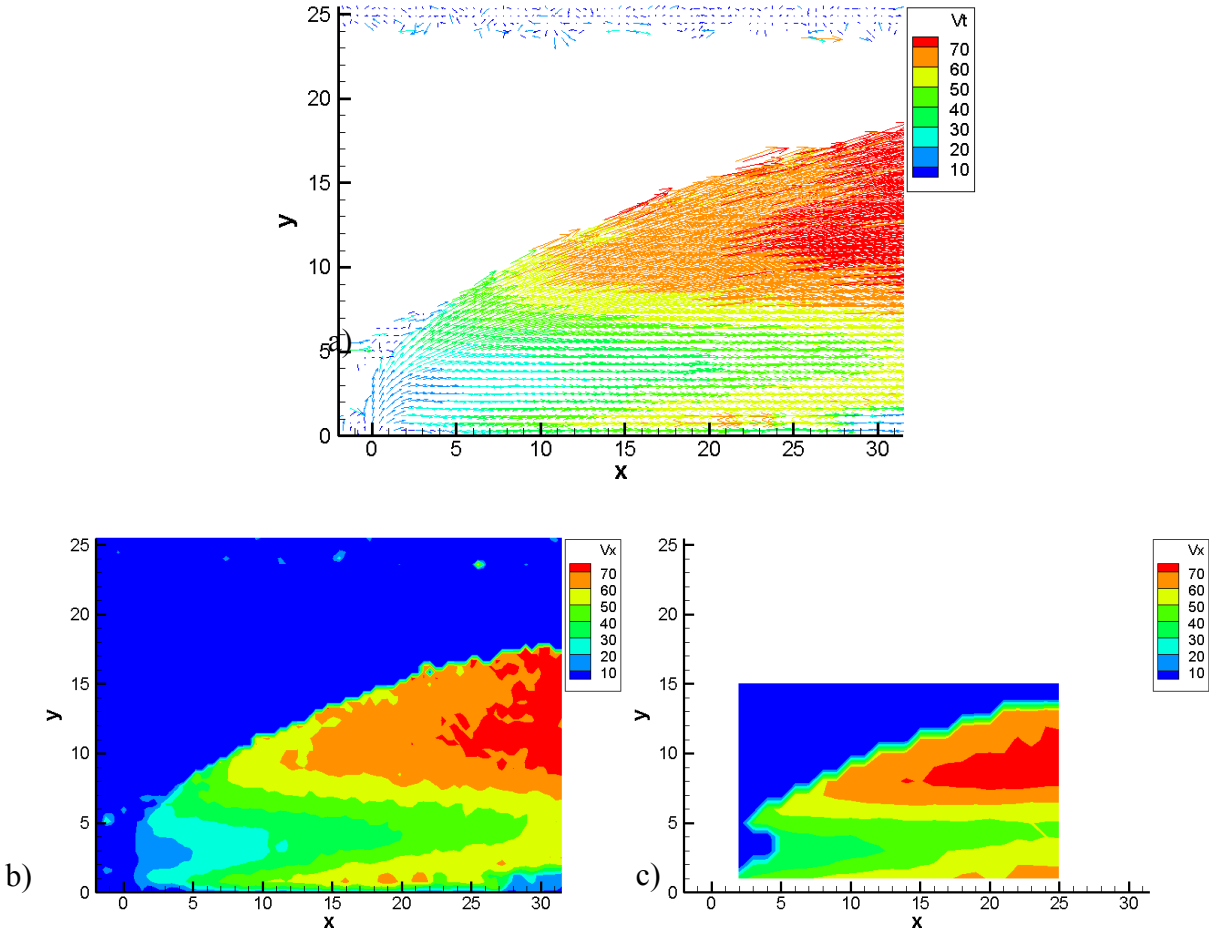

Figure 3.16 Baseline Jet, case 8b, *We* = 99.46, *UR* = 1.04, *q* = 10.07 a) Centerplane velocity vectors, b) Axial velocity, V_x contours (PIV), c) Axial velocity, V_x contours (PDPA)

Figure 3.16b plots the contours of the axial component of the droplet velocities, V_x. This figure clearly shows the presence of the spray core, which is the region with low V_x. As the jet progresses downstream, the velocity in the spray core also increases.

Figure 3.16c plots the axial velocity contours obtained for the baseline case from PDPA measurements. PDPA measurements have been restricted to only a small region of the plane due to optical access restrictions and the long time taken for the point-by-point PDPA measurements. The axial velocity distribution obtained from PDPA is qualitatively similar to that obtained from PIV, though the magnitudes of the velocity are slightly higher.

3.5.2 Effect of Crossflow Parameters (*We*, *UR*) on Jet Centerplane Velocity

The effect of crossflow parameters on the droplet velocity distribution are considered next. Figure 3.17 shows the effect of *UR* on droplet velocity, by plotting the velocity vector distribution for cases 6b, 7b, 8b, 9b and 10b respectively. These cases have $We \cong 100$ and $q \cong 10$, so that the only difference is the parameter *UR*. Values of *UR* for cases 6b, 7b, 8b, 9b, and 10b are 0.2, 0.48, 1.04, 2.07 and 5.1 respectively. The cases plotted in Figure 3.17 are identical to those in Figure 3.9. Similar to the observations in Section 3.4.2, the jet penetration increases with *UR* as seen by the transverse location of the spray core as well as the location of the spray periphery. As *UR* increases, the extent of the spray above the spray core is seen to decrease.

In order to study the droplet velocity distribution in more detail, the variation of the axial, (V_x) and the transverse (V_y) components with y of all 5 cases from Figure 3.17, at an axial location of $x/d = 30$ ($x = 15$ mm) have been plotted in Figures 3.18a and b. We observe that for all 5 cases, the axial velocity profile exhibits a concave shape with high velocities above and below the

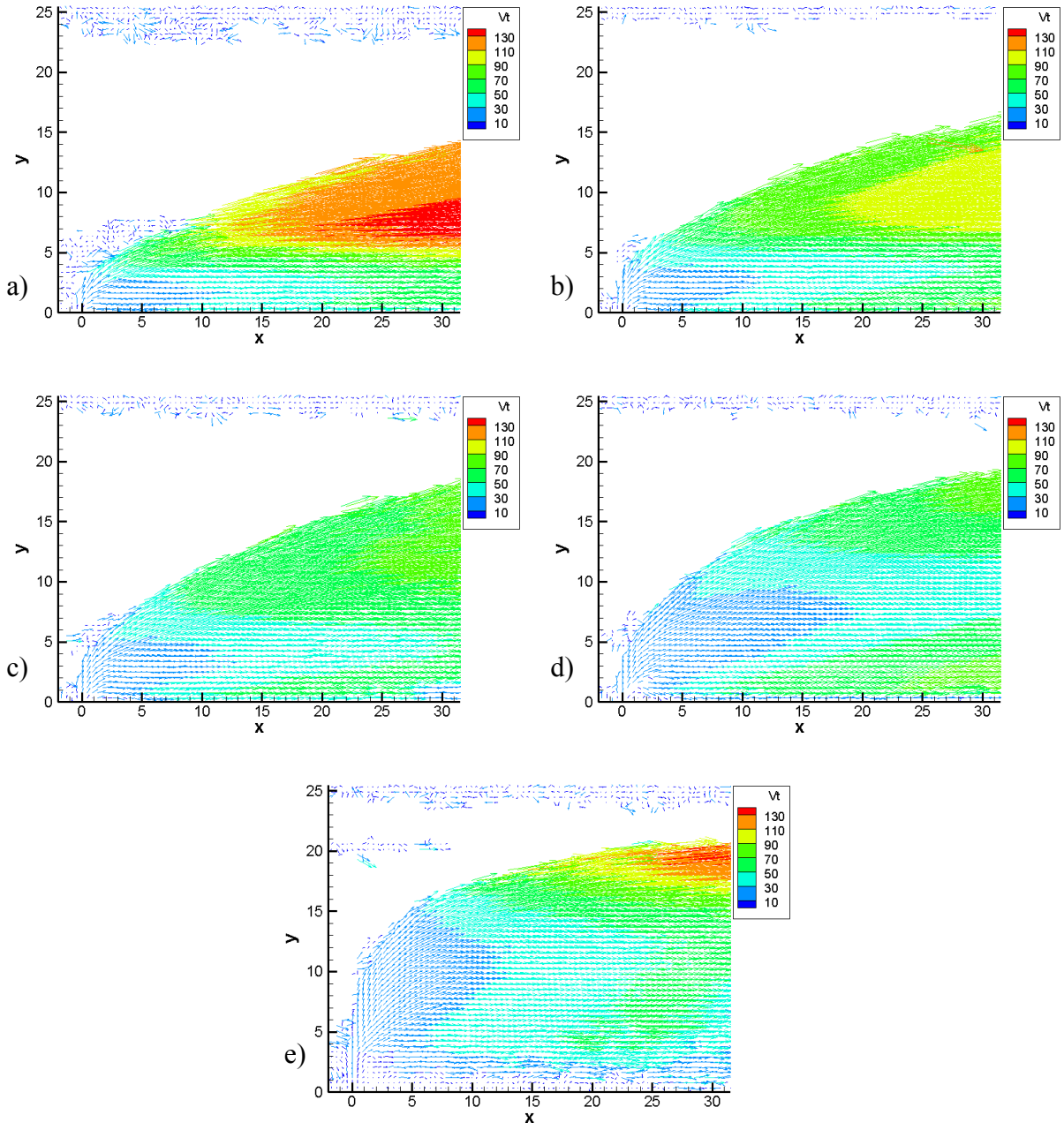

Figure 3.17 Effect of *UR* on Centerplane velocity, a) Case 6b, *We* = 101.98, *UR* = 0.2, *q* = 9.72, b) Case 7b, *We* = 100.18, *UR* = 0.48, *q* = 10.07, c) Case 8b (Baseline Jet), *We* = 99.46, *UR* = 1.04, *q* = 10.07 , d) Case 9b, *We* = 101.23, *UR* = 2.07, *q* = 9.92, e) Case 10b, *We* = 103.78, *UR* = 5.1, *q* = 9.65

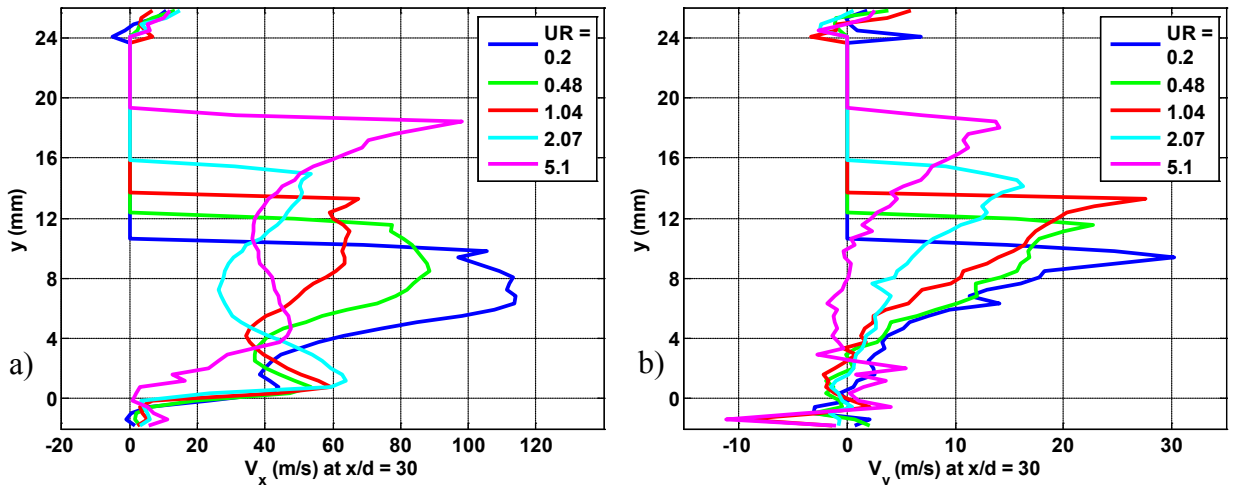

Figure 3.18 Velocity profiles for cases with $We \cong 100$, $q \cong 10$ (cases 6b, 7b, 8b, 9b, 10b), a) V_x, b) V_y.

spray core. Also as UR increases from 0.2 to 2.07, the magnitude of peak V_x decreases, as the momentum of the lower part of the crossflow decreases. However, for UR = 5.1, the jet penetrates through to the upper, higher momentum portion of the crossflow, and as a result, we observe high V_x close to the upper periphery.

The transverse velocities, V_y increase with height for all cases in figure 3.18b. As UR increases, the jet penetration increases, i.e. the spray plume reaches a larger transverse distance. Also the momentum of the upper portion of the crossflow increases, so that rate of increase in penetration decreases as UR increases. As a result, the peak V_y magnitude decreases as UR increases.

Next, the effect of We on the centerplane velocity is observed by comparing the cases with $UR \cong 1$ and $q \cong 10$ (cases 3b and 8b). Figures 3.19a and b plot the velocity distributions for these cases. The only significant difference between these cases is an increase in the droplet velocities, while the velocity distribution looks similar. This can be observed more clearly in Figures 3.19c, d,

which plot the V_x and V_y profiles, respectively, for the two cases. Both the V_x and V_y profiles shift to the right as *We* increases.

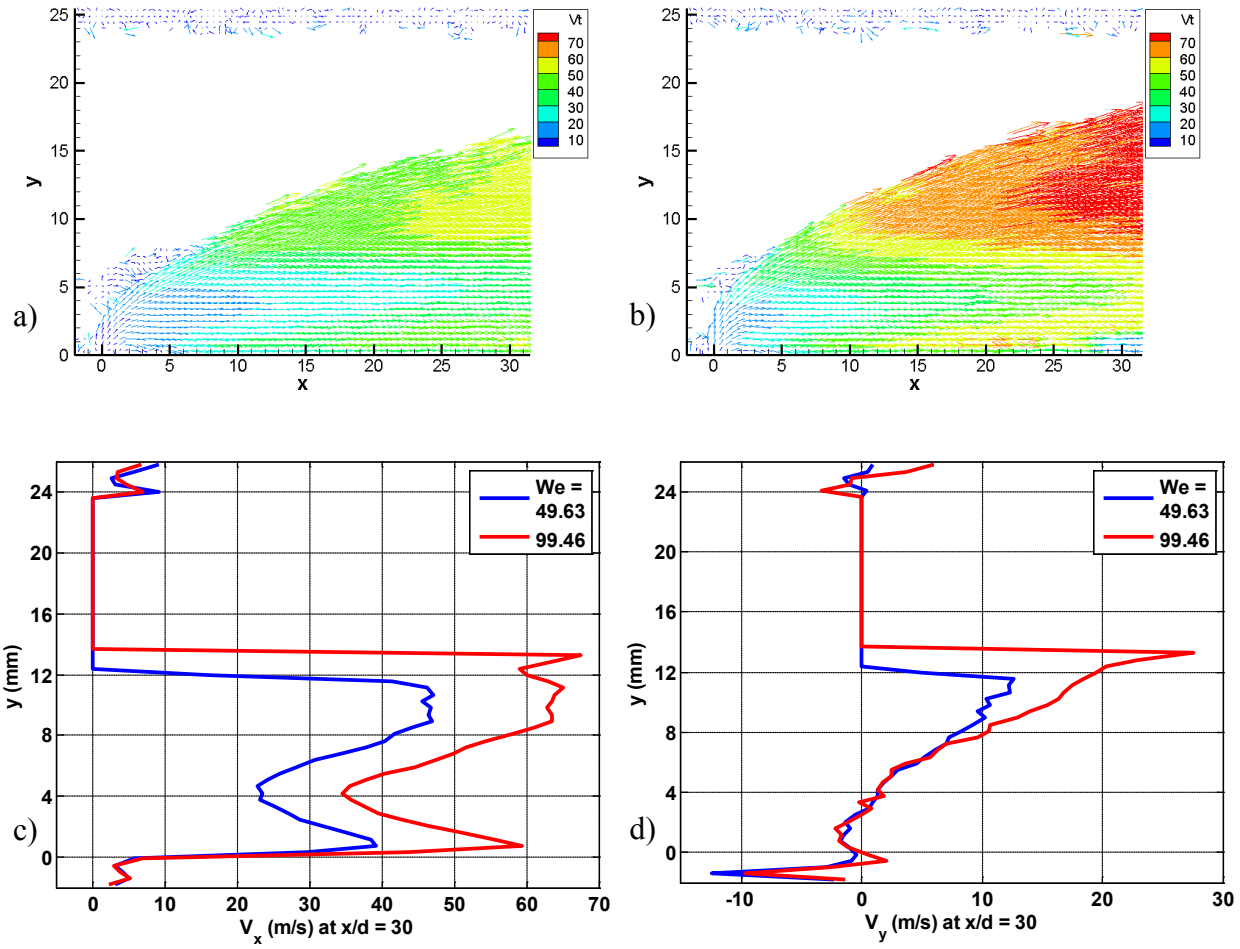

Figure 3.19 Effect of *We* on Centerplane velocity, a) Case 3b, *We* = 49.63, *UR* = 1.04, *q* = 10.14, b) Case 8b (Baseline Jet), *We* = 99.46, *UR* = 1.04, *q* = 10.07, c) V_x for cases 3b, 8b, d) V_y for cases 3b, 8b

3.5.3 Effect of *q* on Jet Centerplane Velocity

Figures 3.20a-c plot the velocity distribution for cases 8a, 8b and 8c (*We* = 99.46, *UR* = 1.04) with *q* = 4.98, 10.07 and 20.24 respectively. Figures 3.20d, e compare the V_x and V_y profiles for

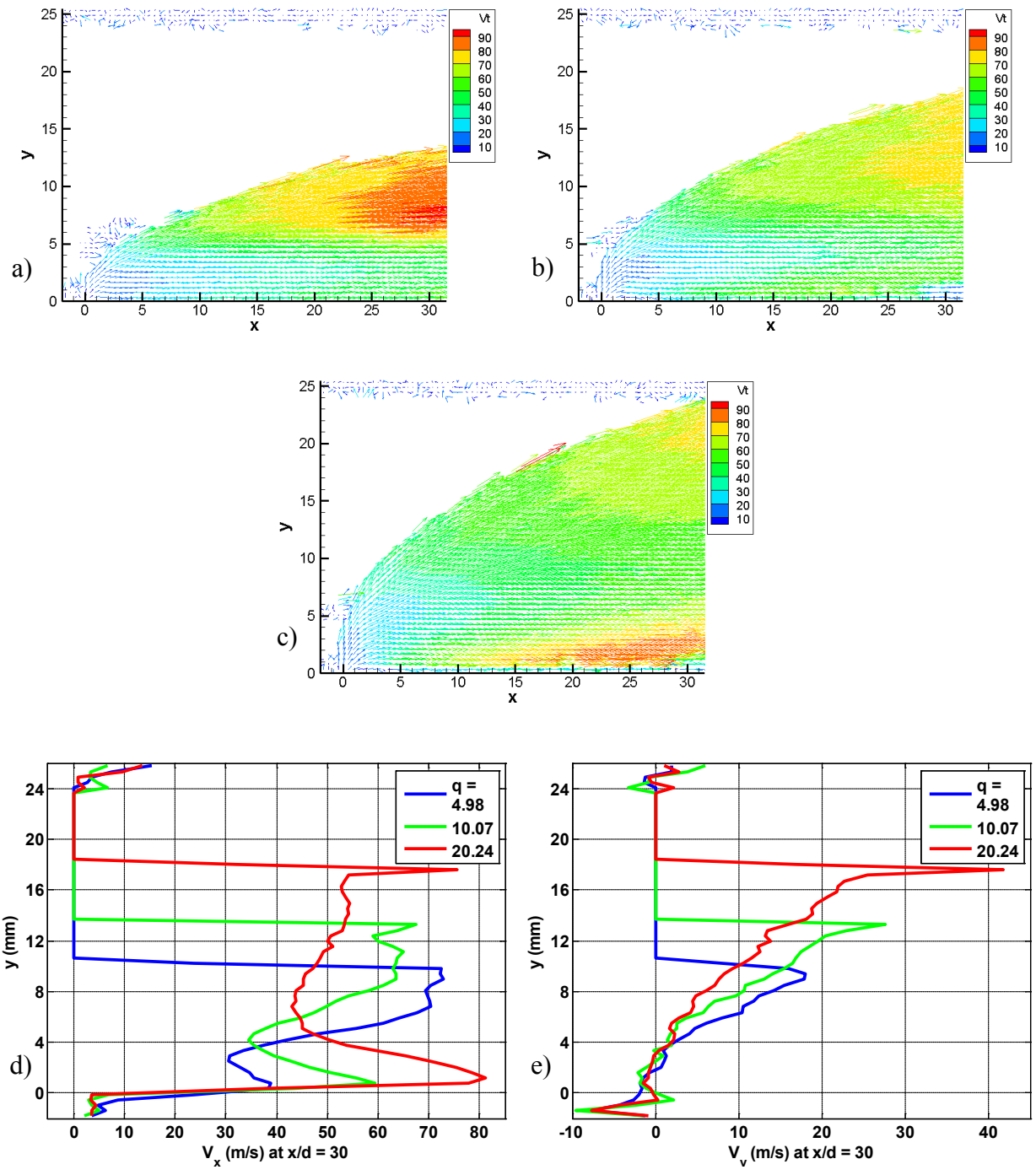

Figure 3.20 Effect of q on Centerplane velocity, a) Case 8a, We = 99.46, UR = 1.04, q = 4.98, b) Case 8b (Baseline Jet), We = 99.46, UR = 1.04, q = 10.07, c) Case 8c, We = 99.46, UR = 1.04, q = 20.24, d) V_x for cases 8a, 8b, 8c e) V_y for cases 8a, 8b, 8c

these 3 cases. In section 3.4.3, it was seen that jet penetration increases with q. As a result, as q increases, the jets retain more transverse momentum, while the amount of streamwise momentum imparted by the crossflow decreases. This results in higher V_y and lower V_x as q increases, especially in the part of the spray plume above the core.

Now, as jet penetration increases, the spray core moves away from the bottom wall. As a result, droplets lying below the core are more susceptible to acceleration by the crossflow since they are further away from the main jet body. As a result the axial velocity in the lower portion of the jet increases with q, as seen in Figure 3.20d.

3.6 Properties of the Jet Cross-Section (PDPA)

Section 3.5, studied the droplet velocities in the center plane of the jet. Next, the cross-section of the jet plume needs to be studied. Section 3.5.1 showed that the centerplane velocities obtained from PDPA measurements were very close to that obtained from PIV. This section will focus on PDPA measurements in the jet cross-section. The properties studied are the droplet axial velocity, the Sauter mean diameter (*SMD*), also known as D_{32}, and the volume flux. The volume flux has been normalized with respect to the maximum flux in the plane for comparability. PDPA measurements were conducted for only a selected few cases from the PIV study, due to the long measurement times required for PDPA.

Due to optical access restrictions, PDPA data could be acquired up to a height of y = 15 mm at the centerplane (z = 0). The measurement height available tapers off towards the left, i.e. towards the negative Z-axis. In PDPA measurements, there exists a possibility of some errors creeping up in areas with low droplet concentrations. To get rid of these errors, locations with a droplet count

of less than 5% of the maximum droplet count were located and all properties at such locations were set to zero. Also, in all cross-section measurements, the spray plumes exhibited some asymmetry about the XY plane. Similar observations have been reported in literature [26], though no conclusive reasons have been proposed yet to indicate the origin of this asymmetry.

3.6.1 Cross-Section of the Baseline Jet (case 8b)

The Baseline Jet case for the PDPA study is case 8bd, which is equivalent to the PIV baseline Jet, case 8b. The test conditions for case 8b are We = 102.86, UR = 0.99, q = 9.71. Figure 3.21 plots the Normalized volume flux, SMD and V_x for case 8bd at a cross-sectional plane located 20D downstream of the nozzle (i.e. at x = 10 mm). In Figure 3.21a, a small region near the center of the spray plume with very high volume flux is observed. This region is known as the spray core [27, 29]. The volume flux tapers off away from the spray core on all sides. The spray core usually has a high concentration of slow-moving, large droplets. This is reflected in Figures 3.21b, c where high SMD and low V_x are seen at the location of the spray core. The largest SMD values are observed in the spray core, which is surrounded by a region or relatively low SMD. Slightly higher SMD values are observed near the spray periphery. The droplet axial velocities, V_x exhibit a minimum at the spray core. V_x increases away from the spray core in all directions.

Additional PDPA cross-sectional measurements were conducted at a streamwise location 50d downstream (x = 25 mm) to observe the progressive change of the jet as it moves downstream. Figure 3.22 plots the properties of the baseline jet at this location. Figure 3.22a shows that at the spray plume has expanded in the transverse as well as the lateral direction while moving from x/d = 20 to x/d = 50. The relative shift in height of the spray core is comparable to the relative increase in the penetration of the jet, so that the plume essentially expands as the jet moves downs-

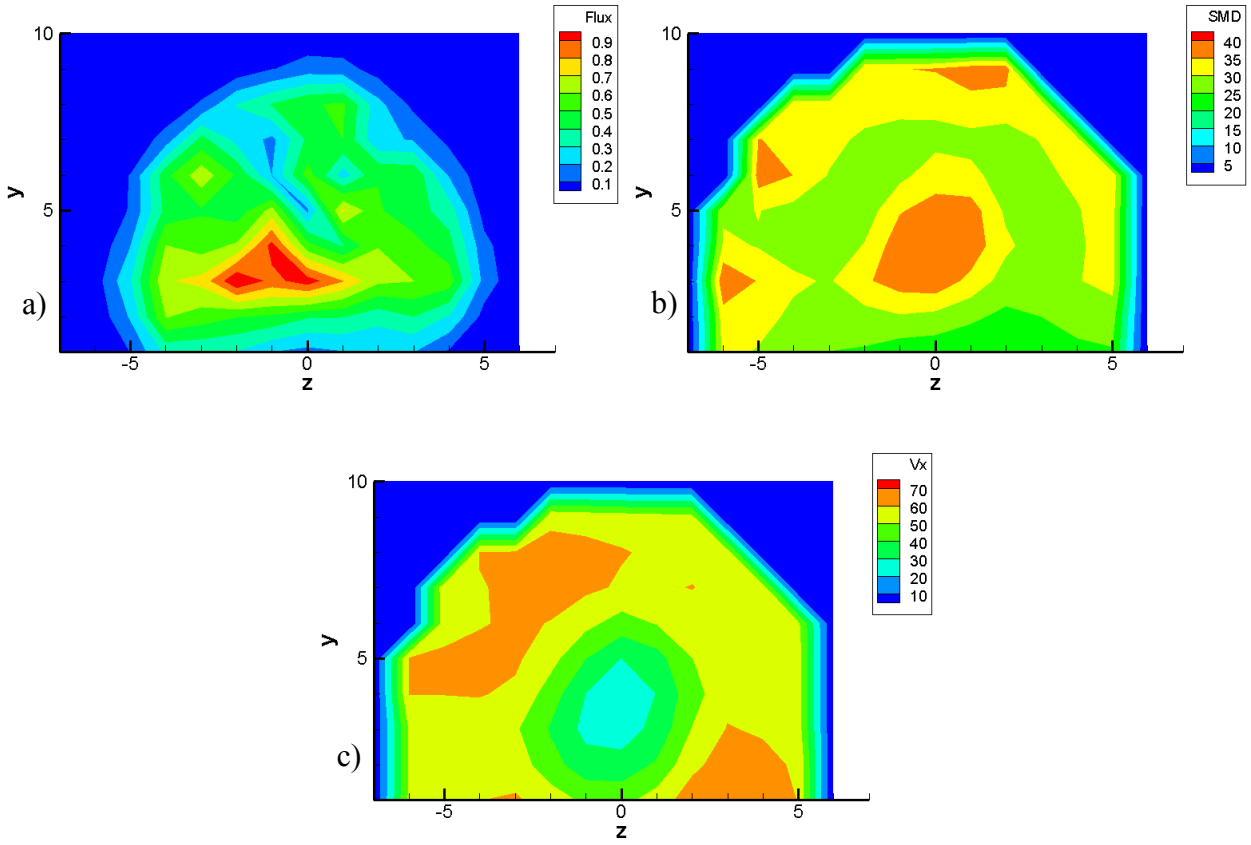

Figure 3.21 PDPA for Baseline Jet, case 8bd, at $x/d = 20$ a) Normalized Volume Flux, b) *SMD*, c) V_x

tream. Figure 3.22b shows that higher *SMD* values were observed throughout the plume, as compared to the $x/d = 20$ location. This occurs as by $x/d = 50$, some of the smaller droplets have evaporated off, causing the SMD to increase. At $x/d = 50$, the droplet axial velocities are higher, though the velocity trend is similar. The increase in the magnitude of V_x occurs due to additional momentum exchange with the crossflow between the two locations.

3.6.2 Effect of *UR* on the Jet Cross-Section

To study the effect of *UR* on the cross-sectional properties cases 6bd, 8bd and 10bd with *UR* val-

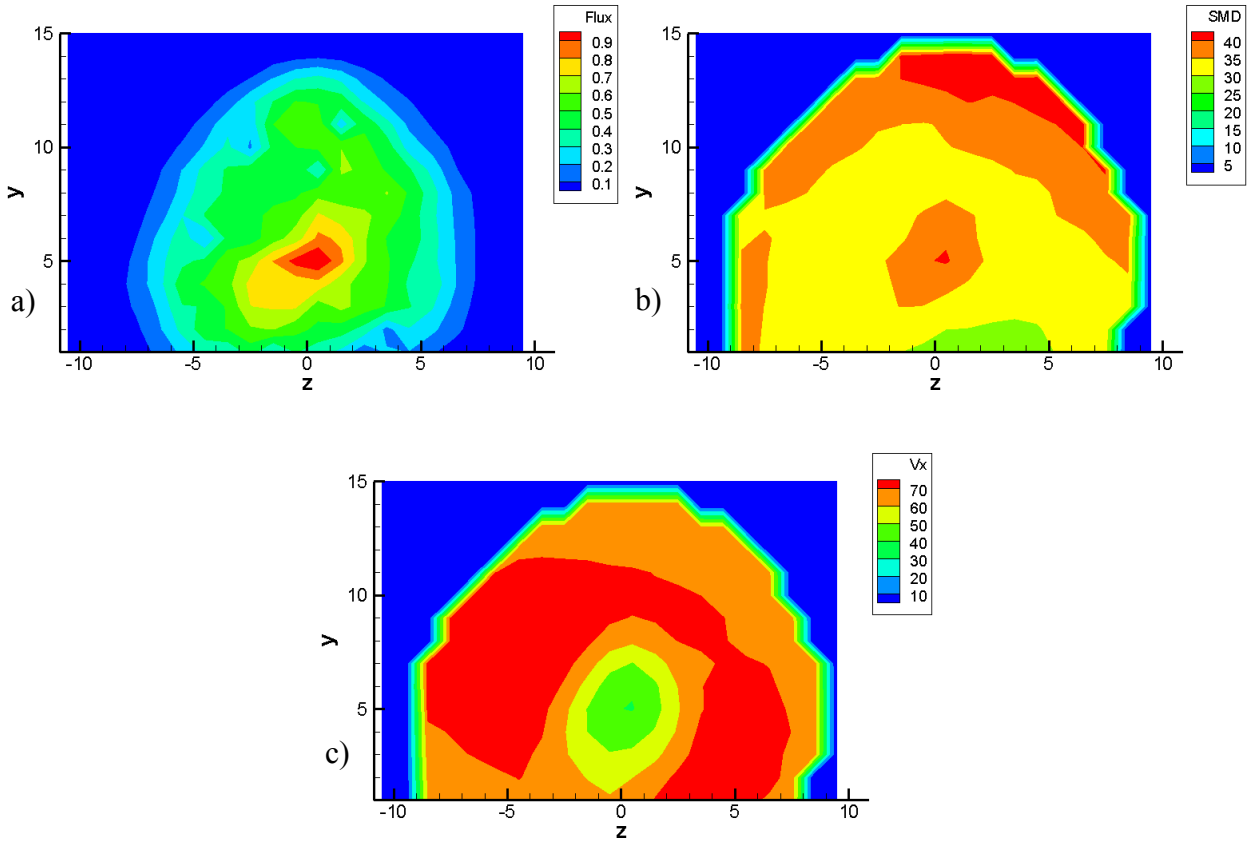

Figure 3.22 PDPA for Baseline Jet, case 8bd, at $x/d = 50$ a) Normalized Volume Flux, b) *SMD*, c) V_x

ues of 0.2, 0.99 and 5.09, respectively, with $We \cong 100$ and $q \cong 10$ are considered. Figures 3.23, 3.24 and 3.25 plot the Normalized Volume Flux, *SMD* and V_x, respectively, for these three cases.

From Figure 3.3 it was seen that an increase in *UR* results in an increase in jet penetration. Similar effect can be observed here. The increase in penetration is also reflected in an increase in the height of the spray core. The spray core for case 10bd is shifted towards the negative *Z*-axis. The reason for this shift is not known.

It is known that as UR increases, the momentum of the lower portion of the crossflow decreases. This means that for small UR, the crossflow near the bottom wall will have higher momentum, and thus can be expected to impart higher momentum to the jet and induce higher atomization.

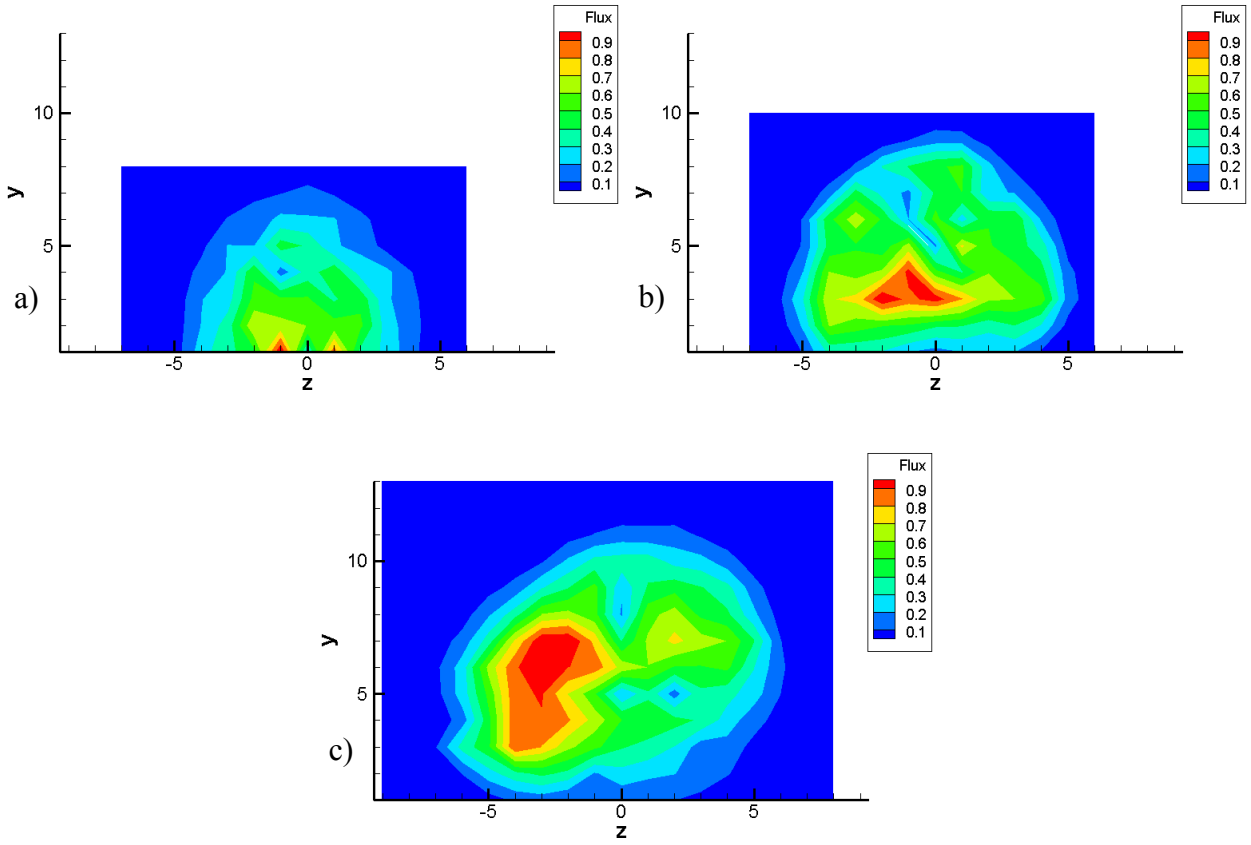

Figure 3.23 Effect of *UR* on Normalized Volume Flux, a) case 6bd, *We* = 100.88, *UR* = 0.2, *q* = 9.9, b) case 8bd (baseline jet), *We* = 102.86, *UR* = 0.99, *q* = 9.71, c) Case 10bd, *We* = 101.93, *UR* = 5.09, *q* = 9.8

The SMD distributions in Figure 3.24, indicate that this is indeed the case, as the SMD values throughout the plume of case 6bd (UR = 0.2) are very small compared those for case 8bd (*UR* = 0.99). The *SMD* distribution of case 6bd is still similar to the 8bd, which has the typical *SMD* distribution for a jet in crossflow. However the *SMD* distribution for case 10bd is different, with higher *SMD* values observed towards the left spray periphery. Comparing Figures 3.23c and 3.24c, it can be seen that though high *SMD* values occur in the spray core, which is itself to the left of the centerline, the highest *SMD* values occur to the left of the core, in a region which has a very low volume flux. This can be attributed to very low droplet count in the region, leading to a

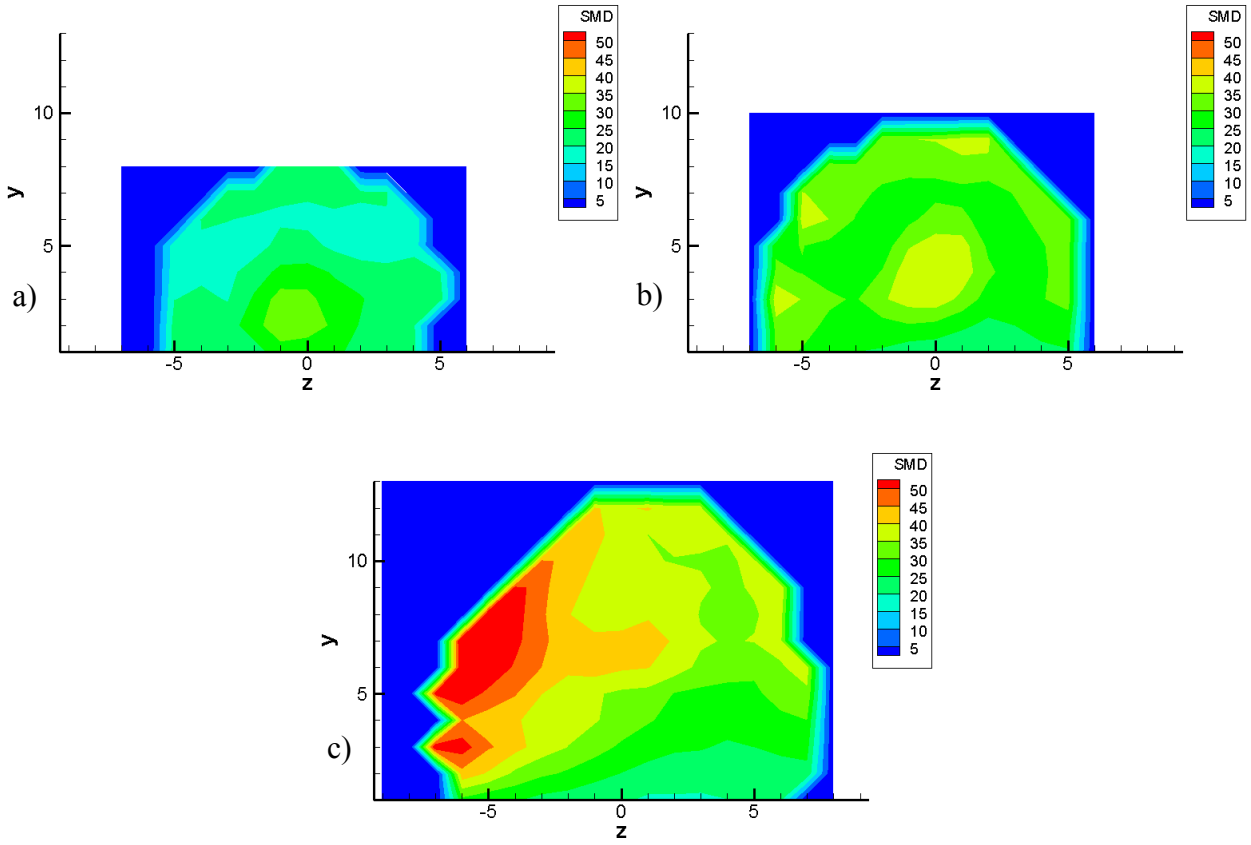

Figure 3.24 Effect of *UR* on SMD, a) case 6bd, *We* = 100.88, *UR* = 0.2, *q* = 9.9, b) case 8bd (baseline jet), *We* = 102.86, *UR* = 0.99, *q* = 9.71, c) Case 10bd, *We* = 101.93, *UR* = 5.09, *q* = 9.8

skewed *SMD* value. However, *SMD* values in the bulk of the plume are very close, leading to an *SMD* distribution that is more homogeneous as compared to a typical jet.

It was proposed above that we can expect higher momentum exchange for the case with low *UR*. Figure 3.25 shows that this is indeed true, as case 6bd exhibits the highest axial velocities. The V_x distributions for both cases 6bd and 10bd are similar to that of the typical velocity distribution seen for the baseline jet, case 8bd. Additionally, case 10bd exhibits low velocities to the left of the centerline, which supports the observation of larger droplets and higher volume flux in that region.

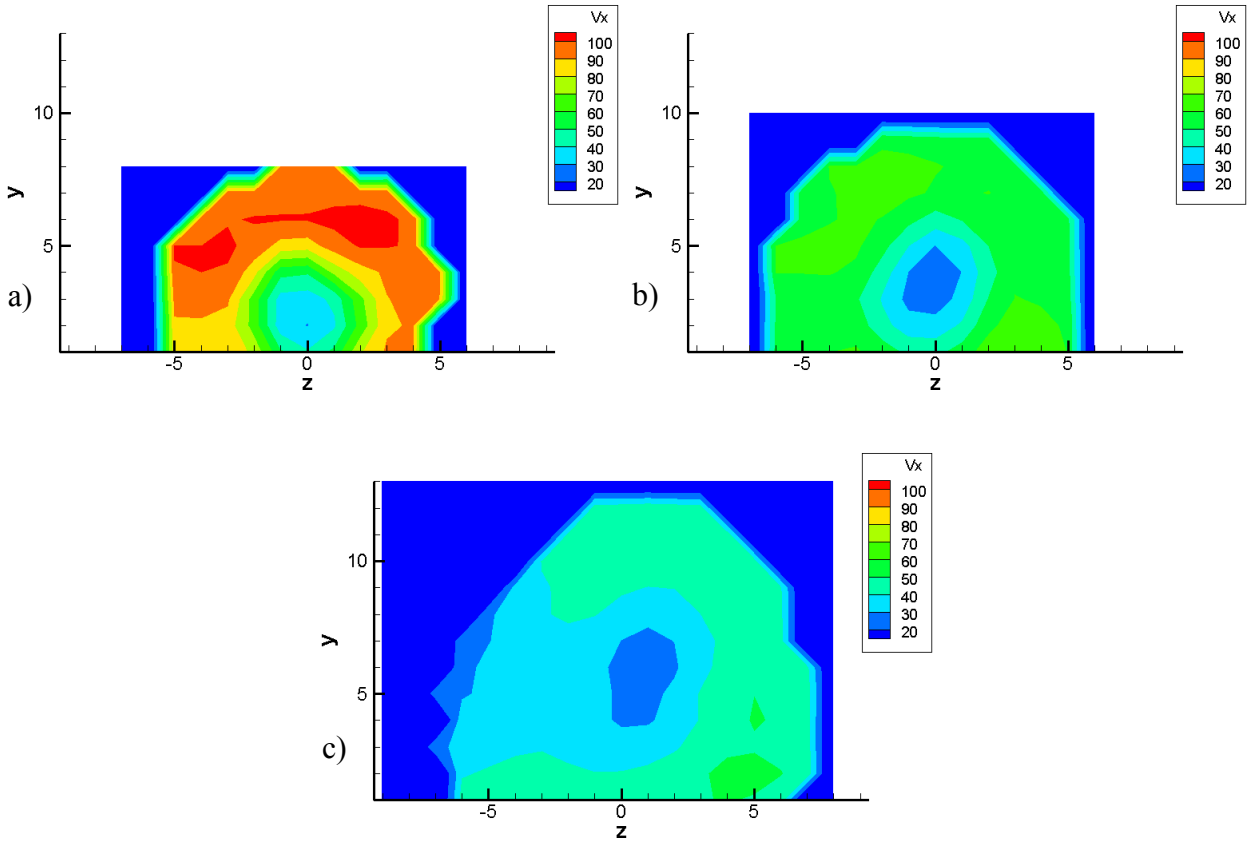

Figure 3.25 Effect of *UR* on V_x, a) case 6bd, *We* = 100.88, *UR* = 0.2, *q* = 9.9, b) case 8bd (base-line jet), *We* = 102.86, *UR* = 0.99, *q* = 9.71, c) Case 10bd, *We* = 101.93, *UR* = 5.09, *q* = 9.8

3.6.3 Effect of *q* on the Jet Cross-Section

For a typical jet in crossflow, the most significant effect of an increase in *q* is an increase in penetration. Also, at high *q*, location of high SMD shifts towards the upper spray periphery, and the spray coverage area increases [29].

To study the effect of *q*, cases 8bd and 8cd with *q* of 9.9 and 19.75 respectively, (*We* ≅ 100 and *UR* ≅ 1) are compared. Figures 3.26, 3.27 and 3.28 plot the Normalized Volume Flux, SMD and V_x, respectively for cases 8bd and 8cd. Figure 3.26 shows that the core moves up within the

spray plume, so that it is located closer to the upper edge of the periphery with increasing q. Additionally, the location of high *SMD* values also moves up along with the spray core, as seen in Figure 3.27.

An increase in q, while keeping *We* constant, signifies an increase in jet momentum while the crossflow momentum is held constant. As a result the jet penetrates higher, causing the low V_x core to be located at a higher transverse location, as seen in Figure 3.28. Additionally, the spray plume size increases. Now since the core is located higher, the droplets below the core are now

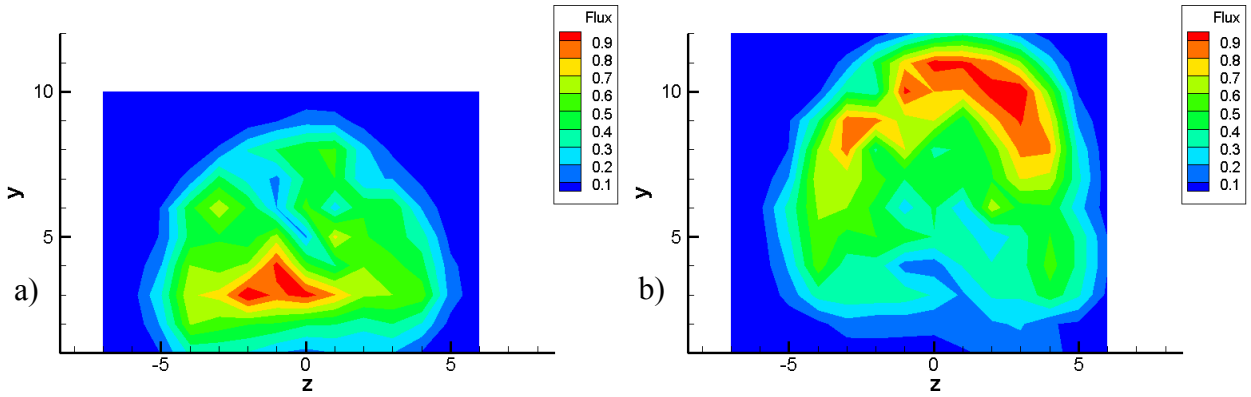

Figure 3.26 Effect of q on Normalized Volume Flux, a) case 8bd (baseline jet), *We* = 102.86, *UR* = 0.99, q = 9.71, b) case 8cd, *We* = 99.96, *UR* = 0.98, q = 20.04

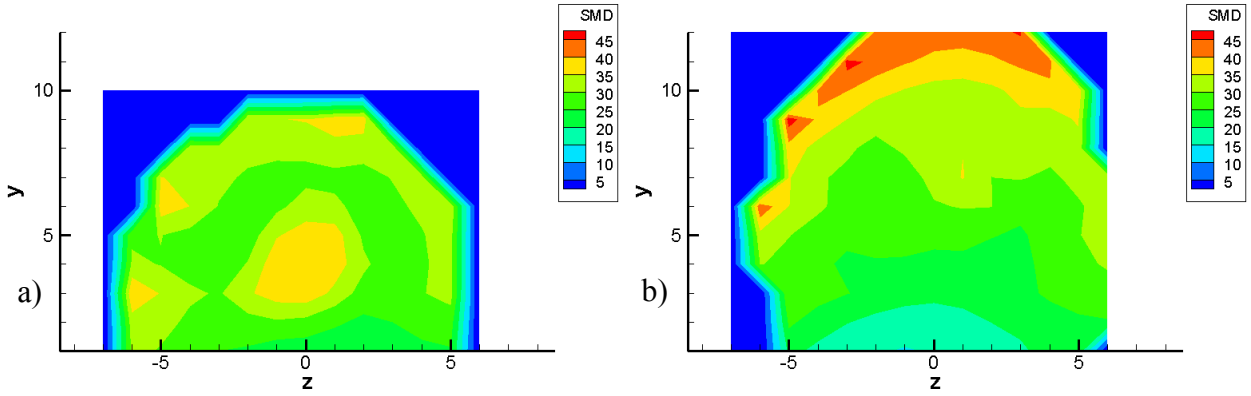

Figure 3.27 Effect of q on *SMD*, a) case 8bd (baseline jet), *We* = 102.86, *UR* = 0.99, q = 9.71, b) case 8cd, *We* = 99.96, *UR* = 0.98, q = 20.04

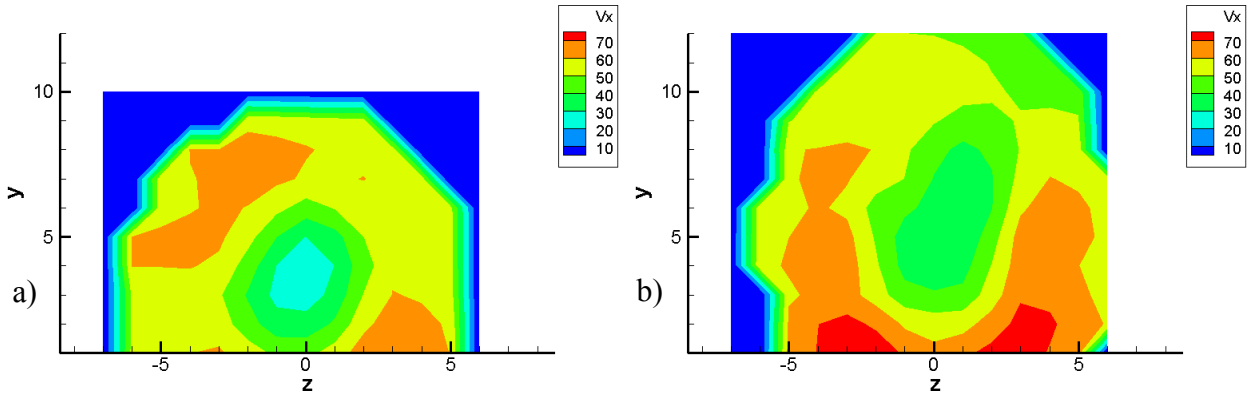

Figure 3.28 Effect of q on V_x, a) case 8bd (baseline jet), We = 102.86, UR = 0.99, q = 9.71, b) case 8cd, We = 99.96, UR = 0.98, q = 20.04

further from the core so that there is greater momentum exchange with crossflow leading to higher V_x being observed to the sides and below the crossflow.

Two other cases, 6bd and 6cd were also compared, to further support the conclusions drawn above. Cases 6bd and 6cd have $We \cong 100$ and $UR \cong 0.2$, with q of 9.9 and 19.75 respectively. Figures 3.29, 3.30 and 3.31 plot the Normalized Volume Flux, SMD and V_x, respectively for cases 6bd and 6cd. An increase in the height of the spray core is observed here as well, though not as much as case 8cd. The spray core for case 6cd is still near the center of the jet plume. The

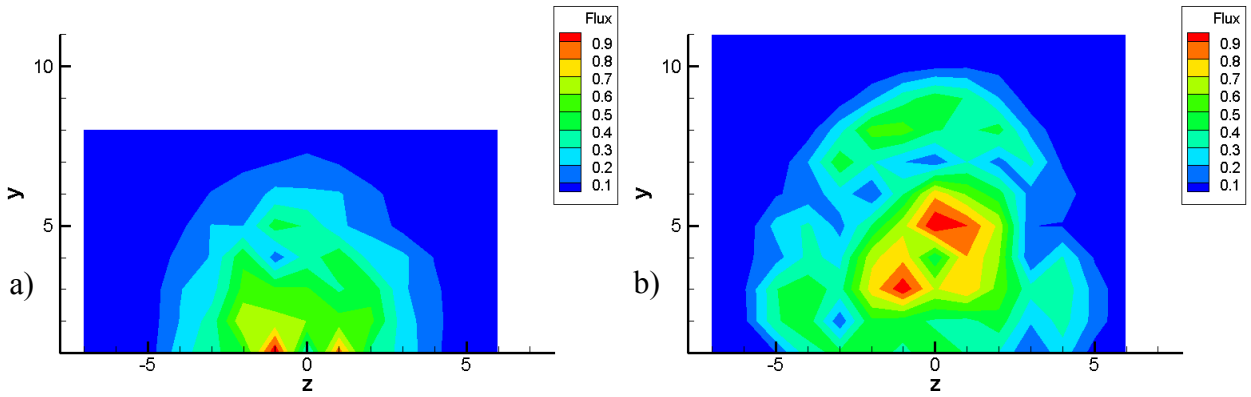

Figure 3.29 Effect of q on Normalized Volume Flux, a) case 6bd (baseline jet), We = 100.88, UR = 0.2, q = 9.9, b) case 6cd, We = 101.78, UR = 0.2, q = 19.75

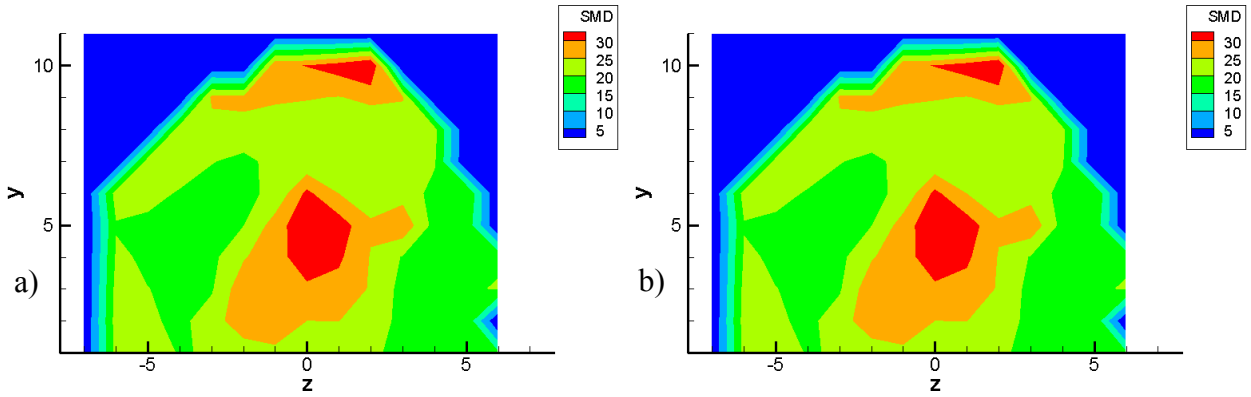

Figure 3.30 Effect of q on SMD, a) case 6bd (baseline jet), We = 100.88, UR = 0.2, q = 9.9, b) case 6cd, We = 101.78, UR = 0.2, q = 19.75

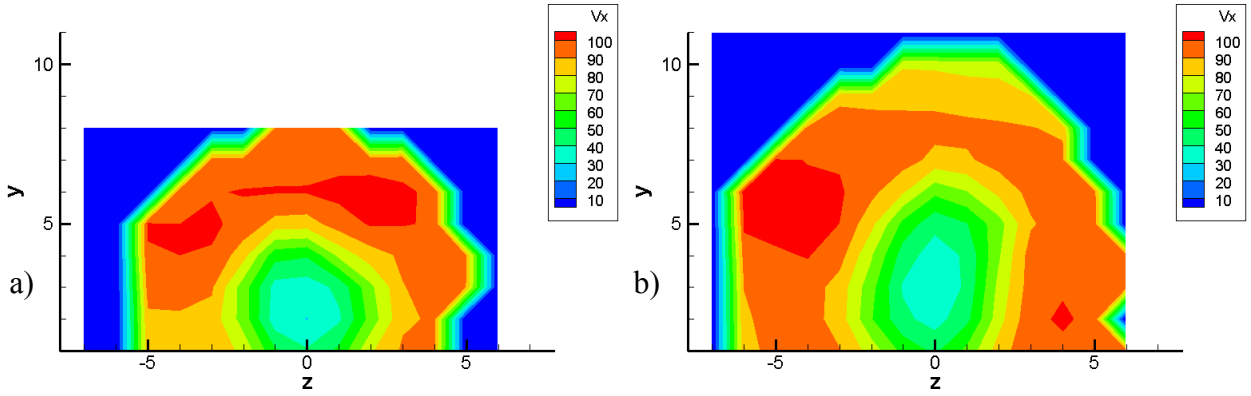

Figure 3.31 Effect of q on V_x, a) case 6bd (baseline jet), We = 100.88, UR = 0.2, q = 9.9, b) case 6cd, We = 101.78, UR = 0.2, q = 19.75

height of high *SMD* values also increases with q, though there is no significant increase in the magnitude of the peak *SMD*. Additionally, a small region of high *SMD* is observed near the upper periphery for case 6cd.

The V_x distribution for both cases 6bd and 6cd is similar, as are the magnitudes of V_x. High V_x near the base of the periphery seen for case 8cd is not seen here, the reason for which is the lower penetration due to the small *UR* for case 6cd. Higher droplet velocities are observed to the sides of the spray core for case 6cd.

3.7 Summary of Jets in Shear-Laden Crossflow

A crossflow with a steady-state, quasi-linear velocity profile due to the presence of the shear layer between the two component airstreams has been studied. The velocity ratio parameter, *UR* was seen to have a significant effect on the velocity gradient and the flow turbulence. *UR* also affected jet behavior. For high *UR* (> 1), jet penetration increased, and the *SMD* distribution in the cross section became more uniform. For low *UR* (< 1), jet penetration reduced significantly. Atomization was improved and the liquid droplets moved with higher velocity.

Chapter 4 Liquid Jets Injected into Swirling Crossflow

4.1 Approach to Measurements and Test Conditions

As seen in Chapter 3, it is important to completely characterize the crossflow before the behavior of jets injected into such a flow is studied. The procedure for obtaining measurements of the crossflow is considered here.

The most important parameter for this study is the aerodynamic Weber number, *We*. However, *We* is defined based upon the total crossflow velocity which cannot be measured directly. Only the axial component of the crossflow velocity, U_x, can be estimated, based on the air mass flow rate. However, crossflow velocity will also have non-trivial components in the radial and the tangential direction, which are unknown.

4.1.1 Test Conditions

A way of determining these unknown components is to conduct LDV tests on the crossflow. The Artium PDI-200 system was used for the LDV tests. Measurements were carried out in a single cross-sectional plane, 2.54 cm (1 inch) downstream of the location of jet injection (x = 2.54 cm). The test conditions for the LDV study are listed in Table 4.1. Detailed analysis was carried out to recreate the velocity components as described in Table 4.1.

Once the crossflow was analyzed, PIV studies were conducted on the jet. Multi-plane PIV investigations were carried out to recreate the 3-D jet. Measurements were conducted in both stream-

wise (x = constant) and cross-sectional (z = constant) planes. The test conditions have been listed in Table 4.2. The test conditions for streamwise studies were designed to replicate the test conditions for the cross sectional studies. Hence they are named similarly with the last letter in the case name indicating the measurement planes. Thus, for case J3, J3c represents measurement in cross-sectional planes and J3s represents measurement in streamwise planes.

Table 4.1 Test conditions for swirling crossflow

Case no	Swirler	*We*	m_{cf}	U_x	U_θ	U	ψ
			(kg/s)	(m/s)	(m/s)	(m/s)	(deg)
C1	30	32.55	0.226	54.28	31.35	62.69	30
C2 (base)	45	33.91	0.222	50.67	38.95	63.91	37.5
C3	60	25.98	0.175	40.37	39.13	56.22	44.1
C4	60	49.35	0.24	55.41	54.12	77.46	44.3

Table 4.2 Test conditions for jets injected into swirling crossflow

Case No	Swirler	*We*	*q*	m_{cf}	U_x	U_θ	U	m_j	V	Measurement
				(kg/s)	(m/s)	(m/s)	(m/s)	(kg/min)	(m/s)	Plane
J1c	30	106.16	9.42	0.401	99.59	57.5	114.99	0.141	12.02	cross-sectional
J2c	45	42.27	12.05	0.245	57.14	43.92	72.07	0.101	8.58	cross-sectional
J3c (base)	45	83.72	12.02	0.345	80.42	61.82	101.41	0.142	12.06	cross-sectional
J4c	45	83.72	24.01	0.345	80.42	61.82	101.43	0.2	17.05	cross-sectional
J5c	60	51.66	19.6	0.243	57.38	56.06	80.22	0.142	12.1	cross-sectional
J6c	30	106.16	18.94	0.401	99.59	57.5	114.99	0.2	17.05	cross-sectional
J7c	60	51.56	39.16	0.243	57.28	55.95	80.07	0.201	17.09	cross-sectional
J1s	30	106.35	9.4	0.401	99.77	57.6	115.21	0.141	12.02	streamwise
J2s	45	42.76	11.91	0.245	57.8	44.43	72.9	0.101	8.58	streamwise
J3s (base)	45	84.69	11.96	0.345	81.35	62.53	102.61	0.142	12.1	streamwise
J4s	45	84.69	23.84	0.345	81.35	62.53	102.61	0.2	17.09	streamwise
J5s	60	52.08	19.44	0.245	57.31	55.99	80.12	0.142	12.1	streamwise

The baseline cases for the crossflow and the jet are cases C2 and J3. The Weber number, *We*, and the momentum flux ratio, q, described in the test conditions were calculated based on total crossflow velocity, which was obtained from LDV results as explained in the results section.

4.1.2 Note on Polar Coordinates

The generic flow issuing out of a swirler is axisymmetric in nature. The same holds true for the axial swirlers used in the current experiments. There will be periodic regions of velocity deficit due to the presence of the vanes, however, these deficits are expected to be small and should dissipate with streamwise distance. Then, it will be more insightful to analyze the flow in polar coordinates. In fact, it is beneficial to consider the flow field in a cylindrical domain, which incorporates the cross-section in polar coordinates, and the streamwise (X) direction. However all measurements are conducted in cartesian planes. It thus becomes necessary to transform from a 3D cartesian measurement domain to a cylindrical domain. As noted, the polar coordinates occur in a cross-sectional (x = constant) plane, thus the transformation also occurs in the x = constant plane. The transformation is carried out in two steps, as explained below.

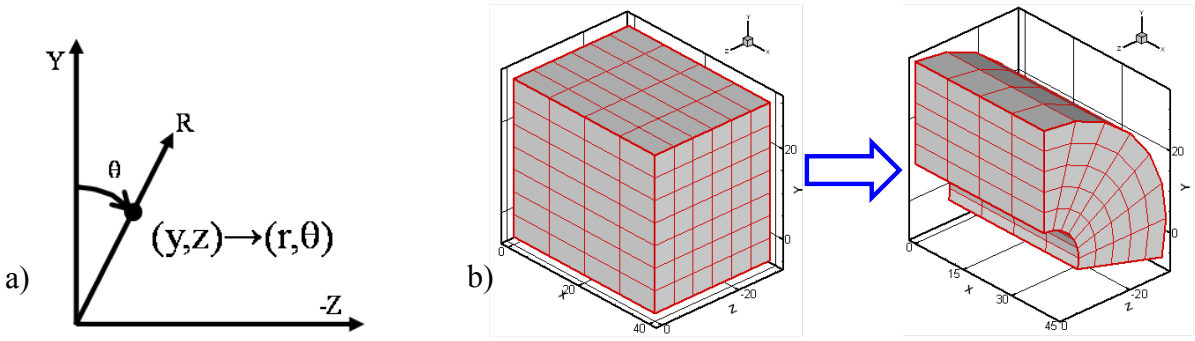

Figure 4.1 Transformation from cartesian to polar domain, a) Polar coordinate frame, b) Conversion to polar domain

In the first step, the cartesian coordinates in the x = constant plane (y, z) are transformed into polar coordinates (r, θ). This process is shown in Figure 4.1a. Since the jet nozzle is located at the positive Y-axis, the jet will issue out vertically upwards and then spin towards the negative Z-axis. Thus the area of interest is the top right quadrant (as viewed from downstream) bounded by

the $+Y$ and $-Z$ axes. Then the polar coordinate system was chosen such that $\theta = 0°$ occurs on the positive Y-axis and $\theta = 90°$ occurs at the negative Z-axis. In this step, polar coordinates are assigned to each measurement location in the plane. It is pertinent here to note that even though the grid points in the plane have polar coordinates, they are still organized in a cartesian manner, i.e. equal grid spacing along each of Y- and Z- directions.

In order to obtain good analysis, it is necessary to order the locations containing data in a polar manner. For example, in order to track the circumferential displacement of a particle in the crossflow, it is important to have data along θ = constant lines. Thus data needs to be reorganized in a polar domain. In step 2, a polar grid was defined such that it spans the area of interest in the cartesian grid. Properties at the new grid point locations were obtained by interpolating between the original grid points. Assuming that the spacing between grid points in the R and Θ directions is λ_r and λ_θ respectively, the interpolation is carried over an area given by ($r \pm \lambda_r/2$, $\theta \pm \lambda_\theta/2$). This process is shown in Figure 4.1b.

The conversion from cartesian to polar domain occurs in a cross-sectional (x = constant) plane. Then if the original data was contained in a cross-sectional plane, the conversion can be carried out without any significant loss of information. However, if the original measurements were carried out in streamwise planes, then a cross-sectional slice of the 3-D domain would contain information only along discrete lines. Then there is a good chance that the missing information would lead to erroneous conclusions. Hence, the domain conversion is conducted only for cross-sectional measurements.

4.2 Swirling Crossflow: Results and Discussion

In a manner similar to the study on the shear-laden crossflow, it is necessary to characterize the swirling crossflow, in order to judge its effect on the jets injected into it. LDV measurements were conducted on the crossflow for the different swirlers. 4 cases were studied, as given in Table 4.1. Case C2, for the 45° swirler, was considered as the base crossflow case. The crossflow was seeded with olive oil droplets to enable measurement.

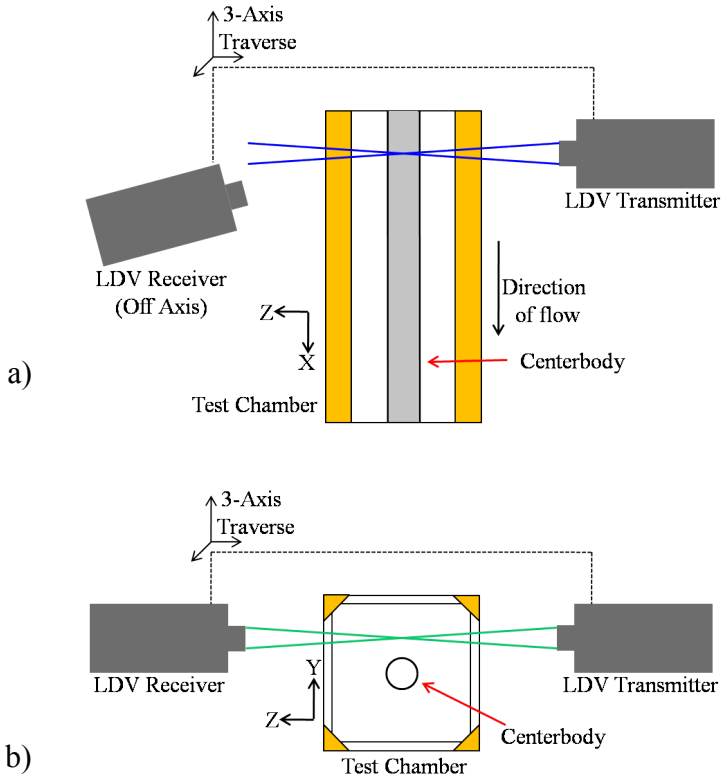

Figure 4.2 LDV Setup, a) Top view, b) View from downstream

4.2.1 Velocity Distribution for the Baseline Crossflow (Case C2): Original Measurements

Figure 4.2 shows the layout of the LDV measurement setup. The receiver was positioned at an angle of 15° off-axis position. Measurements were conducted in a cross-sectional plane located

25.4 mm (1 inch) downstream of the jet nozzle (i.e. x = 25.4 mm). Figure 4.3 shows the grid of measurement locations for the crossflow studies, where measurement locations are designated by the intersections of the horizontal and vertical grid lines. The location of the centerbody is indicated by the black circle in Figure 4.3. Now, from Figure 4.2b, it can be seen that the laser light will be blocked by the centerbody over the Y-range of $-r_{cb} \leq y \leq r_{cb}$. This blockage is the reason that no measurement points exist for -10.5 mm > y > 10.5 mm.

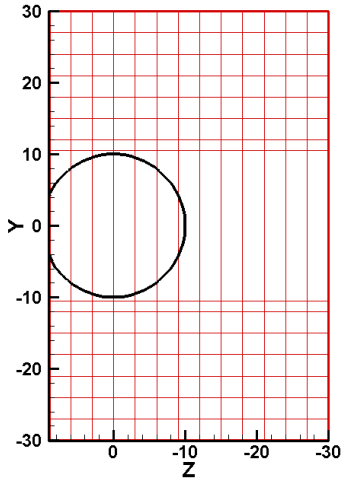

Figure 4.3 LDV measurement grid

Figure 4.4 shows the velocity results for the baseline crossflow, Case C2, which featured the 45° swirler with We = 33.91. Figure 4.4a, shows that the axial component of the crossflow velocity, U_x, is high near the centerbody, but decreases with increasing distance from the centerbody. On the other hand, U_y, which is the vertical component of crossflow velocity, does not change significantly with distance from the centerbody. The variation in U_y is consistent with a clockwise rotation, which generates negative U_y in the right half plane ($-Z$-axis). The magnitude of U_y is nearly zero towards both arms of the Y-axis, and increases as near the $-Z$-axis. This shows the axisymmetric nature of the crossflow.

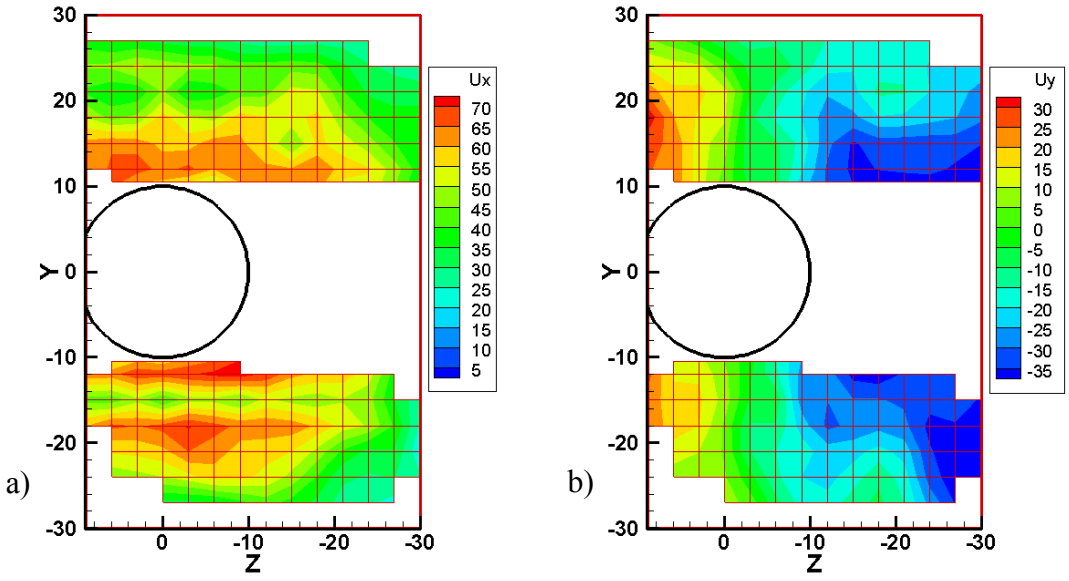

Figure 4.4 LDV results for case C2, 45°, *We* = 33.91, a) U_x, b) U_y

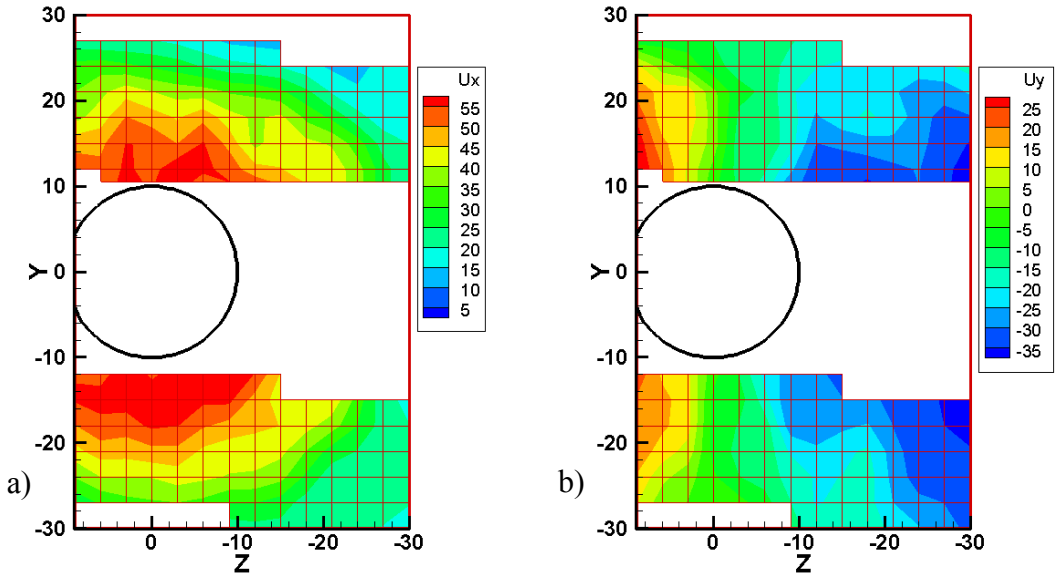

Figure 4.5 LDV results for case C3, 60°, *We* = 25.98, a) U_x, b) U_y

In order to confirm the above conclusion, the measured velocities from another test case, case C3, which features the 60° swirler with *We* = 25.98, are considered. The velocity components for case C3 are shown in Figure 4.5. Case C3 clearly exhibits the axisymmetric velocity distribution.

U_x clearly decreases with radial distance away from the centerbody. Also U_y changes along with circumferential location.

In the next couple of sections, the analysis undertaken to enhance the understanding of the crossflow is described. The base crossflow case, case C2 will serve as an example to demonstrate the analysis.

4.2.2 Transformation to Polar Velocity Components

The crossflow was observed the axisymmetric in section 4.2.1. In order to analyze the flow completely, it is necessary to conduct the analysis in polar coordinates. A polar grid was created and U_x and U_y components were mapped to the new grid locations by interpolation, as described in section 4.1.2. Figure 4.6 shows the new polar grid along with contours of U_y for case C2. From figure 4.6, it can be seen that the values of U_y are known along two distinct circumferential zones, $-30° \leq \theta \leq 60°$ and $120° \leq \theta \leq 210°$.

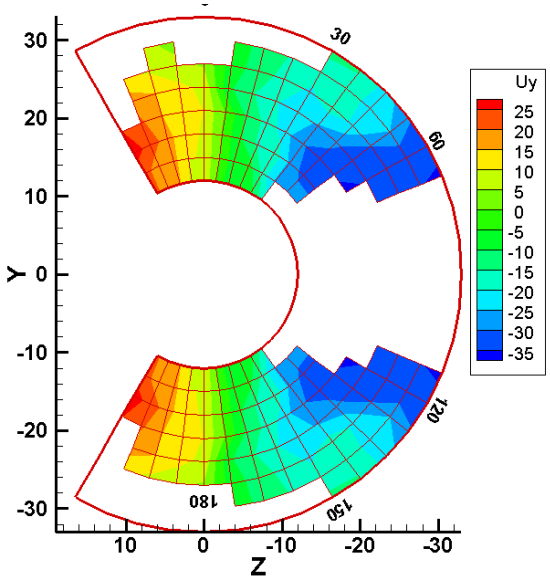

Figure 4.6 U_y contours for case C2 (45°, We = 33.91) mapped to polar grid

Now since the crossflow is axisymmetric, it follows that the magnitude of the velocity vector and it's orientation with respect to a radial line should be independent of the circumferential position. It follows that the magnitude of the *y*-component of the velocity at a location (r, θ) will be equal to the magnitude of the *z*-component of the velocity at a location of (r, $\theta \pm 90°$). The sign of the U_z component at these locations depends on the sense of rotation of the flow. Then, based on the circumferential positions where U_y is known, U_z for $60° \leq \theta \leq 150°$ and $30° \leq \theta \leq 120°$, respectively can be calculated.

Thus the only circumferential zones where both U_y and U_z are known are $30° \leq \theta \leq 60°$ and $120° \leq \theta \leq 150°$. Additionally, closer inspection reveals that both these zones are equivalent. Consider the region $30° \leq \theta \leq 60°$. U_y for this region is obtained from the U_y results at $30° \leq \theta \leq 60°$, while U_z is obtained from U_y results from $120° \leq \theta \leq 150°$. On the other hand, for the region $120° \leq \theta \leq 150°$, U_y and U_z are obtained from U_y results from $120° \leq \theta \leq 150°$ and $30° \leq \theta \leq 60°$ respectively. Thus when we calculate the in-plane velocities in these two regions, they will be essentially equivalent. Hence we consider only one of the two zones, $30° \leq \theta \leq 60°$. The three velocity components for this region for case C2 are shown in Figure 4.7.

$$U_r = U_y \cos\theta - U_z \sin\theta \tag{4.1}$$

$$U_\theta = -U_y \sin\theta - U_z \cos\theta \tag{4.2}$$

Next the polar velocity components for each grid point in the zone $30° \leq \theta \leq 60°$ need to be determined. The transformation to polar velocity components was obtained by using trigonometric relations. These relations were derived from the geometry of the measurement plane (Figure 4.8),

and have been given in equations 4.1 and 4.2. Figure 4.9 plots the radial (U_r) and the tangential (U_θ) components of the crossflow velocity for case C2.

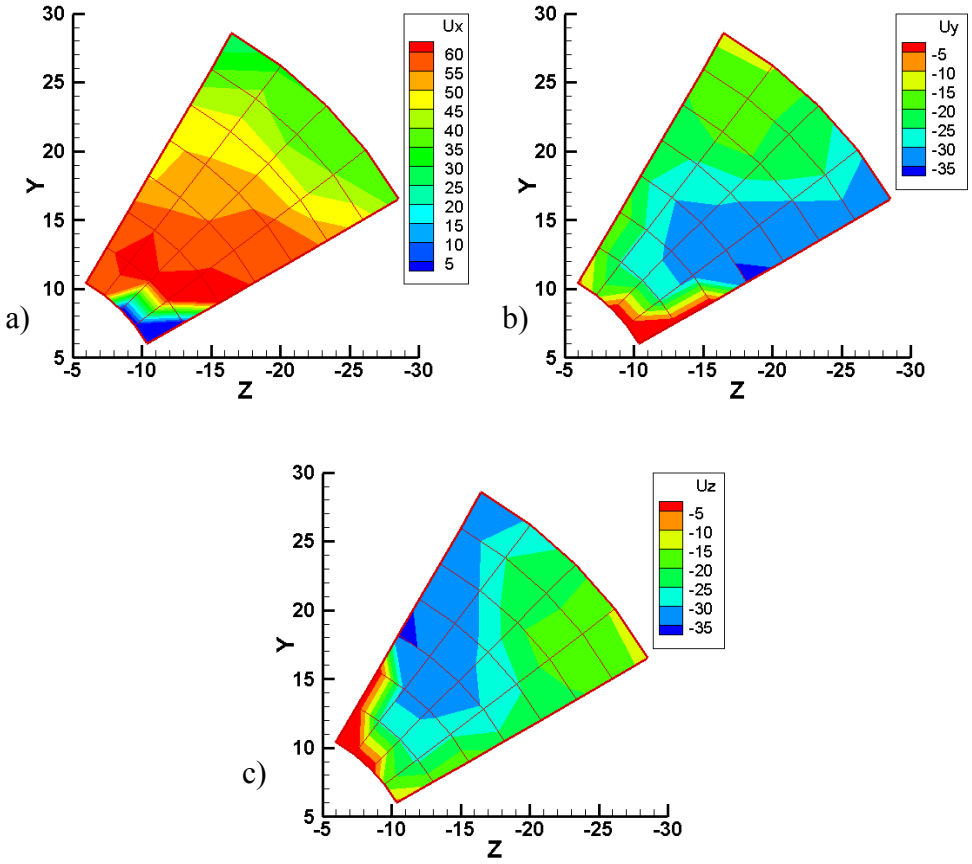

Figure 4.7 Cartesian velocity component contours for case C2 (45°, *We* = 33.91) for the circumferential region 30° ≤ θ ≤ 60°, a) U_x, b) U_y, c) U_z

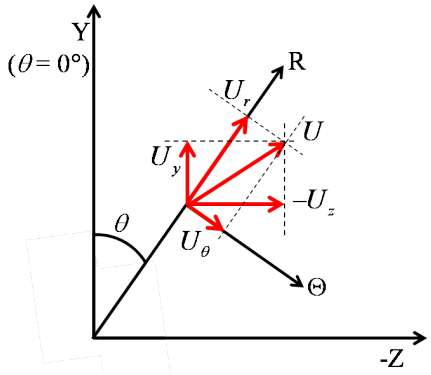

Figure 4.8 Geometry of the measurement plane used to obtain polar velocity components

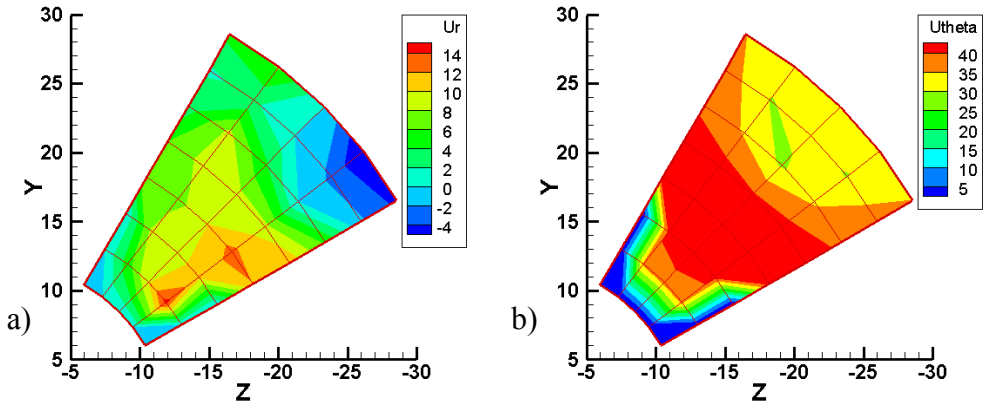

Figure 4.9 Polar velocity component contours for crossflow case C2 (45°, *We* = 33.91), for the circumferential region 30° ≤ θ ≤ 60°, a) U_r, b) U_θ

Figure 4.9 shows that there was no significant variation in both U_r and U_θ with θ. Then the variation of these components with θ was obtained by taking a circumferential average. The variation of U_x with θ was also obtained in similar fashion. The total crossflow velocity, U was then obtained as a vector sum of these three components.

The total velocity and the cylindrical components for case C2 are plotted in Figure 4.10. The streamwise velocity component, U_x, is seen to decrease with increasing radial distance, r, away from the centerbody. The radial velocity component, U_r was nearly constant for low r, but then started decreasing at higher r. The magnitude of U_r was nearly an order of magnitude smaller than U_x. The tangential velocity component, U_θ, initially increased with r, but then started decreasing at high r. The total crossflow velocity, U, was observed to decrease monotonically as r increases. Since U_r was significantly smaller as compared to U_x and U_θ, it was neglected for most of the further analysis. Average values of U_x and U_θ were obtained by averaging them over r. These average velocity components were used to calculate and average total velocity, which

was used in the calculation of the aerodynamic Weber number, *We*. The average velocities have been listed in Table 4.1.

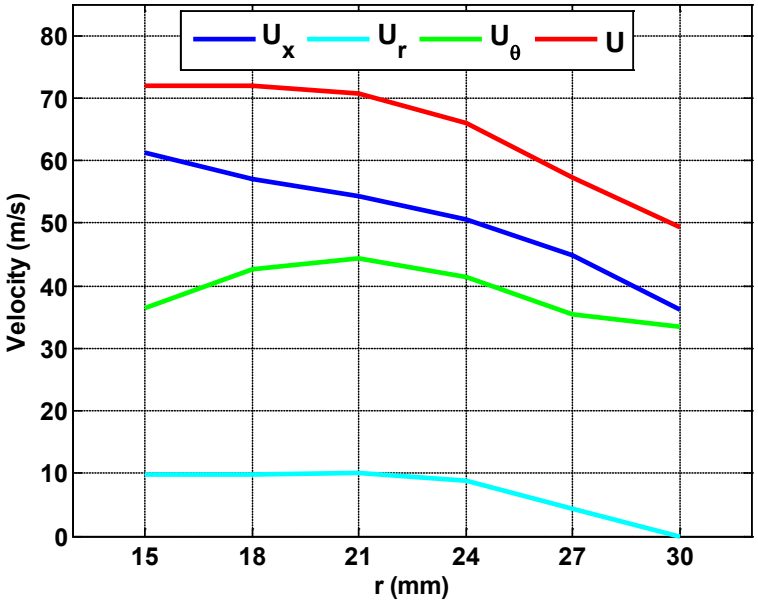

Figure 4.10 Total velocity and cylindrical velocity components for crossflow case C2 (45°, *We* = 33.91)

4.2.3 Calculating Circumferential Motion

Due to the rotating nature of the crossflow, a particle in the crossflow will follow a helical path. Neglecting radial velocity, the streamwise distance required by the particle to complete one revolution around the centerbody depends on the orientation of the velocity vector. Then the movement of any particle in the crossflow can be tracked in a X-Θ (r = constant) plane. Within this plane, the streamwise distance take by the particle to move from $\theta = 0°$ to $\theta = 0°$ (one revolution) depends on the angle of the velocity vector with the *X*-axis, as shown in Figure 4.11. This angle is called the flow angle, ψ, of the crossflow. Then, at any radial location, ψ can be determined from the total velocity and the streamwise component of the velocity, as given by equation 4.3.

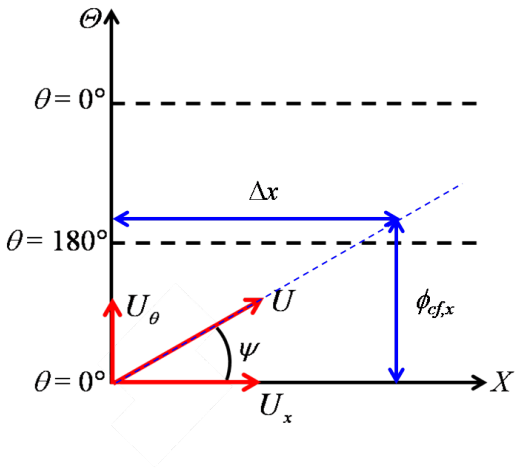

Figure 4.11 Illustration of the flow angle ψ in X-Θ (r = constant) plane

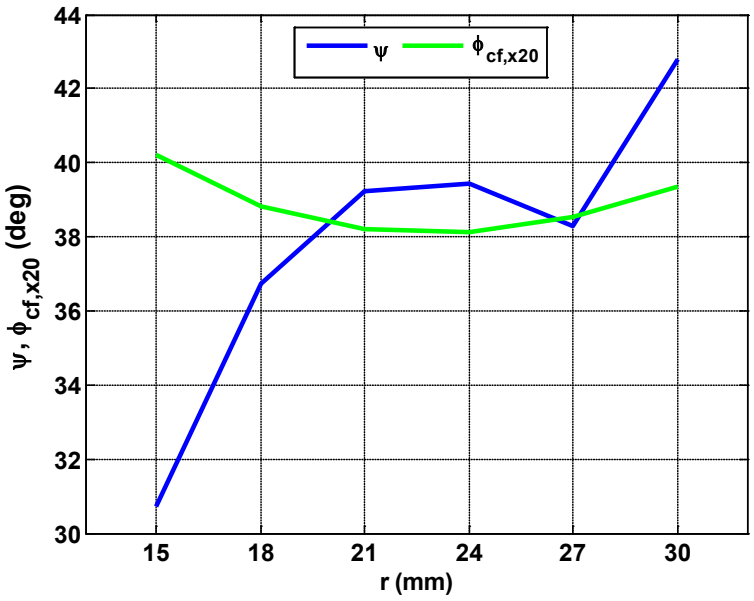

Figure 4.12 Flow angle and circumferential displacement for crossflow case C2 (45°, We = 33.91)

Since both U_x and U_θ are functions of r, it follows that ψ will also depend upon r. Figure 4.12 plots the variation of ψ with r for case C2. ψ is observed to increase with r.

$$\psi = \tan^{-1}\left(\frac{U_\theta}{U_x}\right) \tag{4.3}$$

Table 4.3 Linear fits for the flow angle, ψ

Case no	Swirler	*We*	Ψ (deg)	$\Psi = f(r)$	R^2 (linear fit)	ϕ (deg) r = 20 mm Δx = 20 mm
C1	30	32.55	30	0.9721*r + 8.6	0.9883	30.4
C2 (base)	45	33.91	37.5	1.2054*r + 9.7	0.5018	38.4
C3	60	25.98	44.1	1.538*r + 11	0.9437	51.2
C4	60	49.35	44.3	1.4937*r + 12.2	0.9234	51.8

The flow angles, ψ were observed to be nearly linear, so linear fits were obtained to describe the variation of ψ with r. The linear fits obtained for cases C1-C4 are listed in table 4.3.

Another significant parameter for a swirling flow is the circumferential displacement, ϕ, which is defined as the change in the θ-coordinate for a known displacement in x (Figure 4.11). It is more convenient to represent the circumferential displacement of the swirling crossflow as $\phi_{cf,\,x}$, where the subscripts cf and x represent the crossflow and the streamwise displacement, respectively. As r increases, the distance required to cover the same θ displacement increases, so that for constant U and ψ, the streamwise distance required to complete one revolution would increase with r. Moreover, both U and ψ change with r. Thus it also becomes necessary to study the variation of $\phi_{cf,\,x}$ with r. U_r has been neglected throughout this analysis.

Next a relation for $\phi_{cf,\,x}$ is derived. From equation 4.3, the relation between streamwise and tangential displacements for a particle of the crossflow located in a given r = constant plane is given by equation 4.4. It has been assumed that U_x and U_θ do not change with x.

$$\frac{\Delta t}{\Delta x} = \frac{U_\theta}{U_x} = \tan\psi \tag{4.4}$$

In equation 4.4, Δt represents the distance along the Θ-axis for a given r = constant plane. Then Δt can be related to the θ displacement (angles, in degrees) by,

$$\Delta t = r\Delta\theta \ \ (rad) = \frac{\pi r}{180}\Delta\theta \ \ (\deg) = \frac{\pi r}{180}\phi \tag{4.5}$$

Then $\phi_{cf,\,x}$ is obtained as,

$$\phi_{cf,\,x} = \frac{180}{\pi r}\Delta x \tan\psi \tag{4.6}$$

The flow angles, ψ used for determining $\phi_{cf,\,x}$ in equation 4.6 were obtained from the linear fits from Table 4.3 Figure 4.12 also plots the variation of $\phi_{cf,\,x}$ with r for case C2 using Δx = 20 mm. We observe that $\phi_{cf,\,x}$ increases with r. though the variation in $\phi_{cf,\,x}$ is significantly smaller than the variation in ψ.

4.2.4 Crossflow Velocity Distribution

The parameters of the crossflow that can affect the velocity distribution are the swirl angle and the aerodynamic Weber number, *We*. The effect of these parameters on the crossflow velocity distribution is considered in this section.

Figure 4.13 plots the variation of U_x with r for crossflow cases C1-C4. The (swirl angle, *We*) pairs for cases C1, C2, C3 and C4 are (30°, 32.55), (45°, 33.91), (60°, 25.98) and (60°, 49.35), respectively. U_x is observed to decrease with increasing swirl angle, which is to be expected. For an equivalent *We*, the total velocity is nearly constant. Now, tangential velocity would increase with swirl angle, so that in order to maintain a constant velocity, the streamwise component would have to decrease. The trend of U_x is similar for cases C2 and C3, where the low U_x for C3

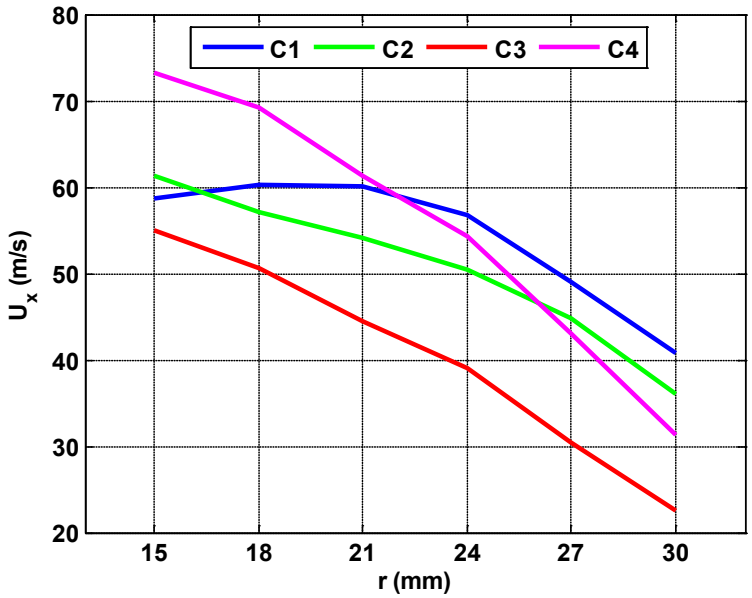

Figure 4.13 Variation of U_x with r, Cases C1 (30°, We = 32.55), C2 (45°, We = 33.91), C3 (60°, We = 25.98), C4 (60°, We = 49.35)

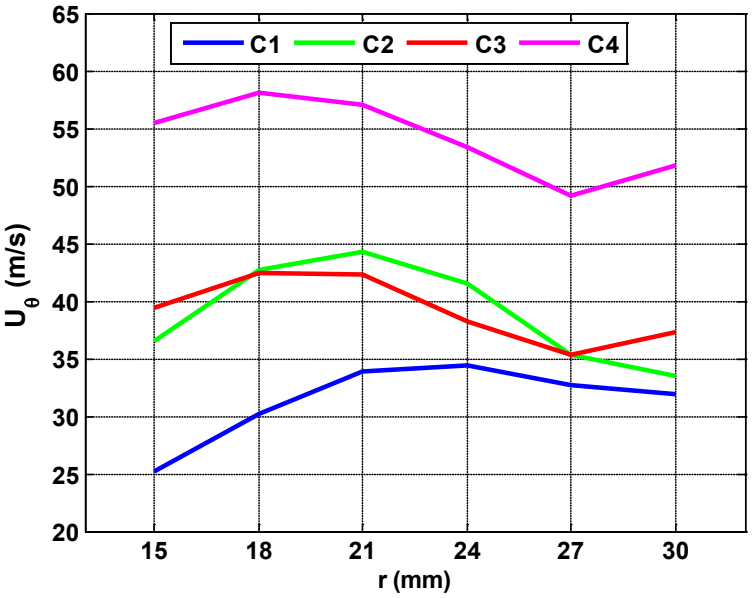

Figure 4.14 Variation of U_θ with r, Cases C1 (30°, We = 32.55), C2 (45°, We = 33.91), C3 (60°, We = 25.98), C4 (60°, We = 49.35)

occurs due to the higher swirl angle in addition to the lower *We*. For case C1, U_x initially increases with *r* before hitting a peak and then reducing as *r* increases further. Comparing cases C3 and C4, it can be seen that increasing *We* results in an increase in the magnitude of U_x.

Figure 4.14 plots the variation of U_θ with *r* for cases C1-C4. From Figure 4.10, it was seen that U_θ initially increases with *r* before decreasing at higher *r* (Case C2). A similar trend is observed for other cases. U_θ is expected to increase with swirl angle. From Figure 4.14, it can be seen that though U_θ for C1 (30°) is lower than that for C2 (45°), U_θ for C2 and C3 are nearly equal. One reason for this is that *We* for C3 is significantly lower as compared to case C2. As *We* increases, there is a significant increase in the magnitude of U_θ as seen from cases C3 and C4. Comparing U_θ for cases C2, C3 and C4, it can be seen that U_θ for the 60° swirler will be higher than that for the 45° swirler for an equivalent *We*.

Figure 4.15 plots the variation of U_r with *r* for cases C1-C4. U_r is observed to decrease as *r* increases. The magnitude of U_r is significantly smaller than the other components. Also U_r decreases with increasing swirl angle and increases with increasing *We*.

Figure 4.16 plots the variation of the total crossflow velocity, *U* with *r* for cases C1-C4. *U* decreases with increasing *r*, similar to the trend for U_x. Magnitudes of *U* for cases C1 and C2 are nearly equal due to the similar *We* for the two cases. From cases C3 and C4, it is seen that increasing *We* causes an increase in *U*.

Average values of U_x and U_θ were obtained by taking an average over *r* for each test condition. The average values were then used to obtain an average total velocity, *U* for that case, which, in turn, was used to calculate *We*. The velocities and *We* listed in Table 4.1 were obtained in this manner.

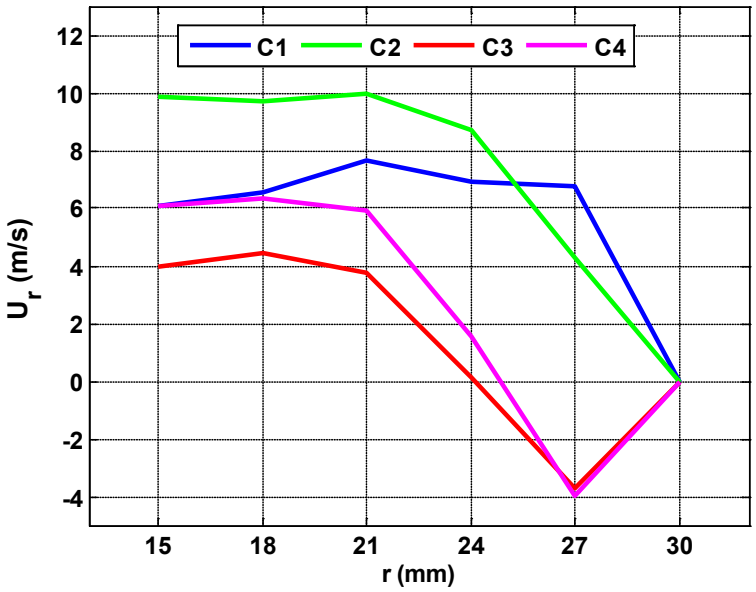

Figure 4.15 Variation of U_r with r, Cases C1 (30°, We = 32.55), C2 (45°, We = 33.91), C3 (60°, We = 25.98), C4 (60°, We = 49.35)

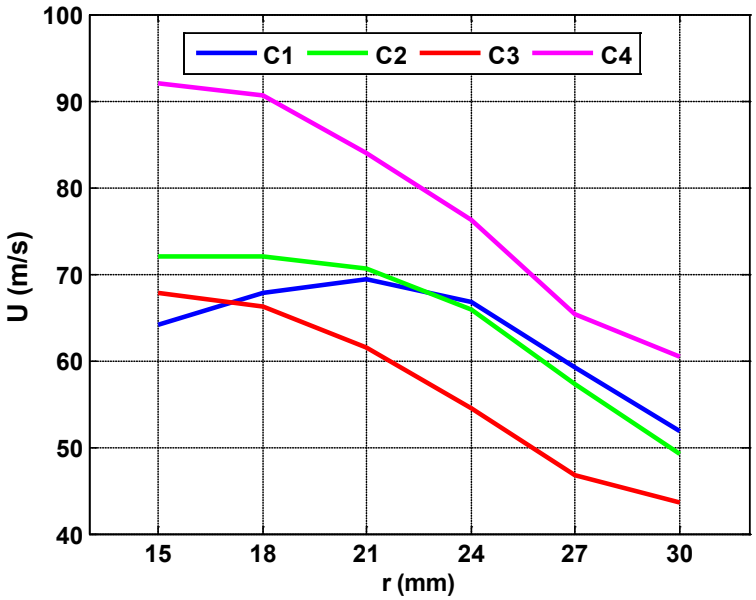

Figure 4.16 Variation of U with r, Cases C1 (30°, We = 32.55), C2 (45°, We = 33.91), C3 (60°, We = 25.98), C4 (60°, We = 49.35)

Figure 4.17 plots the flow angles, ψ, for cases C1-C4. ψ increases with r and also increases as the swirl angle increases. Moreover, only the 30° swirler seems to have imparted sufficient flow rotation to the crossflow. Average values of ψ were obtained from the average U_x and U_θ as described above and have been listed in Table 4.1. The average ψ for cases C1 (30°), C2 (45°) and C3 (60°) were 30°, 37.5° and 44.1°. This suggests that while the 30° swirler imparted sufficient flow rotation, the flow issuing out of the 45° and 60° was not tangent to the vanes at swirler exit. This is indicative of flow separation on the suction side of the vanes, due to which the flow issues out at an angle smaller than the vane exit angle. From Figure 4.17, it can be seen that *We* has no effect on ψ as observed from cases C3 and C4.

Figure 4.18 plots $\phi_{cf,\,x}$ for cases C1-C4 and Δx = 20 mm. $\phi_{cf,\,x}$ is seen to exhibit a concave shape for all cases, where it initially decreases and then starts increasing as r increases. From the discussion in section 4.2.3 $\phi_{cf,\,x}$ is expected to decrease as r increases. However, as r increases, the flow angle, ψ, increases, causing $\phi_{cf,\,x}$ to start increasing. $\phi_{cf,\,x}$ at r = 20 mm have been listed in table 4.3. For the baseline crossflow, case C2, a particle in the crossflow located at r = 20 mm undergoes a circumferential displacement of 38.4° as it moves 20 mm downstream.

4.3 Overview of Liquid Jets in Swirling Crossflow

The swirling crossflow studies were followed by studies of water jets injected into the crossflow. One of the issues with measurement of the jet is that the direction of the jet trajectory is unknown. Due to the helical path of the crossflow, the jet path will also curve around the centerbody. Now, since the jet trajectory is at an angle to the *YZ* plane, the jet cross-section is no longer

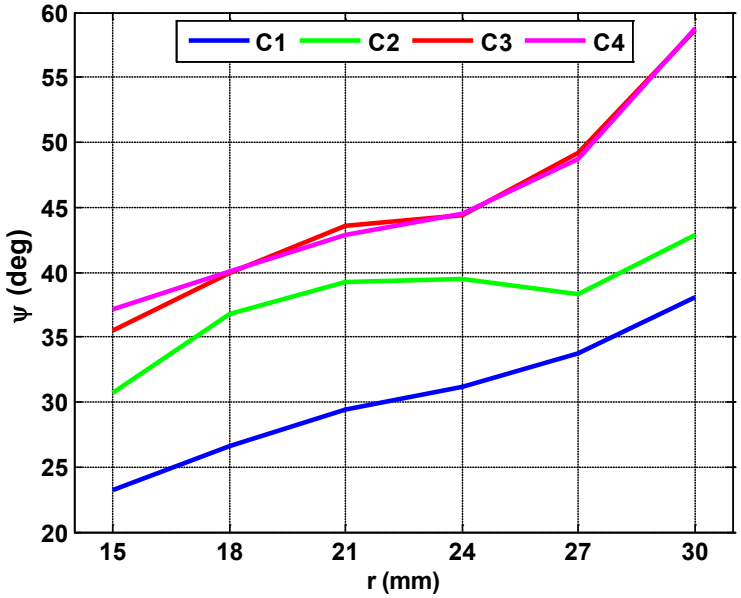

Figure 4.17 Variation of ψ with r, Cases C1 (30°, We = 32.55), C2 (45°, We = 33.91), C3 (60°, We = 25.98), C4 (60°, We = 49.35)

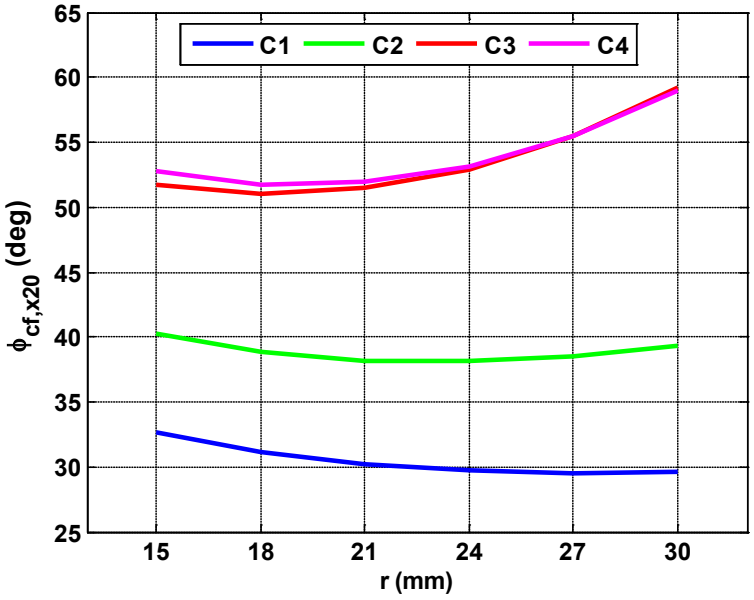

Figure 4.18 Variation of $\phi_{cf,\,x}$ with r, Cases C1 (30°, We = 32.55), C2 (45°, We = 33.91), C3 (60°, We = 25.98), C4 (60°, We = 49.35)

contained within the *YZ* plane, but is at an angle to it. It is difficult to predict this angle in advance. Also, as the jet progresses downstream, the angle might change.

To overcome this issue, PIV studies were conducted at multiple, parallel planes. The results from the different planes can then be collated together to create a 3-D measurement domain containing the jet. The following sub sections give an overview of the PIV setup for measurements.

4.3.1 PIV Setup for Measurements in Cross-Sectional Planes

It was shown in section 4.1.2 that in order to be able to create a good cylindrical domain, it is necessary to have data in the cross-sectional, or *YZ* planes. Hence one set of PIV measurements was carried out in the x = constant planes, with measurements being conducted between x = 0:25 mm, measurement planes being separated by 2.5 mm. The Mie-Scattering images obtained from PIV were used to recreate the 3-D jet plume. The boundary of the 3-D plume was extracted to study jet penetration. Additionally, the PIV results yielded the V_y and V_z components of the jet droplet velocities, which were converted into polar velocity components, V_r and V_θ. Additionally, the measurement domain was converted to cylindrical to study the jet penetration and polar velocity components. The test conditions are listed in Table 4.3, with a "c" following the test case number to indicate measurement in a cross-sectional plane. Thus, cross-sectional measurements for the baseline jet, case J3 (45°, We = 83.2, q = 12.02), are represented by case J3c.

Figure 4.19a shows a schematic of the PIV setup used for measurements in the cross-sectional planes. It is worth restating that cross-sectional planes imply a cross-section of the test chamber (i.e. *YZ* planes) and not of the jet itself. From Figure 4.19a shows that the camera had to be inclined to the measurement plane in order to avoid impacts from the water spray and the high-speed crossflow air issuing out of the test chamber. A Scheimpflug adapter was used to ensure

that the plane of focus of the camera was parallel to the *YZ* plane. The PIV software, Davis, intrinsically corrects the images and provides results for the corrected planes.

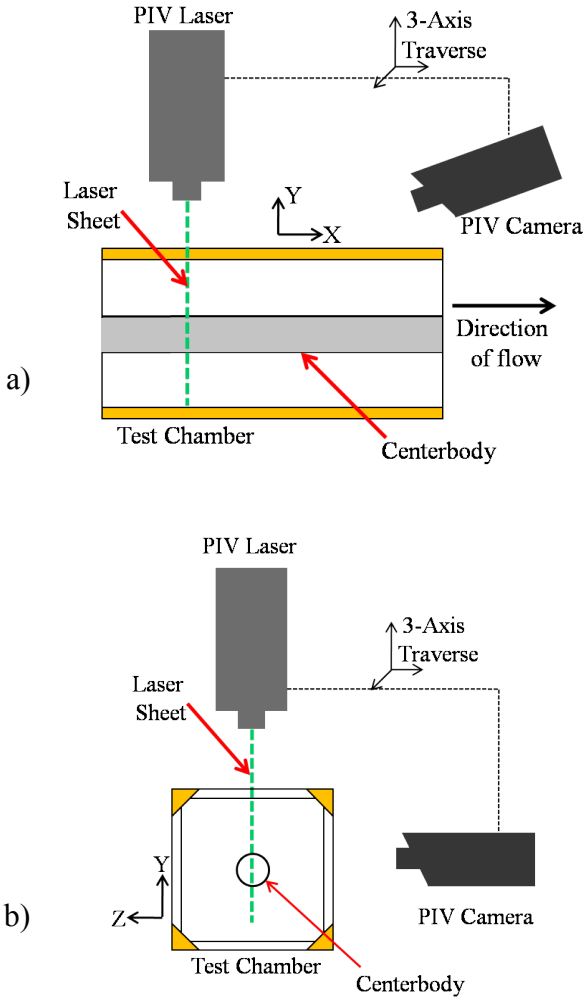

Figure 4.19 Schematic of PIV setup for measurement in: a) Cross-sectional planes, b) Streamwise planes

4.3.2 PIV Setup for measurements in Streamwise Planes

PIV studies in the cross-sectional planes yielded two velocity components. However, to fully understand the evolution of the jet, it is necessary to know the streamwise component of the veloci-

ty as well. Hence some of the test cases were repeated with measurements in the streamwise planes (i.e. *XY* planes), with measurements being conducted between z = 0: -25 mm, measurement planes being separated by 2.5 mm. The PIV setup for these measurements is shown in Figure 4.19b. The test conditions are listed in table 4.2 with an "s" following the case number to indicate measurements in streamwise planes. The same case number indicates that the test conditions were essentially the same to ensure compatibility between the two sets of results. The two sets of velocity results could then be compiled together to create 3-D velocity information.

4.4 Evolution of the Liquid Jet in Swirling Crossflow

4.4.1 Creating the 3-D Jet Plume

PIV results consist of Mie-Scattering images and the velocity maps. The Mie-Scattering images are essentially intensity maps, with coordinate information within the image plane and values of intensity at each location in the measurement grid. Thus we have intensity maps for each measurement plane, ranging from x = 0 mm to x = 25 mm. Examples of Mie-Scattering images for case J3c at x = 5, 10 mm are shown in Figure 4.20.

A Matlab program was created to create a 3-D intensity map of the jet. The program first created a polar grid and mapped intensity values from the *YZ* measurement grid onto it following the procedure outlined in section 4.1.2. It then normalized the intensities in each polar plane by the maximum intensity in that plane. The last step was to combine the individual polar planes into a single 3-D cylindrical domain by adding the third (x) coordinate.

The intensity value in a Mie-Scattering image is proportional to the total droplet surface area, which is related to the droplet density in an area of the image. Images near the location of inject-

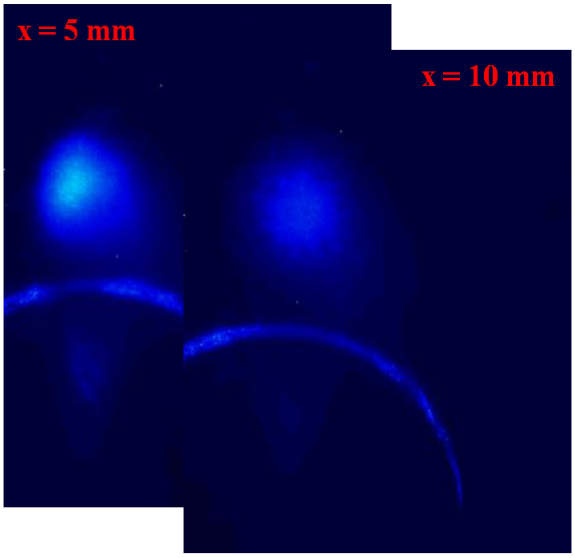

Figure 4.20 Cross-sectional Mie-Scattering images, Case J3c, (45°, *We* = 83.2, *q* = 12.02)

tion (low *x*) include a very concentrated area of liquid, resulting in very high intensities. Reflection from the jet surface creates a glare producing high intensities in the surrounding area, which are low compared to the intensities within the jet itself, but still have a significant magnitude. As the jet progresses downstream, the droplet concentration reduces, causing the magnitude of the peak intensity values in these planes to decrease. It is possible that the magnitude of the intensity in the glare in the first few planes could be comparable to the magnitude of the intensity in the jet region in some of the latter planes. Then, if the actual intensity values are used, there is a chance of misrepresenting the jet boundary. To avoid this error, the intensities in each measurement plane were normalized by the maximum intensity in that plane. This enables comparison between the different measured planes as the magnitudes of the intensities are not comparable.

The visualization software, Tecplot was used to generate a 3-D plot of the measurement domain. Tecplot also has the capability of plotting isosurfaces of the intensity. An isosurface is a surface created by joining all locations having the same value for the given variable. For locations where

no information is available, Tecplot performs interpolation to yield a continuous surface. Thus isosurfaces of the jet intensities essentially recreate the 3-D jet plume.

4.4.2 Evolution of the Baseline Jet (Case J3c)

Figure 4.21a shows the isosurfaces for the baseline jet, case J3c. Figures 4.21b, c and d show projected views of the spray plume onto the *XY*, *XZ* and *YZ* planes respectively. Figure 4.21 also illustrates the limits of the 3-D cylindrical domain and the location of the centerbody. The jet plume is observed to follow a path similar to the helical path of the crossflow. The crossflow momentum tries induces drag on the jet which tries to align the path of the jet to the crossflow trajectory. As a result, the jet follows the curved trajectory seen. Due to this, the jet cross-section is at an angle to the R-Θ (YZ) plane, causing it to appear elliptical in figure 4.21d.

4.5 Jet Penetration

Section 4.4.1 we showed that jet surface could be recreated. The jet boundary could then be extracted and used for penetration analysis. However it is first necessary to review the significance of the 3-D nature of the jet trajectory and how it affects jet penetration

4.5.1 Effect of the 3-D nature of the Jet Trajectory on Penetration

The simple case of a transversely injected jet in a uniform crossflow is considered first. The crossflow induces drag on the fluid of the jet. As a result, jet fluid gains momentum directed along the direction of the crossflow. Additionally, some of the initial momentum of the jet gets

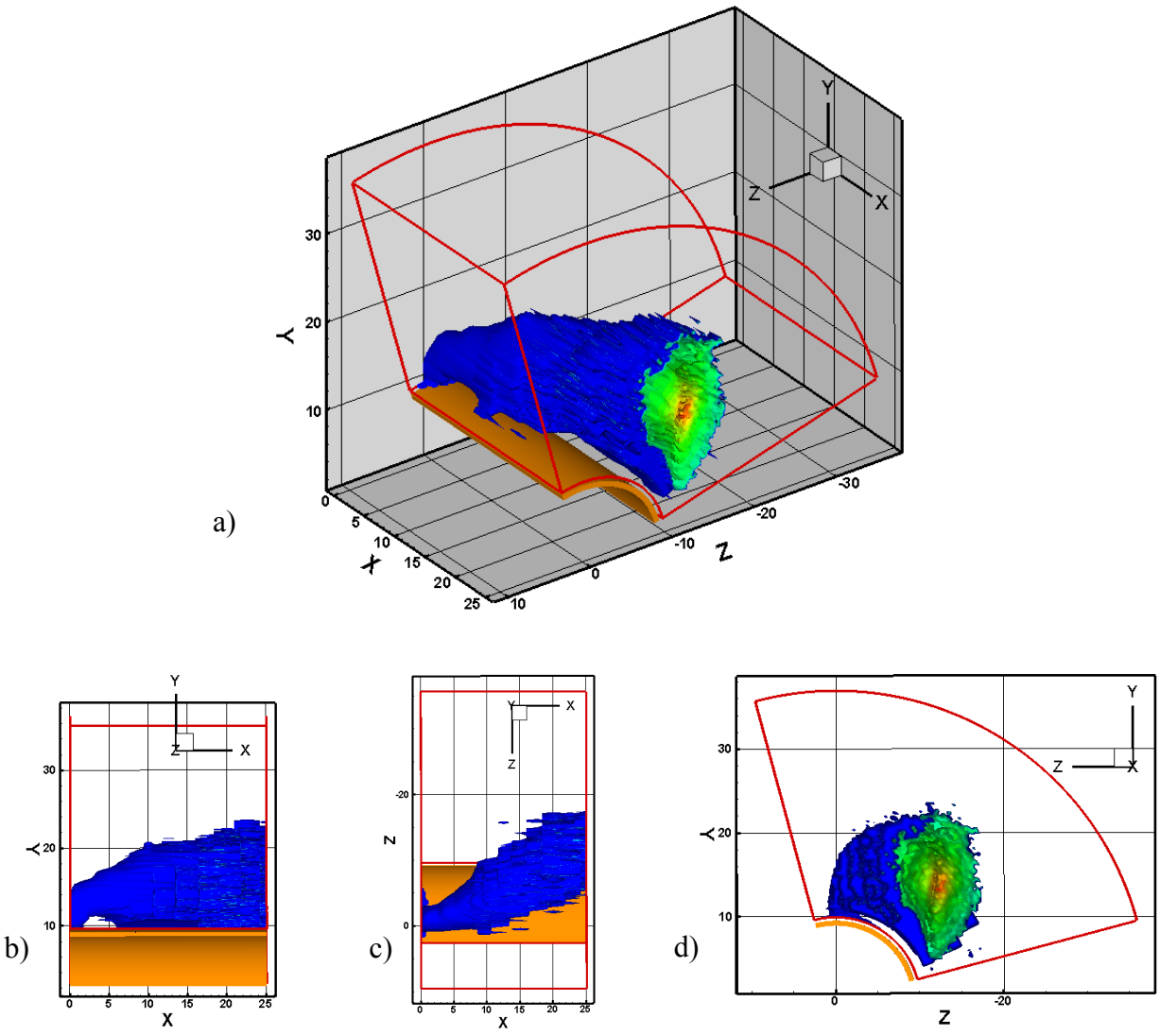

Figure 4.21 Spray plume for the baseline jet, case J3c (45°, *We* = 83.2, *q* = 12.02), a) 3-D view of the spray plume, b) Spray plume projected onto the *XY* plane, c) Spray plume projected onto the *XZ* plane, d) Spray plume projected onto the *YZ* plane

redirected along the momentum gained from interaction with the crossflow. Thus jet particles start moving in the direction of the crossflow and the jet trajectory gets aligned with the direction of the crossflow. It then follows that the jet trajectory would always align itself with the direction of the crossflow velocity provided the undisturbed crossflow trajectory is a straight line. Then

the only relevant parameter about the jet trajectory is the transverse location of the jet at any point along the flow direction. Thus the jet trajectory information is one-dimensional.

Now consider a simplified version of swirling crossflow while observing from within the cylindrical domain. This is akin to cutting the domain along a θ = constant plane and flattening it out, so that the r = constant plane is a flat surface.

Now if it is assumed that U_r is zero and that U_x and U_θ do not change with r, then the resulting flow is uniform, though the velocity is directed at an angle to the x-axis. This is plausible as the nature of the domain means that any particle leaving the domain at $\theta = 360°$ re-enters the domain on the other side at $\theta = 0°$ at the same (x, r) location. Then the aerodynamic forces exerted by the jet would cause the jet trajectory to align itself with the direction of the crossflow. Thus, the flow angle of the jet will be equal to the flow angle of the crossflow, within this domain. Thus even in this domain, the jet trajectory is one-dimensional, with the only relevant parameter being the transverse location of the jet at any point along the flow direction of the crossflow.

However, if the same flow is now considered from an inertial reference frame, it can be seen that the trajectory of the jet is no longer along a straight line, but is rather curved, tracing a helical path. Then even though a particle in the jet was to move with constant speed, the direction of velocity changes, and as a result, the particle is under acceleration. Such acceleration is known as centripetal acceleration, since it is directed towards the center of curvature and causes the particle trajectory to curve in on itself. This centripetal acceleration is being imposed on the jet be the swirling crossflow by means of aerodynamic forces. However the tendency of the jet is to oppose the aerodynamic forces of the crossflow. This results in an effect similar to that of "centrifugal acceleration" whereby the particles in the jet seem to undergo acceleration directed radially outwards, as compared to the crossflow. The result is that the circumferential displacement

of the jet would be lower than that of the crossflow causing the average flow angle of the jet to be lower than that of the crossflow. Then the jet trajectory becomes two dimensional, as in addition to the radial (transverse) height of the jet there is also a need to monitor the circumferential location of the jet to complete the description of the jet trajectory.

It should be noted that the actual crossflow is more complicated due to the presence of U_r and due to the variation of U_x and U_θ with r. Thus the nature of the jet trajectory for the swirling crossflow is two-dimensional, and needs to be monitored along both dimensions. It is more convenient to break it up into two different modes of penetration, which will be called as the "radial" penetration and the "circumferential" penetration. These modes of penetration are defined in the following sections.

4.5.2 Radial Penetration, r_P

Radial penetration is equivalent to the penetration for a typical transverse jet in a uniform crossflow. Here, radial penetration, r_P, is defined as the radial height of the top of the jet periphery from the surface of the centerbody at any streamwise location. Now, since the origin is defined at the axis of the centerbody, r_P, is the difference between the radial location of the jet periphery and the radius of the centerbody, r_{cb}. We know that r_{cb} is 0.96 cm (3/8 inch).

It is common practice to non-dimensionalize the jet penetration by the nozzle diameter in order to allow comparison between different studies. Here also, the radial distance is divided by the jet diameter, d, to obtain non-dimensional radial penetration, r_P, as shown in equation 4.7.

$$r_P\left(x/d\right) = \frac{\left(r\left(x/d\right) - r_{cb}\right)}{d} \tag{4.7}$$

4.5.3 Circumferential Penetration, ϕ_P

It was shown in section 4.5.1 that due to centrifugal acceleration, the circumferential displacement for the jet will be lower than that of the crossflow for the same streamwise displacement. The tendency of the jet is to oppose circumferential displacement, so that the difference in the circumferential displacements is a measure of the jet's penetration. Then circumferential penetration, ϕ_P, is defined as the difference in the circumferential displacements of the crossflow, ϕ_{cf}, and that of the jet, ϕ_j, for a streamwise displacement from $x/d = 0$ to the location where ϕ_P is being considered. Then ϕ_P can be obtained from equation 4.8. The use of non-dimensional distance x/d allows us to relate the radial and circumferential penetration of the jet. Now since ϕ_{cf} varies with r, it is difficult to calculate ϕ_P as at any x the jet occupies a range of r. Moreover, the radial extent of the jet keeps changing as it moves downstream. Since the primary interest is in determining ϕ_P to enable qualitative comparison between cases, representative values of ϕ_{cf} and ϕ_j will be used. The representative value of ϕ_{cf} was chosen to be ϕ_{cf} at $r = 20$ mm. ϕ_j for the top edge of the jet was selected to be the representative ϕ_j for the jet. The concept of the top edge of the jet is explained below in section 4.5.4.

$$\phi_P(x/d) = \left(\phi_{cf}(x/d) - \phi_{cf}(0)\right) - \left(\phi_j(x/d) - \phi_j(0)\right)$$

$$\phi_P(x/d) = \phi_{cf}(x/d) - \phi_j(x/d) \tag{4.8}$$

4.5.4 Extracting the 3-D Jet Trajectory

The recreation the 3-D jet plume was demonstrated in section 4.4.1. Next the boundaries of the jet plume need to be extracted in order to investigate the jet penetration. This process was carried

out in the cross-sectional ($R\Theta$) planes, which were also the measurement planes. The normalized intensity values were used for boundary extraction. The process was carried out by a Matlab program as described below.

A threshold of 10% of the maximum intensity was applied to the $R\Theta$ plane. All locations with intensities of below 10% of the maximum intensity were assumed to be the crossflow. A boundary detection algorithm was then used to trace the boundary of the jet plume. The boundary detection algorithm first converts the intensity map to binary, with an intensity of 1 for grid points located in the jet and 0 for all other locations. Then using a neighborhood search, all interior points were eliminated. This process also eliminates small solitary droplets and specks due to noise located outside the jet plume.

For each $R\Theta$ plane, 4 boundary points were selected, marking the radial and circumferential extremities of the jet plume. The radial extremities mark the top and the bottom (in a radial sense) of the jet periphery. The circumferential extremities mark the circumferentially advancing and receding edges of the jet. As seen from downstream the jet spins in a clockwise direction, so that the advancing side is referred to as the "right" side and the receding side is referred to as the "left" side of the jet.

Thus for each case, 4 lines were traced, marking the progress of the top, bottom, left and right edges of the jet. The points along each line have radial as well as circumferential coordinates, illustrating the two-dimensional nature of the jet penetration. The top edge is considered representative of the jet, and most of the following discussion will use the top edge of the jet to illustrate penetration. The left and the right edges will be used to illustrate the circumferential penetration of the base jet.

4.5.5 Comparison of Jet Penetration to Literature (Uniform Crossflow)

As was reported in Chapter 1, several works have studied penetration of liquid jets in uniform crossflow. Several correlations exist in the literature. However, there is usually some disagreement between any two correlations from the crossflow. Here, a correlation predicted from a previous work of this author, Tambe 2004 [27], was chosen for comparison. In terms of the variables used for the current study (i.e. y replaced by r), the penetration correlation from Tambe 2004 is given in equation 4.9. From equation 4.9 it can be seen that the penetration depended only on q.

$$\frac{r}{d} = 1.55 q^{0.53} \ln\left(1 + 1.66 \frac{x}{d}\right) \tag{4.9}$$

4.5.6 Penetration of the Baseline Jet (case J3c)

Figure 4.22 shows the radial penetration, r_P, for the baseline jet, case J3c along with the prediction from the correlation [27] for an equivalent q of 12. The near-field penetration of the jet in swirl flow is observed to be similar to that of the correlation. However, as the jet moves further downstream, the penetration of the jet in swirling crossflow is observed to be significantly higher than the jet from the correlation. One of the reasons for high r_P could be the effect of centrifugal acceleration of the jet. Additionally, from Figure 4.10, it was observed that the total crossflow velocity, U, decreases with r. This creates a similar situation to the shear-laden crossflow in Chapter 3 with $UR < 1$, so that the jet will experience higher incremental penetration. As a result the jet in swirling crossflow penetrates higher as compared to an equivalent jet in a uniform crossflow.

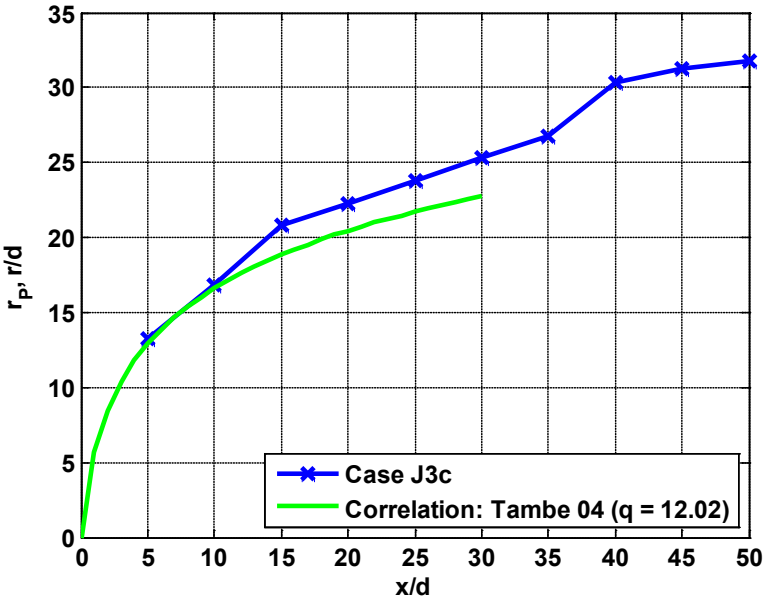

Figure 4.22 Radial penetration, r_P, for the baseline jet, case J3c (45°, We = 83.2, q = 12.02)

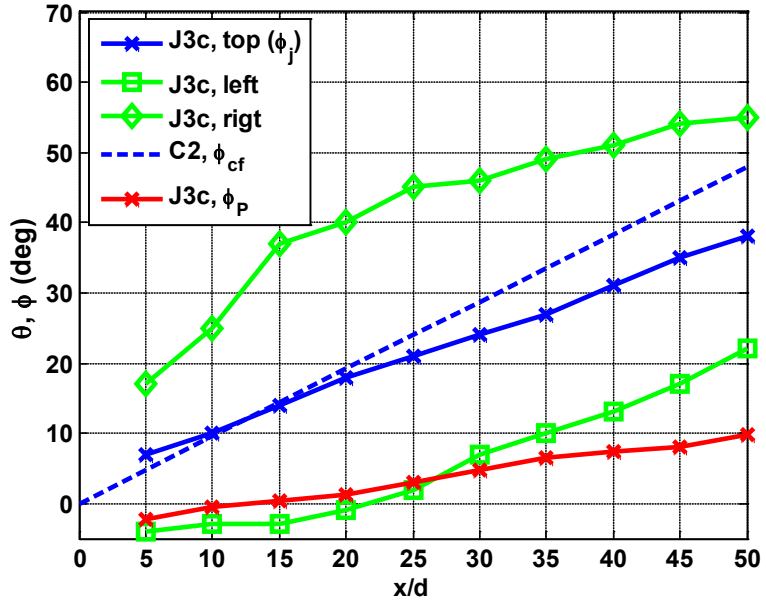

Figure 4.23 Circumferential penetration, ϕ_P, for baseline jet, case J3c (45°, We = 83.2, q = 12.02)

The circumferential progress of the jet is considered next. Figure 4.23 plots the circumferential progress of the top, left and right edges of the spray plume for the baseline jet, case J3c. The top periphery is observed to be slightly closer to the left edge as compared to the right edge. This occurs since the jet cross-section exists at an angle to the x = constant ($R\Theta$) plane. Figure 4.23 also plots the representative ϕ_{cf} of the crossflow (at r = 20 mm). The circumferential penetration of the jet, ϕ_P, can then be obtained as the difference between ϕ_{cf} and ϕ_j of the top edge of the jet, and is also plotted in Figure 4.23. The relation between ϕ_P and x/d is seen to be nearly linear in nature. The positive magnitude of ϕ_P reinforces the concept of circumferential penetration.

4.5.7 Effect of Crossflow and Jet Parameters on Jet Penetration

The effect of jet and crossflow parameters on jet penetration are considered next. The crossflow parameters are the swirl angle and the aerodynamic Weber number, *We*. The jet parameter is the momentum flux ratio, q.

Figure 4.24 illustrates the effect of *We*, q on the radial penetration by plotting r_P for cases J3c, J2c and J4c. Cases J2c and J3c have nearly equal q due to which the penetration correlations from Tambe 04 [27] for these two cases neatly overlap. However *We* increases from 42.27 for J2c to 83.72 for J3c. The increase in *We* has no significant impact on r_P. Cases J3c and J4c have same *We*, but q increases from 12.05 for J3c to 24.01 for J4c. From Figure 4.24 it is seen that r_P increases with q. For both J3c and J4c, jet penetrations are close to the correlations for low x/d, though for high x/d, the penetration for the jets from the current study seem to be significantly higher than the projected correlations.

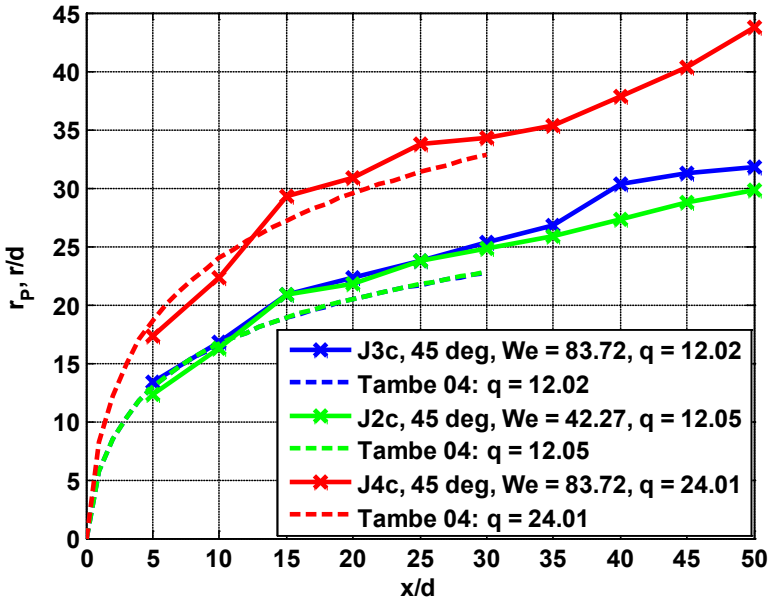

Figure 4.24 Effect of *We*, *q* on r_P

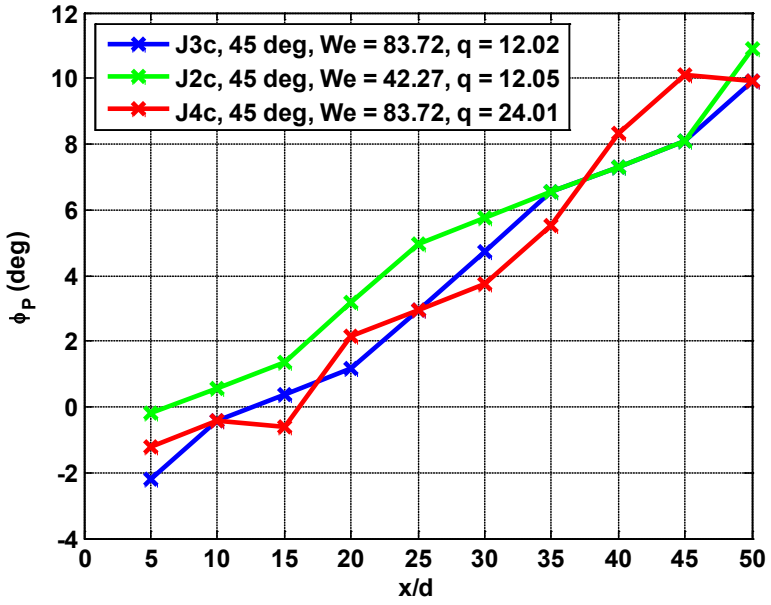

Figure 4.25 Effect of *We*, *q* on ϕ_P

Figure 4.25 plots the circumferential penetration, ϕ_P for cases J3c, J2c and J4c, respectively, to illustrate the effect of *We*, *q*. ϕ_P for all three cases are nearly equal indicating that *We* and *q* have no significant effect on ϕ_P.

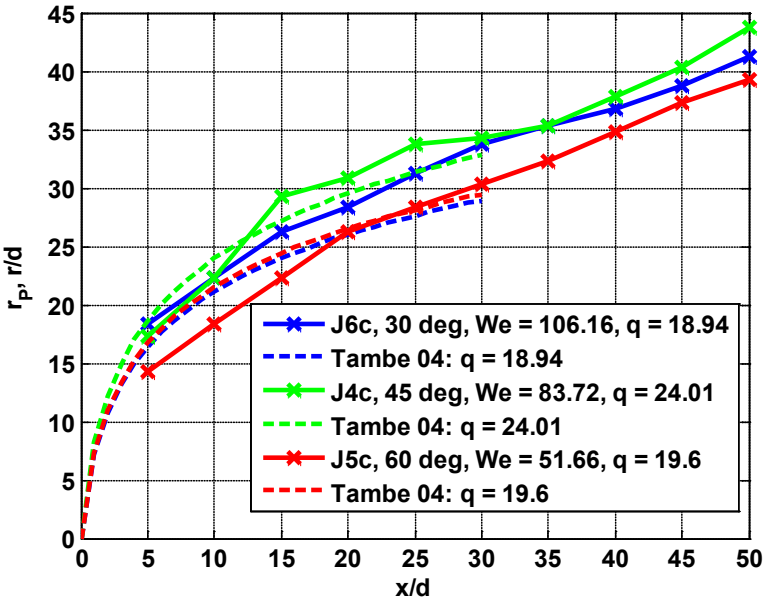

Figure 4.26 Effect of swirl angle on r_P

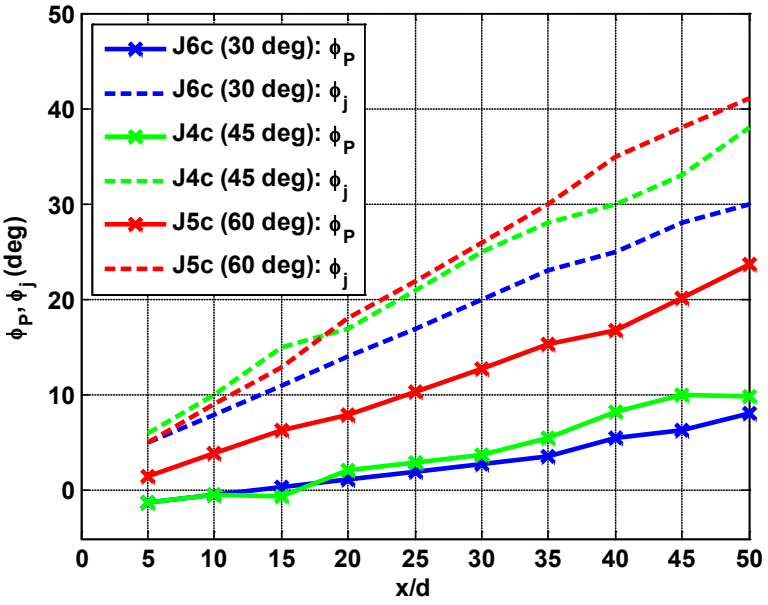

Figure 4.27 Effect of swirl angle on ϕ_P

The effect of swirl angle on the radial penetration, r_P, is considered next. Figure 4.26 plots r_P for cases J6c (30°), J4c (45°) and J5c (60°) along with the penetration correlations from Tambe 04 for the corresponding values of q. The radial penetrations for all three cases are very close to the

predicted penetrations from the correlation in the near region. However, beyond the initial region, the penetration for case J6c (30°) seems to be the highest, and is nearly equal to that for case J4c (45°), even though q for J4c is higher. An explanation for this could be that as swirler angle increases, more tangential momentum is imparted to the jet, causing reduced resistance in the radial direction, leading to lower r_P.

Figure 4.27 plots the circumferential penetration, ϕ_P for the same cases, J6c, J4c and J5c to demonstrate the effect of swirl angle on ϕ_P. ϕ_P for the 30° swirler (J6c) and the 45° (J4c) swirler are seen to be very close, though ϕ_P for the 45° swirler is slightly higher. It is noted here that the difference in q and We between cases J4c and J6c are not relevant since we have seen that they have no significant effect on ϕ_P. ϕ_P for the 60° swirler (J5c) is significantly higher than that for the 45° swirler. Thus it can be inferred that ϕ_P increases with an increase in the swirl angle. Figure 4.27 also plots the circumferential displacement, ϕ_j, of the jets showing that ϕ_j increases with swirl angle as well. Thus, as swirl angle increases, the circumferential displacements of the jets (ϕ_j) increase, but not as much as the circumferential displacements of the crossflow (ϕ_{cf}), causing the circumferential penetrations of the jets (ϕ_P) to increase as well.

4.6 Droplet Velocities: Cross-Sectional Planes

The Mie-Scattering images from PIV results have been analyzed to study the progress of the jet plume and analyze the jet penetration. Next the velocity maps obtained from PIV will be considered. Figure 4.28 plots the velocity maps obtained at x = 5, 10 mm for the baseline jet, case J3c. The domain was transformed to a polar domain, and polar components of velocities were obtained, to analyze droplet velocities in the new cylindrical domain.

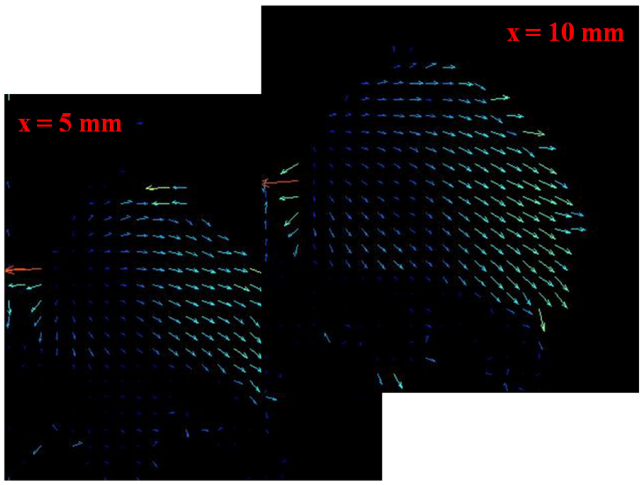

Figure 4.28 Cross-sectional velocity maps from PIV, Case J3c (45°, *We* = 83.2, *q* = 12.02)

4.6.1 Obtaining Polar Components of Droplet Velocities

The cross-sectional velocity maps were transformed into polar coordinates following the procedure outlined in section 4.1.2. Next the velocity components were transformed in a manner similar to crossflow velocity components following the procedure given in section 4.2.2. The geometry used for the transformation has been shown previously in Figure 4.8. The final relations for obtaining the polar velocity components of droplet velocity, V_r and V_θ, are given in equations 4.10 and 4.11.

$$V_r = V_y \cos\theta - V_z \sin\theta \tag{4.10}$$

$$V_\theta = -V_y \sin\theta - V_z \cos\theta \tag{4.11}$$

The individual planes were then collated together, while adding the third (x) coordinate information, thus creating a cylindrical measurement domain. All analysis of the velocities measured in the cross-sectional planes will be conducted in this cylindrical domain.

4.6.2 Cross-Sectional Droplet Velocity Distribution for the Baseline Jet (Case J3c)

Figure 4.29 shows the in-plane velocity vectors for case J3c for streamwise planes located at x = 5, 10, 15 and 20 mm. From Figure 4.29 it can be seen that the bulk of the velocity vectors are directed in the tangential direction. This clearly shows the tangential spread of the jet and also the circumferential shift of the jet plume. However, the jet also grows in the radial direction, though this is not immediately evident from the velocity vectors.

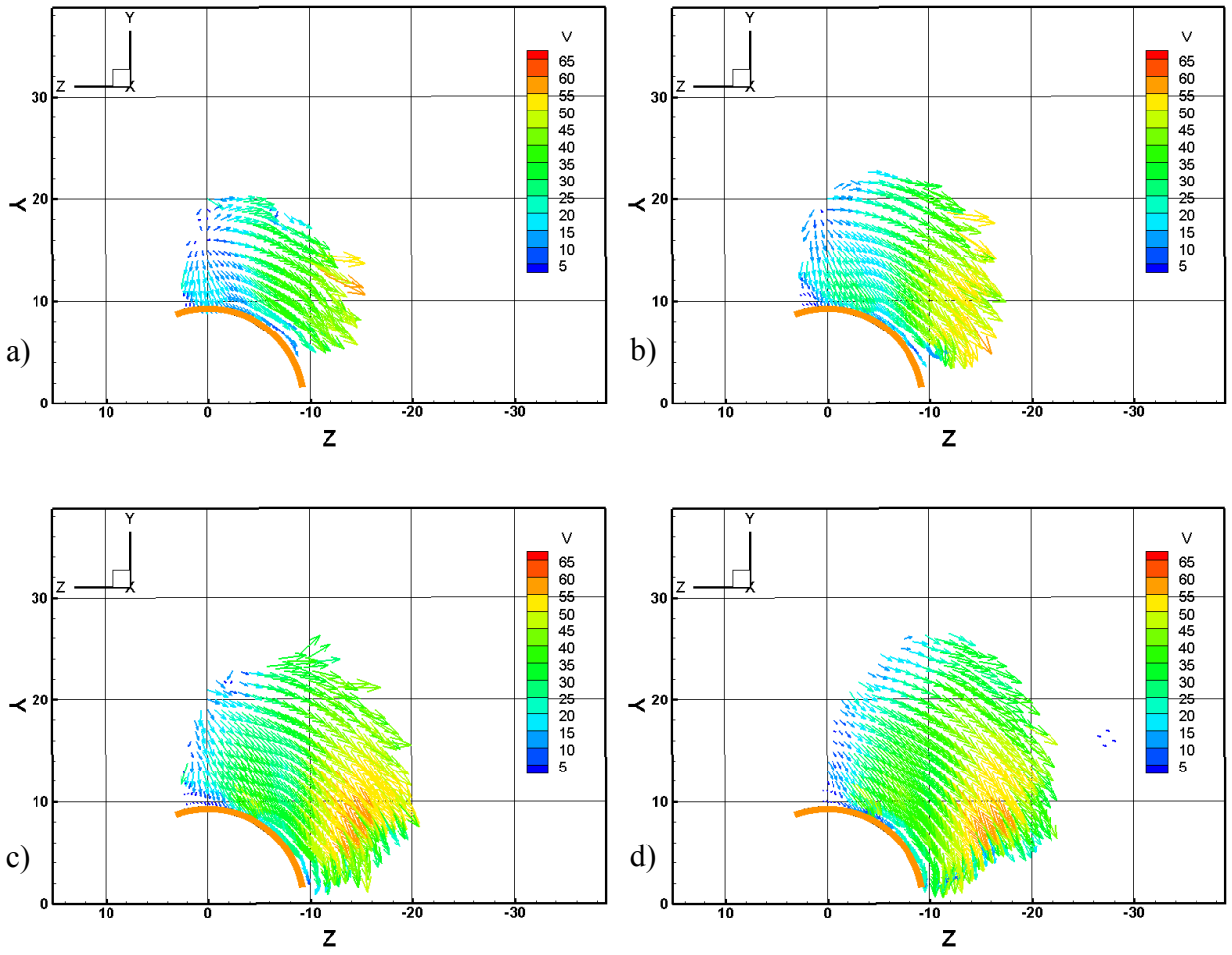

Figure 4.29 Droplet velocity vector distribution for case J3c (45°, We = 83.2, q = 12.02), a) x = 5 mm, b) x = 10 mm, c) x = 15 mm, d) x = 20 mm

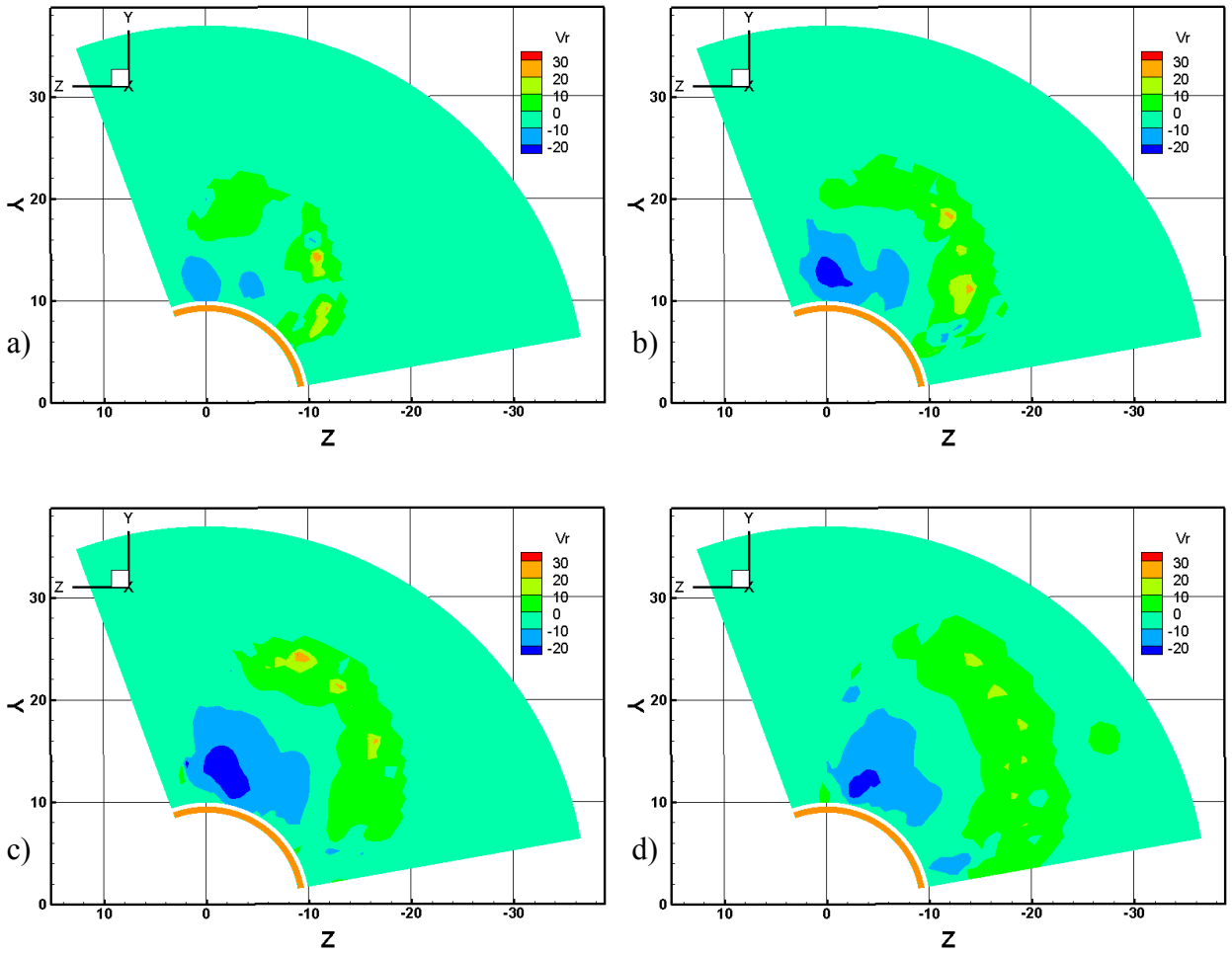

Figure 4.30 Droplet radial velocity, V_r, distribution for case J3c (45°, We = 83.2, q = 12.02), a) x = 5 mm, b) x = 10 mm, c) x = 15 mm, d) x = 20 mm

It is possible to gain further insight into the jet behavior by studying the two velocity components separately. Figure 4.30 plots contours of the radial component of droplet velocity, V_r, for case J3c at the same locations as shown in Figure 4.29. In Figure 4.30, a band of positive V_r is observed near the upper edge of the jet periphery. Also there is a zone of negative V_r located near the bottom of the jet periphery, concentrated mostly near the left edge. These bands exhibit the tendency of the jet plume to expand in the radial direction. Additionally, as the jet progresses downstream, the band of positive V_r near the upper periphery grows in size, while at the same

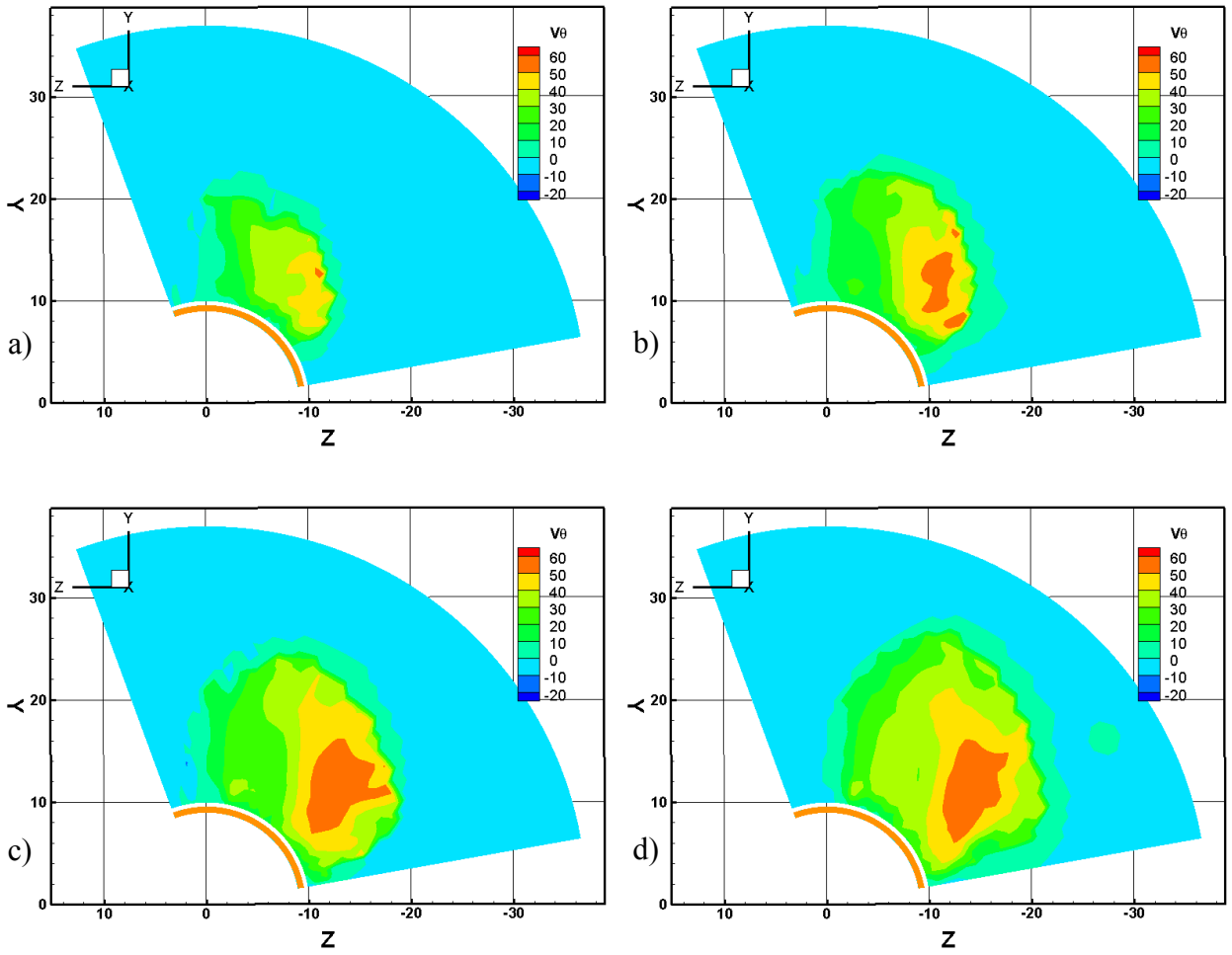

Figure 4.31 Droplet tangential velocity, V_θ, distribution for case J3c (45°, We = 83.2, q = 12.02), a) x = 5 mm, b) x = 10 mm, c) x = 15 mm, d) x = 20 mm

time, the magnitude of V_r decreases. This indicates that the potential for incremental radial penetration decreases as the jet progresses downstream, which is to be expected.

Figure 4.31 plots contours of the tangential component of the droplet velocity, V_θ, for case J3c at streamwise locations of x = 5, 10, 15 and 20 mm respectively, the same as Figures 4.29 and 4.30. In each plane, a region of high V_θ is seen near the right (advancing) edge of the jet periphery. In general, V_θ increases from the left (receding) edge to the advancing edge, i.e. circumferential displacement of the receding edge is lower than that of the advancing edge. This indicates that

the jet plume is expanding in the circumferential direction, which is evident from figure 4.31. It is interesting to note that the highest value of V_θ, observed at x = 25 mm (not shown) was approximately 63 m/s. The mean tangential velocity of the crossflow, U_θ, is 61.82 m/s (Table 4.2). This suggests that the jet lags the crossflow in the circumferential direction.

4.7 Droplet Velocities: Streamwise Planes

Additional PIV tests were conducted in streamwise (*XY*) planes to add to the knowledge gained from the cross-sectional velocity components in section 4.6. The test conditions used were a repeat of a selected few cases studied with cross-sectional PIV. This was done to ensure that the datasets could be combined to create a 3-D velocity distribution. Measurement in *XY* planes is indicated by an "s" following the case number in table 4.2. Measurements were conducted at planes ranging from z = 0 mm to z = −25 mm, with a separation of 2.5 mm between measurement planes. The negative value of the z-coordinates occurs due to the orientation of the axes chosen and the clockwise nature of the swirl. The region of interest for this study was the top right quarter of the cross-section of the test chamber ($Y \geq 0$, $Z \leq 0$).

Figure 4.32 plots the velocity maps obtained for the baseline jet, case J3s at z = -5, -10 mm. Knowing that the radius of the centerbody, r_{cb}, is 9.6 mm, the centerbody would still exist at the measurement plane of z = -5 mm but not at z = -10 mm. Even though the centerbody is not visible in Figure 4.32, the effect of the presence of the centerbody is apparent if Figure 4.32a, where the velocity vectors get cut off at a straight horizontal line, below which no velocity vectors were detected. This horizontal line probable represents the centerbody. No such demarcation was observed in Figure 4.32b (z = −10 mm) as expected.

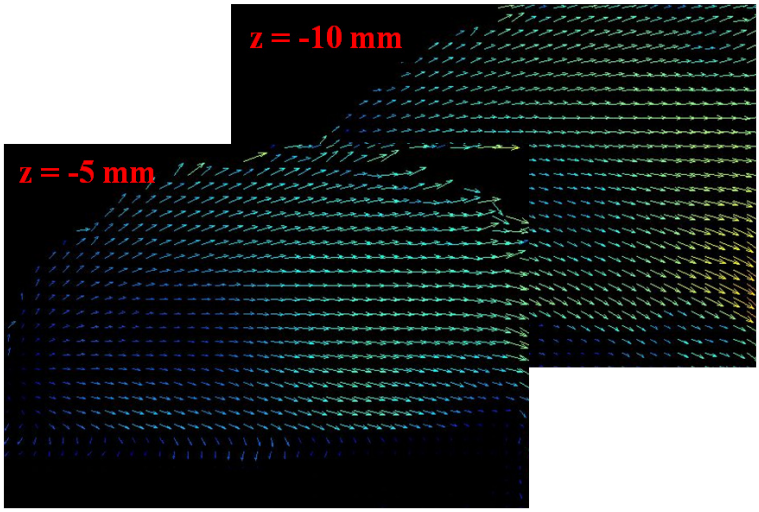

Figure 4.32 Streamwise velocity maps from PIV, Case J3c (45°, *We* = 83.2, *q* = 12.02)

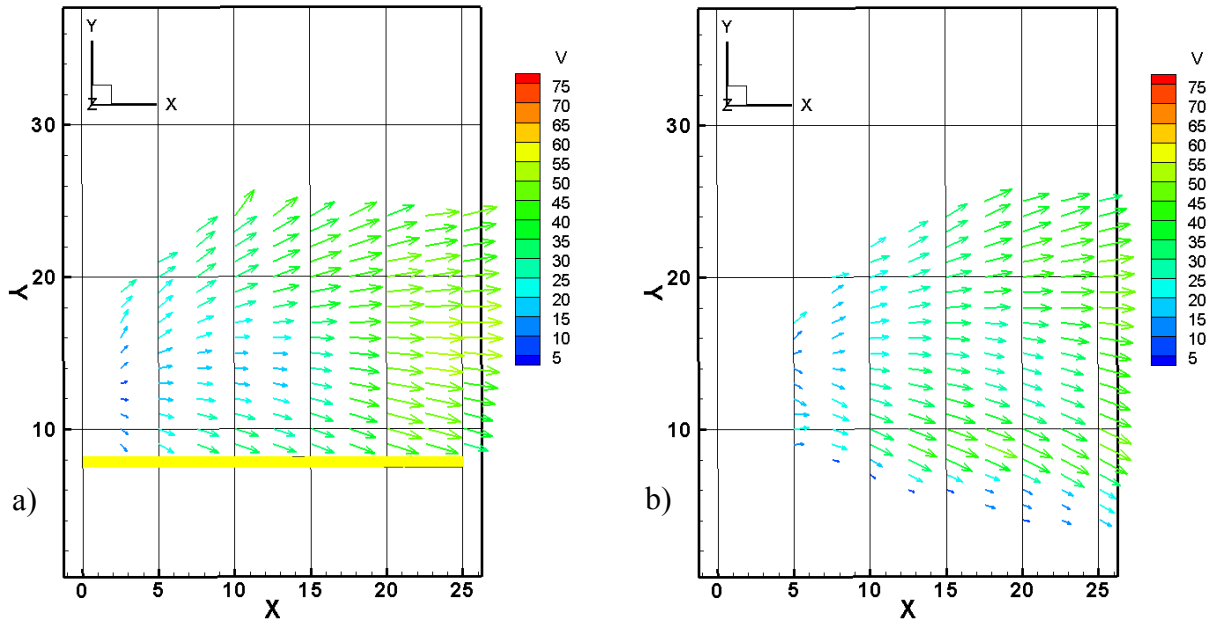

Figure 4.33 Droplet velocity vector distribution for case J3s (45°, *We* = 83.2, *q* = 12.02), a) *z* = -5 mm, b) *z* = -10 mm

The measurement planes were collected together by adding the third coordinate (*z*) to create a 3-D measurement domain. Conversion to cylindrical domain was not attempted since the data was not originally in cross-sectional planes

4.7.1 Streamwise Droplet Velocity Distribution for the Baseline Jet (Case J3s)

Figure 4.33 plots the velocity vector distribution contained within the z = -5, -10 mm planes for the baseline jet, case J3s. Figure 4.33a also shows a slice of the centerbody located at z = -5 mm.

4.8 3-D Droplet Velocities

From the results presented in sections 4.6 and 4.7, all three components of the velocity are now available. Since the test conditions used for measurement in streamwise planes replicated the test conditions used for cross-sectional planes, it is possible to combine the merge the two sets of data. The procedure for combining such datasets and the results is described below.

4.8.1 Obtaining 3-D Droplet Velocity Components

The process of merging the results from cross-sectional and streamwise velocity measurements is to create an entirely new 3-D cartesian grid, and to assign velocity values to the new grid locations by interpolation. Now, for cross-sectional measurements, the largest separation between measurement locations is along X-axis (between two measurement planes) and is equal to 2.5 mm. Similarly, for streamwise plane the largest separation between grid points was along Z-axis, and was equal to 2.5 mm. It follows that when values are assigned to the new grid points, interpolation in any direction will be conducted over a neighborhood of $\pm\lambda/2$, where λ is the interval between two grid points along that direction. Then to ensure that good values are obtained at each grid point, λ must at least as big as the grid spacing in the original grid. Keeping this in mind, the new cartesian grid created with a grid spacing of 2.5 mm between grid points in all direction. This ensures that we can have good interpolation results for the velocity components.

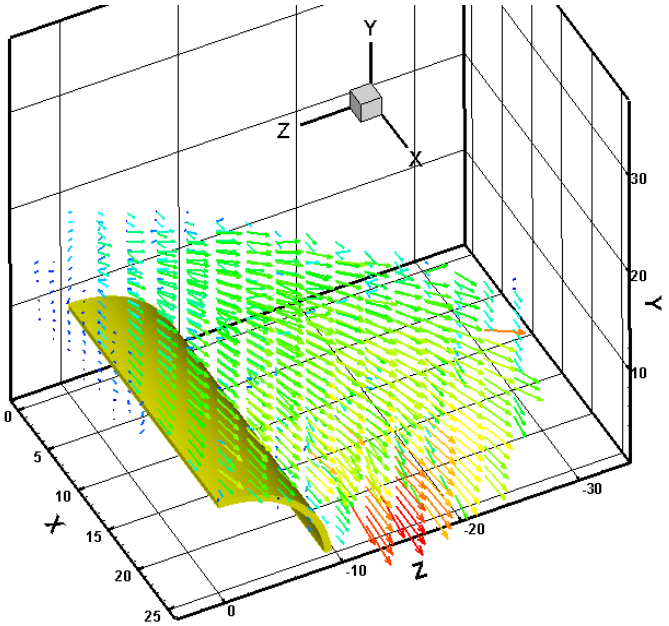

Figure 4.34 3-D velocity vectors for combined case J3 (45°, We = 83.2, q = 12.02)

Now, the streamwise component of velocity, V_x can be obtained from the streamwise velocity measurements while the lateral component of velocity, V_z can be obtained from cross-sectional velocity measurements. The vertical component of velocity, V_y is common to both datasets; hence we need to compare the two sets of V_y before merging. Ideally, the measured values for V_y from the two data sets should match well. However the presence of significant out-of-plane velocity components can likely skew the PIV results for velocity magnitudes. Additionally, there could be small changes in test conditions which could result in slightly different velocity magnitudes. It was observed that the V_y values obtained from the two datasets were close, though the V_y from the streamwise planes was consistently higher. In the end, an average value of V_y from the two datasets was used for the new 3-D grid. The V_y and V_z components of velocity were then used to determine the polar components of velocity, V_r and V_θ, using equations 4.10 and 4.11.

4.8.2 3-D Droplet Velocity Distribution for the Baseline Jet (Case J3)

Figure 4.34 shows the 3-D velocity vectors for the combined case of the baseline jet, case J3. The evolution of each of the three components of velocity is shown separately for better analysis.

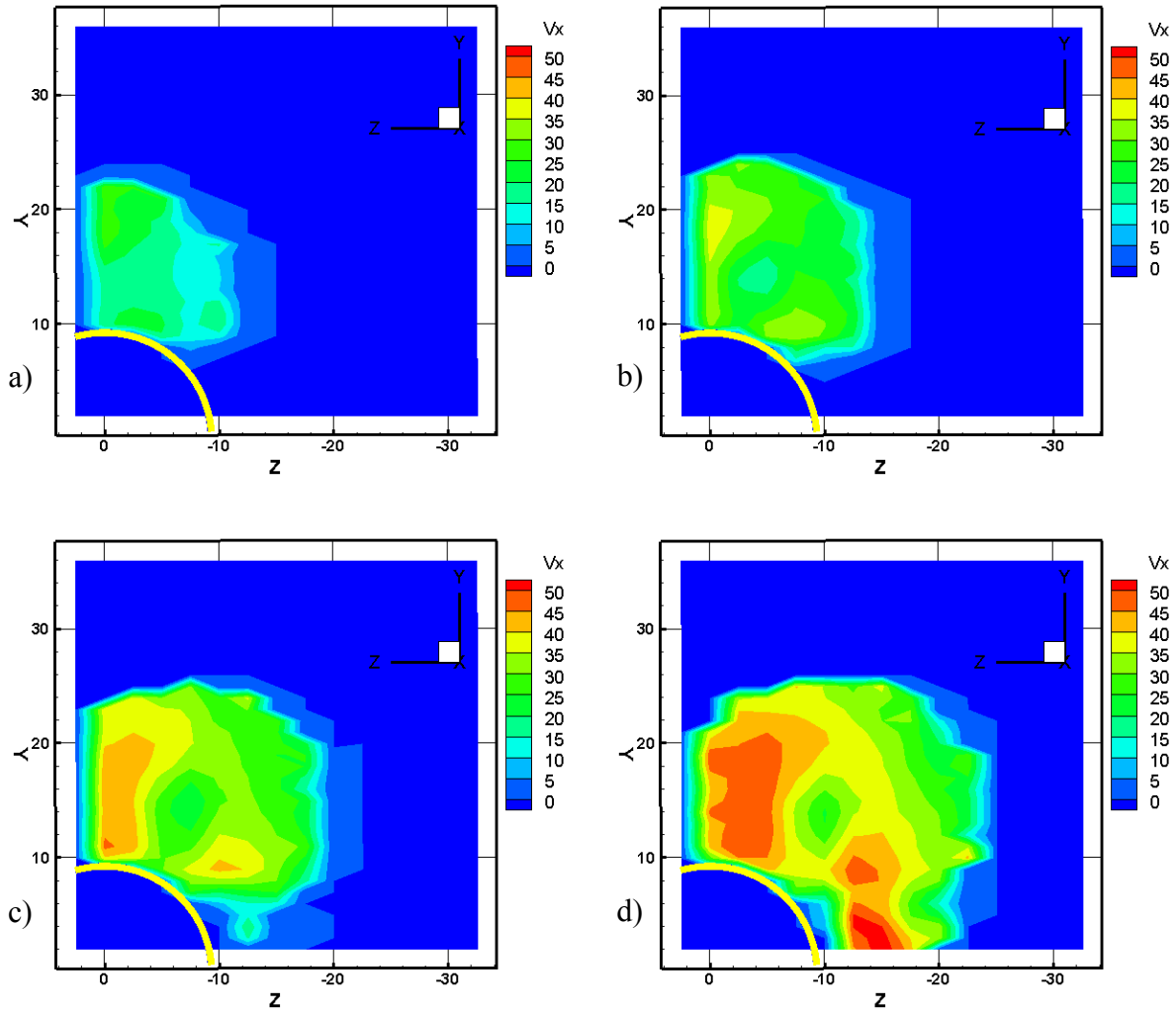

Figure 4.35 Droplet radial velocity, V_x, distribution for combined case J3 (45°, We = 83.2, q = 12.02), a) x = 5 mm, b) x = 10 mm, c) x = 15 mm, d) x = 20 mm

Figure 4.35 plots the contours of streamwise component of the velocity, V_x, for the combined case J3 in cross-sectional planes located at x = 5, 10, 15 and 20 mm respectively. Figure 4.35 shows a low velocity region surrounded by high axial velocities on the sides. This is similar to

the streamwise velocity distribution for liquid jets in uniform crossflow, where the low velocity region represents the spray core of the jet [27, 29]. As the jet proceeds downstream, additional interaction with the crossflow induces and increase in the magnitude of V_x.

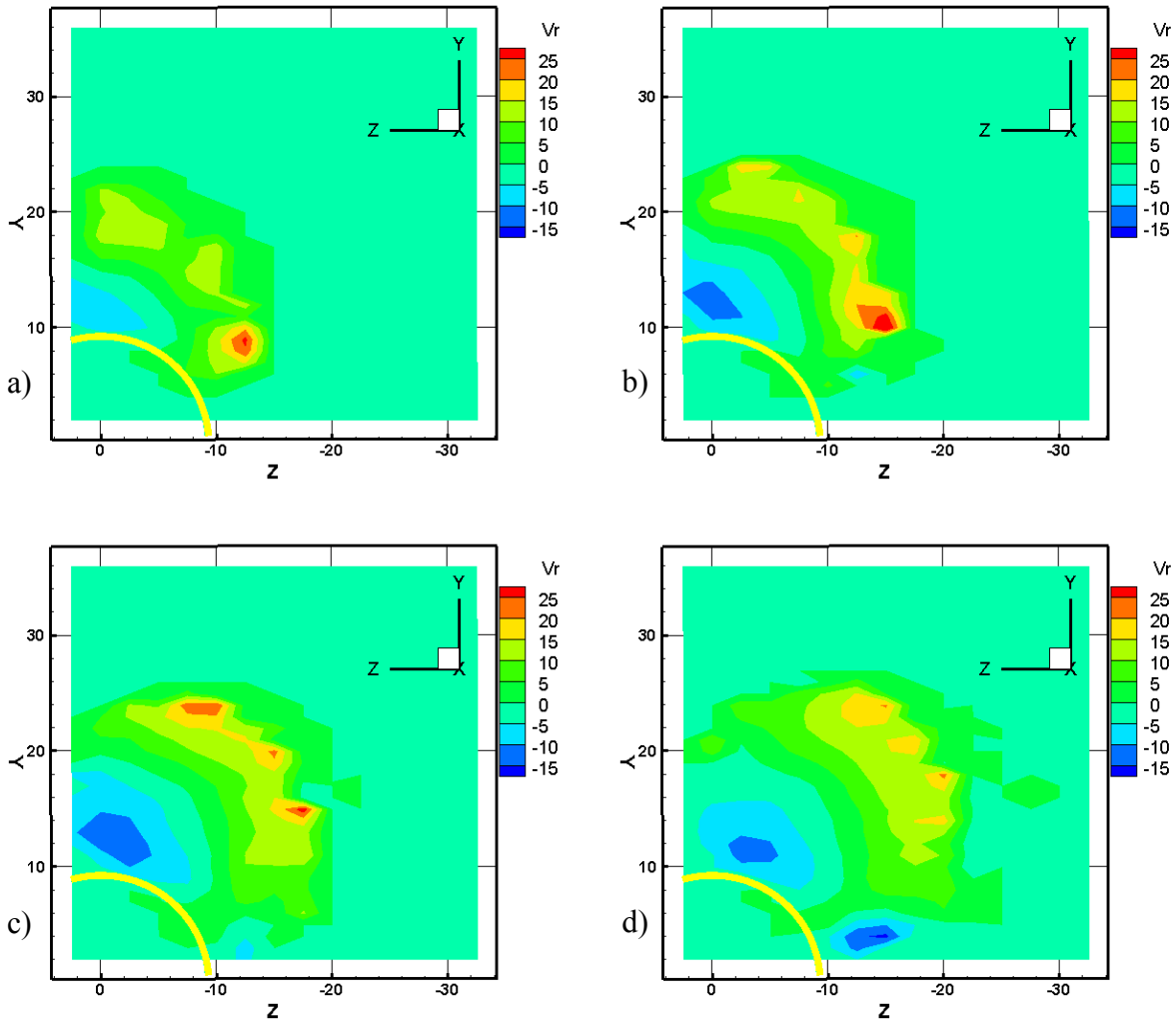

Figure 4.36 Droplet radial velocity, V_r, distribution for combined case J3 (45°, We = 83.2, q = 12.02), a) x = 5 mm, b) x = 10 mm, c) x = 15 mm, d) x = 20 mm

Figure 4.36 shows the contours of radial component of droplet velocity, V_r for the combined case J3 at x = 5, 10, 15 and 20 mm. The radial distribution is essentially similar to that observed for the cross-sectional case (Figure 4.30), with positive V_r at the upper periphery and negative V_r at

the lower periphery of the jet plume. Also here the decrease in the magnitude of V_r with stream-wise distance is more evident, clearly showing that the propensity of the jet for incremental penetration reduces as it progresses downstream.

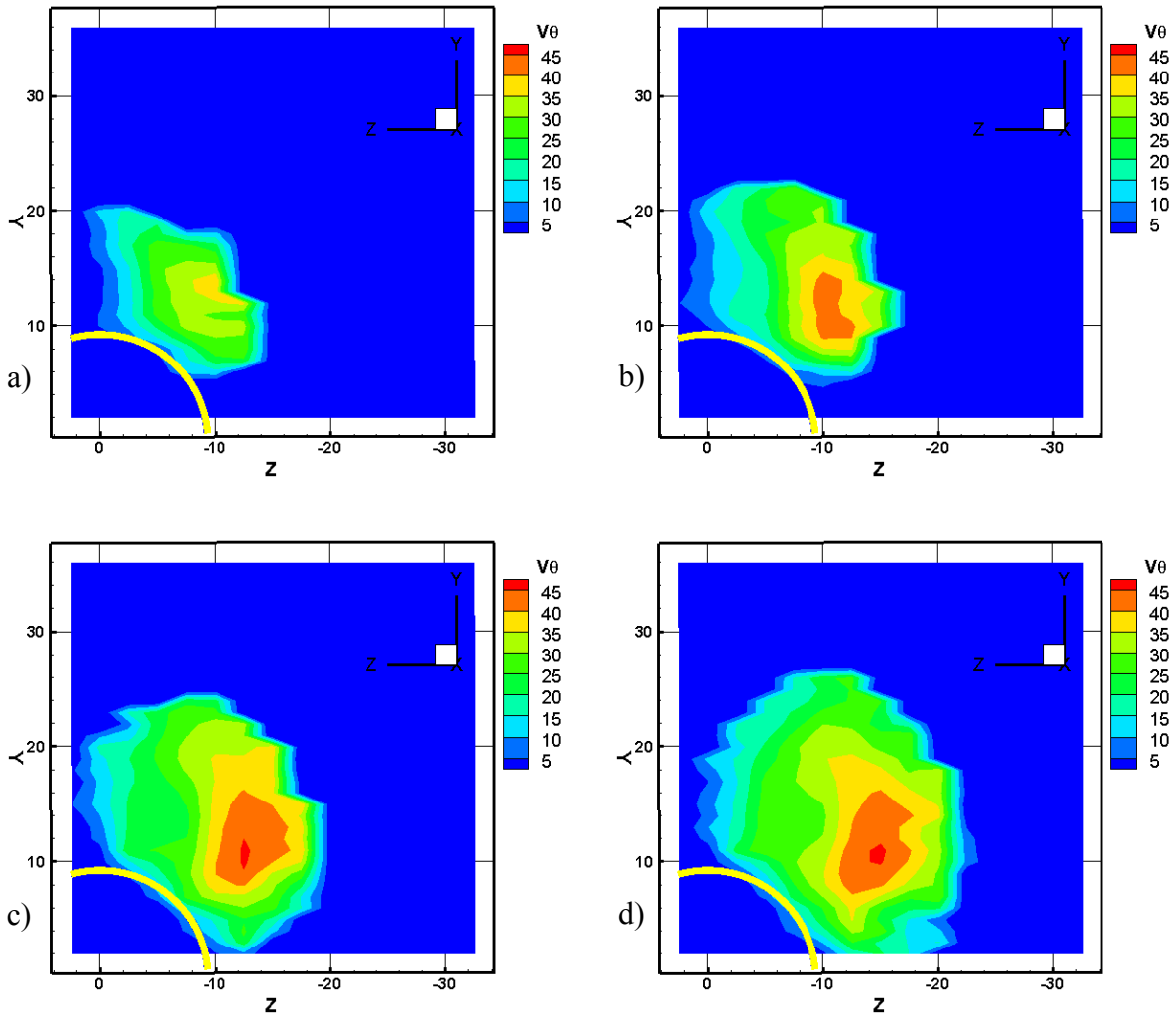

Figure 4.37 Droplet radial velocity, V_θ, distribution for case J3 (45°, We = 83.2, q = 12.02), a) x = 5 mm, b) x = 10 mm, c) x = 15 mm, d) x = 20 mm

Figure 4.37 plots the contours of the tangential velocity, V_θ, for the combined case J3 at x = 5, 10, 15 and 20 mm respectively. The contours of V_θ are also similar to that observed for the cross-

sectional measurements (Figure 4.31) with higher V_θ at the advancing side and lower V_θ at the receding side of the jet.

4.9 Summary of Jets in Swirling Crossflow

Liquid jets injected into a swirling crossflow have been studied. The crossflow was non-recirculating, with both axial and tangential velocities decreasing with radius. Analysis of jet penetration indicated the need to separate the jet penetration into radial and circumferential components to completely describe the jet trajectory. PIV velocity measurements were conducted in cross-sectional as well as streamwise planes, and the velocities were combined to generate a 3-D velocity distribution.

Chapter 5 Conclusions and Future Work

5.1 Conclusions

Recognizing the need to study the impact of crossflows with a non-uniform velocity profile, such as a swirl flow, on the behavior of transversely injected liquid jets, a baseline experimental study has been conducted to evaluate this effect. Two different non-uniform crossflows were devised. The study first characterized the crossflow and then studied water jets injected into these flows. Explanations for deviations in the behavior of the jets compared to jets in uniform crossflows were attempted based on the previously studied non-uniformities in the crossflow.

The shear-laden crossflow was observed to have a quasi-linear velocity profile with a positive velocity gradient for $UR > 1$ and a negative velocity gradient for $UR < 1$. Areas of high turbulence extended from the center of the height of the test chamber to the peak in the crossflow velocity. Cases with $UR = 1$ were also conducted as they were equivalent to studying a uniform crossflow. We observed that the crossflow velocity gradient affects the jet penetration as well as the droplet velocities and sizes. For $UR > 1$, jet penetration increased by up to 100% due to the lower velocities near the nozzle. Droplet velocity distribution was similar to that of a normal jet, while SMD values were distributed more homogeneously. For $UR < 1$, jet penetration was low due to the higher crossflow velocity which also led to improved atomization. Droplet velocities near the upper periphery were very high, and the SMD distribution was close to that of a typical jet, though with lower magnitudes.

The swirling crossflow exhibited velocities whose tangential and streamwise components decreased with radial distance. The flow angles of the crossflow were less than the swirler vane

exit angle, except for the 30° swirler, indicating that the swirlers chosen did not impart the desired tangential momentum to the flow. The flow angle was found to increase with radius. Jets injected into this crossflow were observed to follow a path close to helical shape with a flow angle less than that of the crossflow. The difference in flow angle is expected to be due to jet momentum and the centrifugal force experienced by the jet, and led to the definition of circumferential penetration. Circumferential penetration measures the lag in circumferential displacement of the jet as compared to the crossflow. Radial penetration was found to increase with q while circumferential penetration increased with the swirl angle. The droplet velocity distribution shed more light on the evolution and the spread of the jet plume.

5.2 Future Work

The purpose of this was to create flows similar to the swirling flow expected to be found in a typical combustor, with the shear-laden flow being devised as a 2-D approximation to such a flow. However, the crossflows were designed to be simplified in order to be able to relate crossflow features to jet behavior. And while the shear-laden crossflow did help explain some of the features experienced in the simplified swirling crossflow, in future it might be desirable to create a more realistic crossflow, and test jets injected into it.

For the shear-laden crossflow, adequate measurements were conducted to characterize it. Jet penetration studies were also carried out and a penetration correlation was created to fit the data. Though the correlation fits the data reasonably well, it is desirable to have more data to enhance the robustness of the correlation. Also, due to the long measurement times, PDPA measurements

were restricted to a few selected cases. It is desirable to conduct more studies to study the atomization better.

The swirling crossflow was tested in a square chamber to enable good measurements. However, additional measurements need to be conducted for the crossflow, in order to create a better picture of the velocity distribution. Also, the next step to a better understanding of the jet would be to conduct an atomization study.

References

1. 1 Becker, J., and Hassa, C., "Breakup and Atomization of a Kerosene Jet in Crossflow at Elevated Pressure," Atomization and Sprays, Vol. 11, 2002, pp. 49-67

2. Becker, J., and Hassa, C., "Liquid Fuel Placement and Mixing of Generic Aeroengine Premix Module at Different Operating Conditions," Journal of Engineering for Gas Turbines and Power, Vol. 125, 2003, pp. 901-908

3. Becker, J., Heitz, D., and Hassa, C., "Spray Dispersion in a Counter-Swirling Double-Annular Air Flow at Gas Turbine Conditions," Atomization and Sprays, Vol. 14, 2004, pp. 15-35

4. Beér, J. M., and Chigier, N. A., Combustion Aerodynamics, John Wiley & Sons, 1972, Chapter 5

5. Birouk, M., Azzopardi, B. J., Stäbler, T., "Primary Break-up of a Viscous Liquid Jet in a Cross Airflow," Particle and Particle Systems Characterization, Vol. 20, 2003, pp. 283-289

6. Cavaliere, A., Ragucci, R., and Noviello, C., "Bending and Break-up of a Liquid Jet in a High Pressure Airflow," Experimental Thermal and Fluid Science, Vol. 27, 2003, pp. 449-454

7. Chen, T. H., Smith, C. R. Schommer, D. G., and Nejad, A. S., "Multi-Zone Behavior of Transverse Liquid Jet in High-Speed Flow," AIAA Paper 93-0453, 1993

8. Decent, S. P., King, A. C., and Wallwork, A. C., "Free jets spun from a prilling tower," Journal of Engineering Mathematics, Vo. 42, 2002, pp. 265-282

9. Elshamy, O. M., "Experimental Investigations of Steady and Dynamic Behavior of Transverse Liquid Jets," Ph. D. Dissertation, Dept. of Aerospace Engineering and Engineering Mechanics, University of Cincinnati, Cincinnati OH, 2007

10. Flohre, N., "Experimental Investigation of Spray Atomization Properties of an Aircraft Engine Swirl cup," M. S. Thesis, Dept. of Mechanical Engineering, University of Cincinnati, Cincinnati OH, 2003

11. Fric, T. F., and Roshko, A., "Vortical structure in the wake of a transverse jet," Journal of Fluid Mechanics, Vol. 279, 1994, pp. 1-47

12. Gong, X., Choi, K. J., and Cernansky, N. P., "Lean Direct Wall Injection Mode Atomization of Liquid Jets in Swirling Flow," Journal of Propulsion and Power, Vol. 22, No. 1, 2996, pp. 209-210

13. Han, D., Orozco, V., and Mungal, M. G., "Gross-Entrainment Behavior of Turbulent Jets Injected Obliquely into a Uniform Crossflow," AIAA Journal, Vol. 38, No. 9, 2000, pp. 1643-1649

14. Haven, B. A., and Kurosaka, M., "Kidney and anti-kidney vortices in crossflow jets," Journal of Fluid Mechanics, Vol. 352, 1997, pp. 27-64

15. Inamura, T., "Trajectory of a Liquid Jet Traversing Supersonic Airstreams," Journal of Propulsion, Vol. 16, No. 1, 2000, pp. 155-157

16. Inamura, T., and Nagai, N., "Spray Characteristics of Liquid Jets Traversing Subsonic Airstreams," Journal of Propulsion and Power, Vol. 13, No. 2, March-April 1997, pp. 250-256

17. Inamura, T., Nagai, N., Hirai, T., and Asano, H., "Disintegration Phenomena of Metalized Slurry Fuel Jets in High Speed Air Stream," Proceedings of the 5th International Conference on Liquid Atomization and Spray Systems, Gaithersberg, MD, USA, July 1991, pp. 839-846

18. Kelso, R. M., Lim, T. T., and Perry, A. E., "An experimental study of round jets in crossflow," Journal of Fluid Mechanics, Vol. 306, 1996, pp. 111-144

19. Lefebvre, A. W., Gas Turbine Combustion, 2nd Edition, Taylor & Francis, 1998, Chapter 9

20. Lilley, D. G., "Lateral Jet Injection into Swirling Combustor Flowfields," AIAA/ASME/SAE/ASEE 24th Joint Propulsion Conference, Boston, MA, USA, 1988

21. Lin, K.-C., Kennedy, P. J., and Jackson, T. A., "A Review on Penetration Heights of Transverse Liquid Jets in High-Speed Flows," Proceedings of the 15th International Conference on Liquid Atomization and Spray Systems, Madison, WI, USA, 2002, pp. 345-349

22. Majander, P., and Siikonen, T., "Large-eddy simulation of a round jet in a cross-flow," International Journal of Heat and Fluid Flow, Vol. 27, 2006, pp. 402-415

23. Margason, R. J., "Fifty Years of Jet in Cross Flow Research," AGARD Meeting on Computational and Experimental Assessment of Jets in Cross Flow, 1993

24. http://www.nlreg.com/

25. Oda, T., Hiroyasu, H., Arai, M., and Nishida, K., "Characterization of Liquid Jet Atomization across a High-Speed Airstream," JSME International Journal, Series B, Vol. 37, No. 4, 1994, pp. 937-944

26. Smith, S. H., and Mungal, M. G., "Mixing, structure and scaling of the jet in crossflow," Journal of Fluid Mechanics, Vol. 357, 1998, pp. 83-122

27. Tambe, S. B., "Liquid Jets in Subsonic Crossflow," M. S. Thesis, Dept. of Aerospace Engineering and Engineering Mechanics, University of Cincinnati, Cincinnati OH, 2004

28. Wu, P. -K., Kirkendall, K. A., Fuller, R. P., and Nejad, A. S., "Breakup Processes of Liquid Jets in Subsonic Airflows," Journal of Propulsion and Power, Vol. 13, No. 1, 1997, pp. 64-72

29. Wu, P. -K., Kirkendall, K. A., Fuller, R. P., and Nejad, A. S., "Spray Structures of Liquid Jets Atomized in Subsonic Crossflows," Journal of Propulsion and Power, Vol. 14, No. 2, March-April 1998, pp. 173-181

30. Yuan, L. L., and Street, R. L., "Trajectory and entrainment of a round jet in crossflow," Physics of Fluids, Vol. 10, No. 9, 1998, pp. 2323-2335